UNIVERSITY OF OKLAHOMA

GRADUATE COLLEGE

INVESTIGATING MICROSTRUCTURAL HETEROGENEITY IN ORGANIC SHALE VIA LARGE-SCALE, HIGH RESOLUTION SEM IMAGING

A THESIS

SUBMITTED TO THE GRADUATE FACULTY

in partial fulfillment of the requirements for the

Degree of

MASTER OF SCIENCE

By

HUNG TRAN
Norman, Oklahoma
2017

INVESTIGATING MICROSTRUCTURAL HETEROGENEITY IN ORGANIC SHALE VIA LARGE-SCALE, HIGH RESOLUTION SEM IMAGING

A THESIS APPROVED FOR THE
MEWBOURNE SCHOOL OF PETROLEUM AND GEOLOGICAL ENGINEERING

BY

_____
Dr. Carl Sondergeld, Chair

_____
Dr. Chandra Rai

_____
Dr. Mark Curtis

To my family, friends, and in memory of my late grandparents

Acknowledgements

Firstly, I would like to thank my advisors, Dr. Carl Sondergeld and Dr. Chandra Rai for the opportunities that you have generously provided me with. Working in such a professional environment like the IC^3 lab and Devon Energy Nano Imaging Center is beyond what I could ask for. This thesis would not have been possible without your guidance and support. From the bottom of my heart, you are my best teachers.

I would like to thank Dr. Mark Curtis for your willingness and enthusiasm to deliver your great knowledge of Scanning Electron Microscopy and to help me with my research. Your discipline and professionalism truly inspire me. I also would like to thank Jeremy Jernigen for helping me with the training and experiments. Thank you for sharing me many of your interesting stories.

I would like to express my sincerest thanks to my family overseas for believing in me. Their love and support for the past years truly motivate me to pursue my goals.

I would like to thank all of my friends in the IC^3 lab, undergraduate and graduate students. Thank you for helping me with my research and sharing me great memories.

I would like to acknowledge the OU badminton club and its members as a second family to me. Thank you for providing me with friendly and competitive environment. Every memory with this club will be with me wherever I go. To Mr. Minh Pham, my best friend, thank you for your encouragement and motivation for me to grow as a person. Last but not least, I would like to thank Miho Okuda for giving me the emotional support and helping me get through my toughest time. You are my inspiration to finish this work.

Table of Contents

Acknowledgements iv

List of Tables ..... **Error! Bookmark not defined.**i

List of Figures ix

Abstract xviii

Chapter 1: Introduction 1

1.1 Motivation and Problem Statement 1

1.2 Scope of the Thesis 4

1.3 Organization of the Thesis 5

Chapter 2: Research Background 6

2.1 Scanning Electron Microscopy (SEM) 6

2.1.1 Principle of SEM 6

2.1.2 SEM Signals – Secondary Electrons and Backscattered Electrons 8

2.1.3 SEM Map 10

2.2 Previous Works – SEM Upscaling 11

2.3 Geological Description – Wolfcamp Formation 16

Chapter 3: Experimental Procedure 19

3.1 Sampling Procedure 19

3.2 Scanning Electron Microscopy (SEM) Imaging 20

3.2.1 SEM Procedure 20

3.2.2 SEM Segmentation – Pore and Organic Matter 21

3.2.3 SEM Segmentation – Mineralogy Breakdown 22

3.2.4 SEM Segmentation – Watershed 30
3.3 Petrophysical Measurements 32
3.3.1 Crushed helium Porosity Measurements 32
3.3.2 Total Organic Carbon (TOC) Measurements 33
3.3.3 FTIR Mineralogy Measurements 33
3.3.4 Mercury Injection Capilary Pressure (MICP) Measurements 34
3.3.5 Nuclear Magnetic Resonance (NMR) Measurements 35
3.3.6 Overview – Petrophysical Measurements 36
Chapter 4: Results and Discussion 38
4.1 Pore and Organic Matter 38
4.1.1 Representative Elementary Area 38
4.1.2 Pore and Organic Matter Size Distribution 43
4.1.3 Imaging Data versus Petrophysical Data (Crushed helium Porosity and TOC) 49
4.1.4 Imaging Data versus Mercury Injection Data 53
4.1.5 Imaging Data versus NMR Data 58
4.2 Mineral Grain Size Distribution 61
4.2.1 Representative Elementary Area 61
4.2.2 Grain Size Distribution 67
4.2.3 Clay Grains Alignment 76
Chapter 5: Conclusion 78
5.1 Significance and Contribution 78
5.2 Conclusion 79

5.3 Limitation of the Study 81

5.4 Acknowledgements 82

References 83

List of Tables

Table 2.1 Stratigraphy of selected Permian Basin (UNG, 2012) 17

Table 3.1 Average threshold values from SEM 8-bit images. The classification of the mineral groups can be seen at 3.2.3..... 21

Table 4.1 Average areal percentage and REA values for four mineral groups of the selected seven samples 67

List of Figures

Figure 1.1: Map of the U.S. shale gas and shale oil plays in the lower 48 states (sources: www.eia.gov) 2

Figure 2.1: Components of a typical scanning electron microscope (Hafner, 2007) 7

Figure 2.2: Illustration of multiple types of signals generated from an incident electron beam – sample interaction in the SEM and the regions from which the signals can be detected (Zhou et al., 2007) 9

Figure 2.3: SEM illustration of a secondary electron caused by an inelastic event (left) and a backscattered electron caused by elastic events (Hafner, 2007) 9

Figure 2.4: Portions of the BSE map of the Barnett sample (B4) and the Wolfcamp sample (W4) (left) and their corresponded segmented organic matter (white) network (right) Note a higher concentration of organic matter can be observed in B4 (Curtis et al., 2014) 11

Figure 2.5: SEM image from the map of sample #4. Porosity is segmented (red). Clay porosity leads to a high-degree of pore shape anisotropy (Goergen et al., 2014) 14

Figure 2.6: Workflow for upscaling rock properties in a 3.5 ft carbonate layer from nanometer to gird block scale (Vahrenkamp et al, 2011) 15

Figure 2.7: Absolute permeability for vertical flow from a 3.5 ft layer simulation model (first picture) derived from permeabilities for vertical flow (second picture) and horizontal flows (third and fourth pictures) from 8-inch sample slab (Vahrenkamp et al, 2011) 15

Figure 2.8: Comparison between porosity measured from laboratory and from CT scanning for three plugs located in the 8-inch slab. Strong agreement is observed (Vahrenkamp et al, 2011) 16

Figure 2.9 : Location of Wolfcamp formation (light blue) in the Permian Basin in Texas and New Mexico (USGS) 17

Figure 2.10 : Stratigraphic nomenclature of Delaware Basin and Midland Basin. Note the Wolfcamp formation in Midland Basin is located below the Spaberry formation (Kelly et al., 2012) 18

Figure 2.11 : Vertical depth map of the Wolfcamp formation throughout the Midland Basin (Bachmann et al., 2014) 18

Figure 3.1: Location of SEM Map and petrophysical measurements of the 24 samples from a one foot section of Wolfcamp shale core. Different colored labels indicate different types of tests; the tests are performed next to each other horizontally in each interval. The measurements are compared to the properties estimated from the images spanning the cored interval 19

Figure 3.2: A) pores are segmented, i.e. that is defined through setting gray scale threshold. The left most image is the original, the middle image shows the pore highlighted in red and the right most image show the extracted pore areas, B) organic matter is segmented in an SEM image; organic matter is highlighted in blue. The sequence of images is the same as defined in A 23

Figure 3.3: Sample #1 minerals are segmented through setting gray scale thresholds. There are 4 major mineral groups: group SCL (silica, clays, Mg-dol., feldspar) group CCL (calcite, clays, Fe-dol., K-feldspar), group RA (rutile, apatite), and group P

(pyrite). These groups are highlighted in different colors with density range increasing from the left to the right..... 24

Figure 3.4: A portion of SEM map (sample #1) before and after mineralogy segmentation. There are 4 major mineral groups: group SCL (silica, clays, Mg-dol., feldspar), group CCL (calcite, clays, Fe-dol., K-feldspar), group RA (rutile, apatite), and group P (pyrite). Note the mineral distribution in shale microstructure is much easier to observe with the segmentation..... 25

Figure 3.5: Aspect ratio is defined. Particle with aspect ratio of 1 is perfectly rounded. As the aspect ratio decreases, the particle is more elongated..... 27

Figure 3.6: Grain size distribution of all particles with aspect ratio less than 0.4. Note no clear trend line is observed..... 27

Figure 3.7: Grain size distribution of all particles with aspect ratio less than 0.35. Note no clear trend line is observed..... 28

Figure 3.8: Grain size distribution of all particles with aspect ratio less than 0.3. Note a trend line is observed (black line). More fluctuation is observed due to less number of grains..... 28

Figure 3.9: Clays are separated from other grain particles in aspect ratio histogram due to their elongated shape. The cut-off aspect ratio for separation is 0.3..... 29

Figure 3.10: Four major mineral groups are separated from an SEM map based on gray-scale values. The minerals in each group have close or overlapping gray values. Clays are separated from other grains in group SCl and group CCl based on aspect ratio..... 30

Figure 3.11: Illustration of watershed segmentation process – convert an image of overlapping objects (A) into a distance image (B) and finally into image with completed separated objects by progressively filling "water" 31

Figure 3.12: Watershed segmentation applied to an SEM images. Mixing grains are successfully separated (group CCl (calcite, clays, Fe-dol., K-feldspar) – sample #1)... 32

Figure 3.13: Measured TOC, crushed helium porosity, FTIR mineralogy, NMR T2 distribution, and MICP for the 24 samples plotted against increasing depth over the one foot depth interval. Note that the mineralogy is dominated by clay, predominately illite 37

Figure 4.1: A) Porosity measured from SEM map (sample #5) for different sub-map areas is compared to total porosity for the original map (red line), B) Truncation errors of each porosity is compare to 10% error (red line). Note beyond a map area of roughly 20% of the whole map, the difference in porosity estimates reduces and become acceptable 39

Figure 4.2: A) Organic matter content measured from an SEM map of sample #5 for different sub-map areas is compared to the total organic matter content for the original map (red line), B) Truncation errors of TOC value is compared to 10% error (red line). Note beyond a map area of roughly 70% of the total area, the difference in TOC estimates reduces and become acceptable. Note also this area threshold is considerably larger than that for porosity 41

Figure 4.3: REA for porosity and organic content for 24 samples with depth. These are estimated from the whole maps. In general the REAs for organics are roughly twice that for porosity 42

Figure 4.4: Pore size distribution for 24 samples with 50 nm radius boundary (red line). Note the similarity in the trend for 24 samples.Note the assumption of spherical pores. 45

Figure 4.5: Organic matter size distribution for 24 samples with 50 nm radius boundary (red line). There is more scatter in the organic trends than the porosity trends. Note the assumption of spherical organic matter. 45

Figure 4.6 SEM backscattered images of A) sample #5 and B) sample #13. Red circles highlighted larger organic matter particles which are mostly associated with cracks. These organic filled cracks are important and considered as key to HC generation..... 46

Figure 4.7: Areal contribution of porosity (red) and organic matter (green) for 24 samples assuming a 50nm radius boundary (blue line). Note the assumption of spherical pores and organic matter 47

Figure 4.8: Pore size distribution of A) three sub-maps of 10% scale, average number of pores counted is 627,000 ± 17,000 and B) six sub-maps of 5% scale, average number of pores counted is 228,000 ± 39,000. Note variation at large size 48

Figure 4.9: Comparison of porosity measured from SEM imaging and petrophysical data. Red ellipse highlights the interval with the poorest correlation. The error is 1.0% on average. Note SEM porosity values are measured from the whole maps. 50

Figure 4.10: Comparison of organic content measured from SEM imaging and petrophysical data. Green ellipse highlights the interval with the poorest correlation. The error is 0.6% on average. Note the SEM TOC values are measured from the whole maps..... 51

Figure 4.11: SEM backscattered image of sample #3. SEM porosity and crushed helium porosity measured for this sample are 3.0% and 7.0%, respectively 52

Figure 4.12: SEM backscattered image of sample #3. SEM TOC and LECO™ TOC measured for this sample are 2.4% and 3.8%, respectively 53

Figure 4.13: Mercury intrusion and extrusion as a function of pressure of sample #1. Black arrow indicates the difference between intrusion and extrusion profile, which represent the amount of mercury trapped inside rock sample 54

Figure 4.14: MICP model assumption that all pores (blue) are homogeneous in size (left figure) versus real life scenario where pores with different sizes are mixed together ... 55

Fig 4.15: Comparison of MICP pore volume distribution and SEM imaging pore area distribution of sample #1. While each distribution has one dominant pick, they are not at the same pore radius. 55

Figure 4.16: Comparison of MICP pore volume distribution and SEM imaging pore area distribution for the 24 Wolfcamp samples. Two separated peaks are still observed 57

Figure 4.17: Difference between mercury intrusion and extrusion versus pore body to throat ratio shows a directly proportional relationship 57

Figure 4.18: Glass model with mercury. Lower part shows the residual trapped mercury (Wardlaw and McKellar, 1981) 58

Figure 4.19: Comparison of NMR pore volume distribution (blue) and converted SEM pore area (red) distribution of sample #1. The effective surface relaxation is ρ_e = 33 µm/sec 59

Figure 4.20: Comparison of NMR pore volume distribution (blue) and converted SEM pore area distribution (red) of sample #2. The effective surface relaxation is ρ_e = 40 µm/sec 60

Figure 4.21: Comparison of NMR pore volume distribution (blue) and converted SEM pore area distribution (red) of sample #3. The effective surface relaxation is ρ_e = 46 µm/sec 60

Fig 4.22: Comparison of NMR pore volume distribution (blue) and converted SEM pore area distribution (red) of sample #4. The effective surface relaxation is ρ_e = 46 µm/sec 61

Figure 4.23: A) areal percentage for mineral group SCl (silica, clays, Mg-dolomite, feldspar) measured from SEM map (sample #1) for different sub-map areas is compared to total porosity for the original map (red line), B) Truncation errors of each areal percentage value is compared to 10% error (red line). Note beyond a map area of roughly 11% of the whole map, the difference in areal percentage estimates reduces and become acceptable 62

Figure 4.24: A) areal percentage for mineral group CCl (calcite, Fe-dolomite, clays, K-feldspar) measured from SEM map (sample #1) for different sub-map areas is compared to total porosity for the original map (red line), B) Truncation errors of each areal percentage value is compared to 10% error (red line). Note beyond a map area of roughly 90% of the whole map, the difference in areal percentage estimates reduces and become acceptable 63

Figure 4.25: A) areal percentage for mineral group RA (rutile and apatite) measured from SEM map (sample #1) for different sub-map areas in compared with total porosity

for the original map (red line), B) Truncation errors of each areal percentage value with 10% error (red line). Note beyond a map area of roughly 78% of the whole map, the difference in areal percentage estimates reduces and become acceptable 64

Figure 4.26: A) areal percentage for mineral group P (pyrite) measured from SEM map (sample #1) for different sub-map areas in compared with total porosity for the original map (red line), B) Truncation errors of each areal percentage value with 10% error (red line). Note beyond a map area of roughly 78% of the whole map, the difference in areal percentage estimates reduces and become acceptable..... 65

Figure 4.27: REA values for porosity and four mineral groups for the selected seven samples. Note that REAs for group SCl (silica, clays, Mg-dol., feldspar) are significantly low compared to the others..... 66

Figure 4.28: All Grain size distribution for seven samples with their location on the right picture. Note the similar trend for these seven samples..... 68

Figure 4.29: Grain size distribution for group SCl (silica, clays, Mg-dol., feldspar) of seven samples. Note the similar trend for these samples. A little bit more variation is observed compared to all grain distribution (see Fig.4.28) 69

Figure 4.30: Grain size distribution for group CCl (calcite, clays, Fe-dol., K-feldspar) of seven samples. Note the similar trend for these samples. A little bit more variation is observed compared to all grain distribution 70

Figure 4.31: Grain size distributions for group RA (rutile, apatite) of seven samples. Note the similar trend for these samples. More variation is observed compared to all grain distribution 70

Figure 4.32: Grain size distribution for group P (pyrite) of seven samples. Note the similar trend for these samples. More variation is observed compared to all grain distribution..... 71

Figure 4.33: Grain size distribution for clay grains (left) and other grains (right) from group CCl (calcite, clays, Fe-dol., K-feldspar) in seven samples. Average radius of clay is less than of other grains 72

Figure 4.34: All grain size distribution of three sub-maps of 30% scale for group SCl (silica, clays, Mg-dol., feldspar) of sample #1. Note the similar trend of these sub-maps. Note the assumption of spherical grain 74

Figure 4.35: All grain size distribution of four sub-maps of 20% scale for group SCl (silica, clays, Mg-dol., feldspar) of sample #1. Note the similar trend of these sub-maps. Note the assumption of spherical grain 74

Figure 4.36: All grain size distribution of six sub-maps of 10% scale for group SCl (silica, clays, Mg-dol., feldspar) of sample #1. Note the increase in variation between the plots. Note the assumption of spherical grain..... 75

Figure 4.37: All grain size distribution of six sub-maps of 5% scale for group SCl (silica, clays, Mg-dol., feldspar) of sample #1. Note the increase in variation between the plots. Note the assumption of spherical grain..... 75

Figure 4.38: Clay particle orientation relative to the bedding plane (group CCl (calcite, clays, Fe-dol., K-feldspar) – sample #1). Majority of clays are oriented at 0^0 to 10^0 77

Figure 4.39: Clay particle orientation to the bedding plane at different scale (group CCl (calcite, clays, Fe-dol., K-feldspar) – sample #1). Note the trend gets better as the scale increases 77

Abstract

The physical properties of shale are fundamentally controlled by its microstructure; however, shale is problematic due to microstructural heterogeneity that can exist across multiple scales. This creates difficulty in determining a representative sample size for imaging as well as petrophysical measurements. Utilizing large area, high-resolution SEM imaging, appropriate representative elementary areas (REA) are determined for imaging and analysis. Imaging has been performed on contiguous regions of a 1 ft long section of Wolfcamp Shale core. The porosity and organic matter content of this area has been segmented, analyzed and are reported as bounded values. Pore size distributions and pore areal contributions have been calculated from these data. Measurements on sampling size suggest that the REAs needed for analysis differ for various microstructural components of interest (e.g. the size of the image required for analysis of pores is much smaller than that needed to analyze organic matter). Variations of REAs are reported for porosity and TOC of different samples along the 1 ft Wolfcamp Shale core section. REAs for samples of this core section range from 0.2 - 0.8 mm^2 for analysis of pores and from 0.6 – 1.2 mm^2 for analysis of organic matter.

Grain size of shale controls multiple properties of the formation such as gross gamma ray response, thermal properties, elastic properties, and hydraulic properties. In addition, grain size can provide information about the depositional environment that can be crucial to determine “sweet spots” for hydrocarbon exploration. In this research, an approach to analyze grain size distribution is developed. Initially, minerals can be grouped into four categories based of their grayscale values in 8-bit backscattered

electron tif images. Appropriate representative elementary area (REA) of each mineral group is estimated for imaging and analysis. The aspect ratio of clay minerals can be used to distinguish them from these groups. In addition, watershed segmentation techniques are applied to the images to further the grain size distribution. Orientation study is performed for these clay grains to determine the trend of grain alignment, which is strong indication of shale anisotropy. It is confirmed by the velocity measurements conducted on samples within a 195 ft interval located in the same well.

When comparing with the petrophysical measurements of porosity and organic matter content, the result shows a strong correlation between these petrophysical measurements (crushed helium porosity and TOC) and the SEM measurements (porosity and organic content) even though the unit bases are quite different. I compare SEM pore size distribution with MICP and MNR data. The information obtained from this study has two important implications: 1) it defines the imaging scale required to extract useful information about porosity and organic matter and 2) it provides a method for grain size analysis in shale.

Chapter 1: Introduction

1.1 Motivation and Problem Statement

Organic shales have been traditionally treated as a source rocks for conventional source rocks. In recent years, shales have emerged as oil and gas reservoirs. The exploration and production from shale plays, however, is extremely challenging and expensive due to their low porosity and ultra-low permeability as well as their complicated microstructure. With the development of horizontal drilling and multi-stage hydraulic fracturing technologies, the production has become economic, opening a new era for unconventional resource exploitation.

The distribution of U.S. organic shale formations can be seen in **Fig 1.1**. For these onshore lower 48 states shale plays, the technically recoverable shale gas volume is estimated to be up to 750 Tcf and the technically recoverable shale oil volume is approximately 23.9 billion barrels (EIA, 2011).

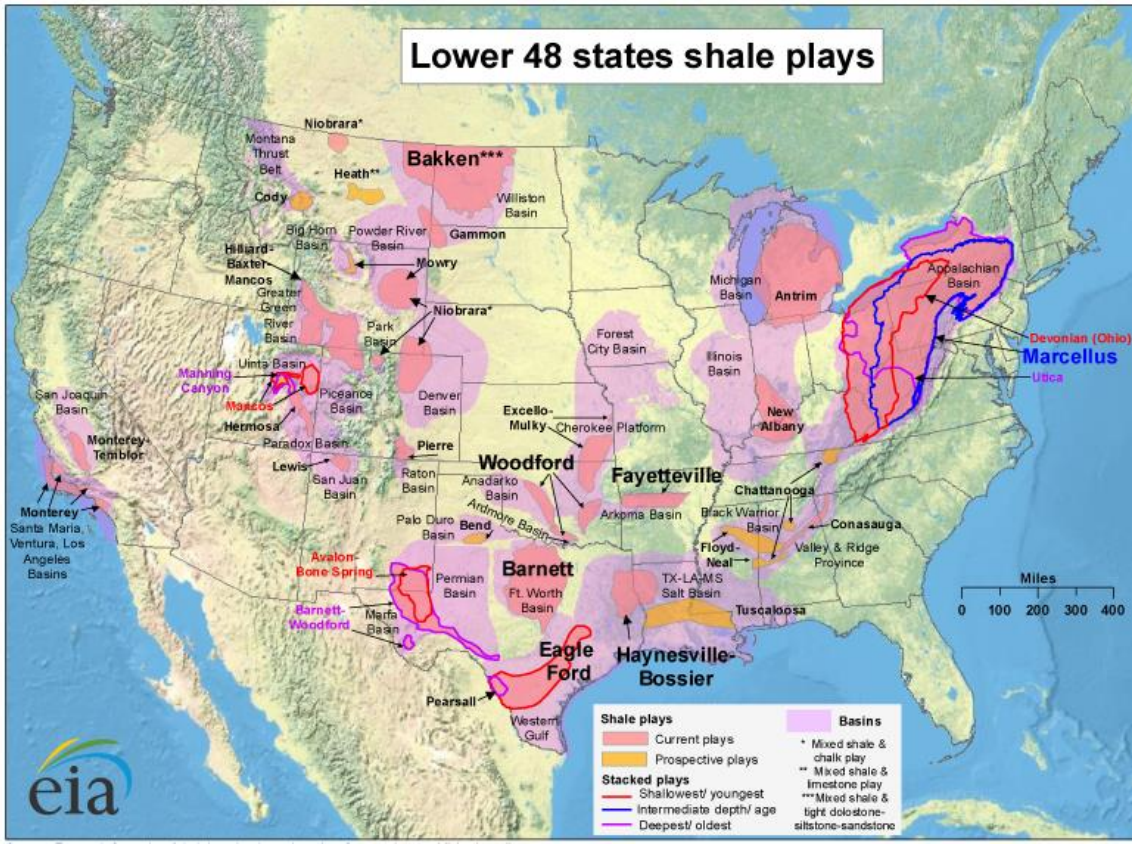

Figure 1.1: Map of the U.S. shale gas and shale oil plays in the lower 48 states (sources: www.eia.gov)

Although each shale has unique composition, organic rich shales by definition have small particle size (below 4 μm in diameter) and contain significant amount of organic matter (2 wt% or above). In addition to their low porosity and ultra-low permeability, shales have a high degree of mineralogical and microstructural heterogeneity at different scales. This creates challenges for both petrophysical measurements and imaging analysis. To deal with heterogeneity, it is crucial to image and analyze shale microstructure across multiple scales. Different techniques including optical and scanning acoustic microscopy (Prasad et al., 2002; Prasad et al., 2009; Bocangel et al., 2013; Ko et al., 2017) were performed to serve this purpose as they allowed mapping

large areas. These techniques however are limited in resolution. Images acquired using scanning electron microscopy (SEM) technique allow extremely small features to be recognized. However, with the favorable resolution, SEM images at high magnification have a very limited field of view. These limitations are overcome by creating a stitched mosaic of high resolution images. In their research, Goergen et al. (2014) created the areas of 1-inch length with high resolution.

Researchers have extracted statistical measurements on pores and organic matter from SEM images, e.g., Loucks, 2009; Curtis et al., 2010; Suri 2011; and Pommer and Milliken, 2015. These studies were performed on relatively small areas, thus suffer significant uncertainty when compared to core-plug petrophysical experiments (Ko et al., 2017). Automated, large-area, high-resolution SEM imaging provides more statistically significant sampling. Unnecessarily large areas, however, result in significant waste of time and money and increase demands for data storage. Determining the optimal scale and resolution required for such measurements would make the overall process of data collection and analysis more efficient.

Multiple techniques have been applied to determine the grain size as well as grain size distribution for rock sample including sieving, laser diffraction, and optical microscopy (Bishop, 1934; Gladkikh et al., 2008; Bakhtiary and Arson, 2013; Ballard and Beare, 2013; Varfolomeev, 2016) Those techniques, however, are more appropriate for conventional reservoir rocks. An approach to estimate grain size for shale using high resolution SEM imaging technique is introduced in this thesis.

This thesis presents results on the determination of bounds on the representative elementary area for imaging and detailed petrophysical analyses of a 1 ft long section of

Wolfcamp Shale core. While conventional techniques require expensive core plugs, SEM imaging can be performed on rock cuttings and less consolidated core plugs.

1.2 Scope of the Thesis

This thesis presents results on the determination of bounds on the representative elementary area (REAs) for pore and organic matter from imaging analyses. The relationship between SEM imaging analyses is correlated with direct petrophysical measurements on core. While conventional techniques require expensive core plugs, SEM imaging can be performed on rock cuttings and less consolidated core plugs. This thesis addresses upscaling SEM data to core petrophysical measurements and potentially to log-scale. Earlier works related to upscaling SEM data to core data are discussed in Curtis et al. (2014) and Goergen et al. (2014).

I used a FEI SEM mapping technique to study large areas (up to 1.6 mm^2) with a resolution of 10 nm. The SEM map experiments as well as petrophysical measurements were conducted on 24 samples taken from a 1 ft section of Wolfcamp core. For each of the samples, a map was broken down into sub-maps. Petrophysical results such as 2D porosity, 2D organic matter, or 2D mineral areal percentage were obtained for each sub-map. These results were combined to determine the REAs. For upscaling purpose, the results extracted from SEM map were compared with results from petrophysical experiments. To be specific, SEM porosity was compared with crushed helium porosity, SEM TOC was compared with LECO™ TOC, and pore size distributions from SEM

was compared with pore size distributions acquired from Mercury Injection Capillary Pressure (MICP) and Nuclear Magnetic Resonance (NMR).

1.3 Organization of the Thesis

The thesis is divided into five chapters and is organized as follows

- Chapter 2 introduces background research undertaken for this thesis. It includes a brief description of scanning electron microscopy, discussion of previous work on the upscaling process, and finally a brief geological description of the Wolfcamp formation.
- Chapter 3 explains the methodology of the FEI SEM mapping technique as well as petrophysical measurements performed on the samples.
- In Chapter 4, the results obtained from SEM maps are presented and discussed.
- Finally, in Chapter 5, conclusions and most significant finding from this study.

Chapter 2: Research Background

2.1 Scanning Electron Microscopy (SEM)

2.1.1 Principle of SEM

The scanning electron microscope is a powerful tool for observing and interpreting the microstructure of rock samples at micro- and nanometer scale. For this study, all of SEM experiments are performed on the FEI Helios Nanolab™ 650 DualBeam™ FIB/SEM machine. The microscope includes following components:

- An electron gun as a source from which an electron beam is accelerated down the column
- A series of lenses including condenser lenses and objective lenses to control the diameter of the electron beam as it interacts the specimen
- A series of apertures to affect the properties of the electron beam when it passes through them
- All of the components above kept at high vacuum levels (Hafner, 2007).

A more detailed breakdown of SEM system is illustrated in **Fig 2.1**. In the SEM, an image of an area is obtained by irradiating that area with a finely focused electron beam, which is swept in a raster across the surface of the specimen (Goldstein et al., 2003) ; the electron beam is rastered from left to right and top to bottom; there is a one-to-one correspondence between the rastering pattern on the specimen/sample and the rastering pattern to produce the image or spectra on a display monitor. The signal created from beam-specimen interaction is collected by the detector and then processed; the intensity of the signal coming from a pixel on the specimen is converted into gray scale value of

the corresponding monitor pixel. The monitor image is thus a two dimensional rastered pattern of grayscale values (Hafner, 2007). Each image is 8-bit; the gray value of 0 represents for black and 255 represents for white.

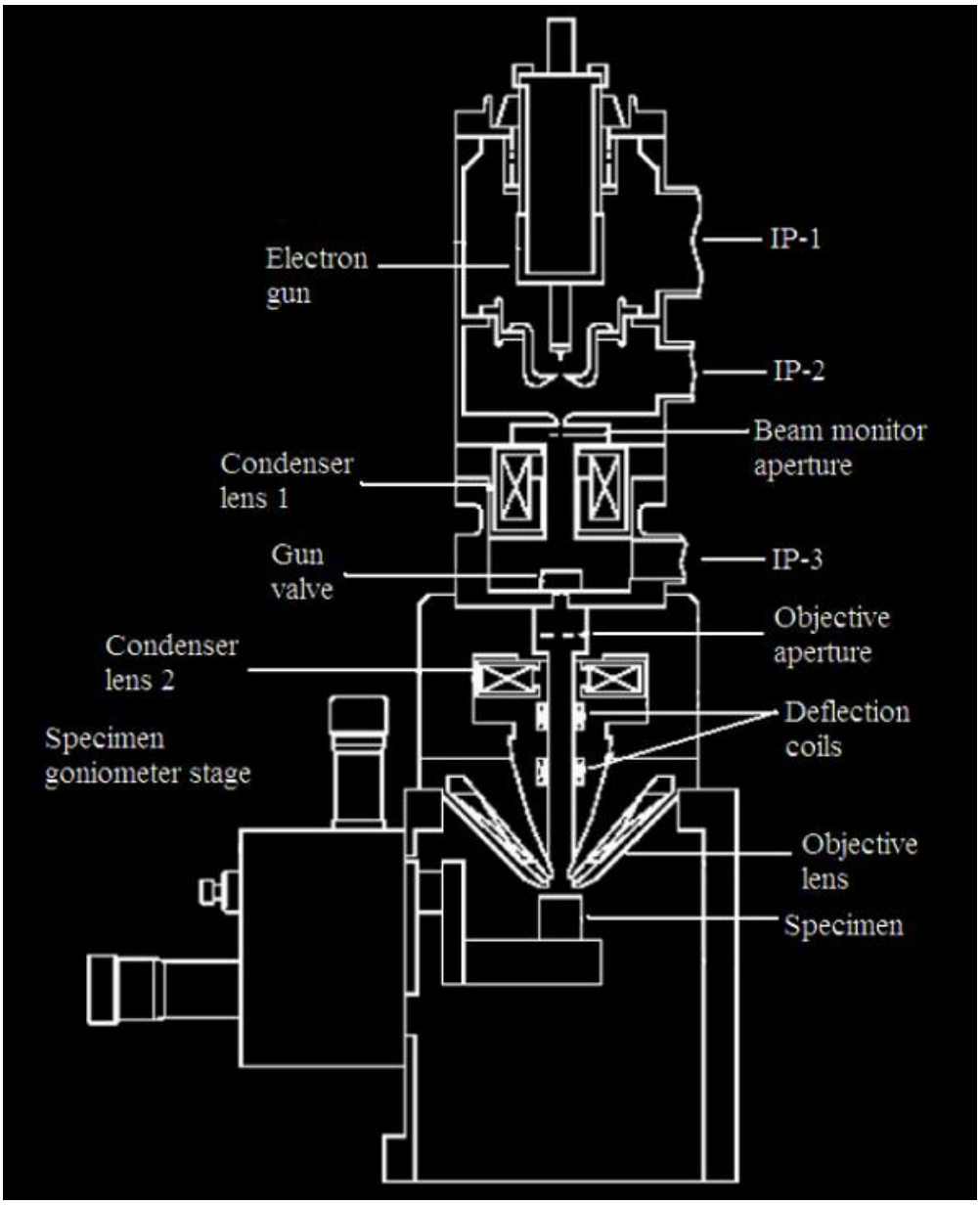

Figure 2.1: Components of a typical scanning electron microscope (Hafner, 2007)

2.1.2 SEM Signals – Secondary Electrons and Backscattered Electrons

During the beam – sample interaction, the beam electron can interact with the electric charge field of both the sample nucleus and electrons. As a result, numerous types of signals are created including backscattered electrons, secondary electrons, characteristic X-Rays, Auger electrons, and cathodoluminescence (Zhou et al., 2007) (**Fig 2.2**). This study focuses upon secondary and backscattered electrons. Secondary electrons are involved in inelastic events where a beam electron interacts with the electric field of a sample atom electron; this results in transfer energy to the sample atom and a potential expulsion of an electron from that atom as a secondary electron (SE). SE's energy is less than 50 eV (Hafner, 2007). SEs are mostly used for topographic contrast in the SEM, i.e. for the visualization of surface texture and roughness. The topographical image quality depends on the number of SEs collected by the detector (Zhou et al., 2007).

Backscattered electrons are involved in elastic events where a beam electron interacts with the electric field of the nucleus of a specimen atom; this results in a change in direction of the beam electron without any significant change in the energy of the beam electron. If the beam electron is deflected back out of the sample, the diverted electron is called backscatter electron (BSE). BSEs can have energy from 50 eV to almost equal to incident beam electron energy (Hafner, 2007). **Fig 2.3** visualizes the two types of electrons by two types of beam-sample interaction. The BSE signal is sensitive to the atomic number (Z) contrast. Areas of sample composed of higher atomic number will have more positive charges on the nucleus resulting in more electrons being

backscattered, which yields more backscatter signal and thus appear brighter in the image. For pore, organic matter, and mineralogy interpretation, the SEM images from SEM MAPS™ are generated with backscattered mode.

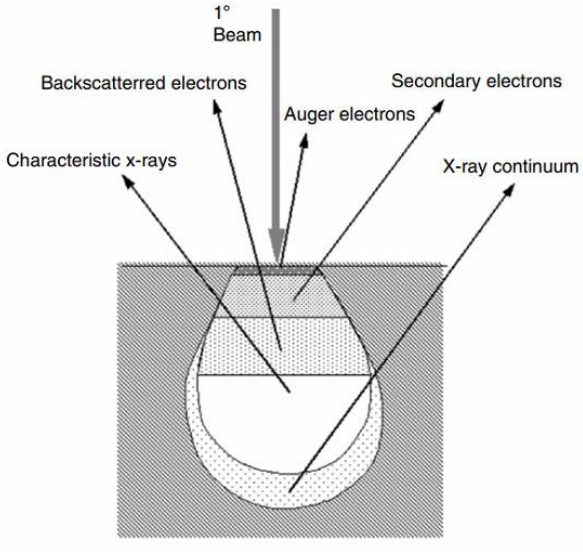

Figure 2.2: Illustration of multiple types of signals generated from an incident electron beam – sample interaction in the SEM and the regions from which the signals can be detected (Zhou et al., 2007)

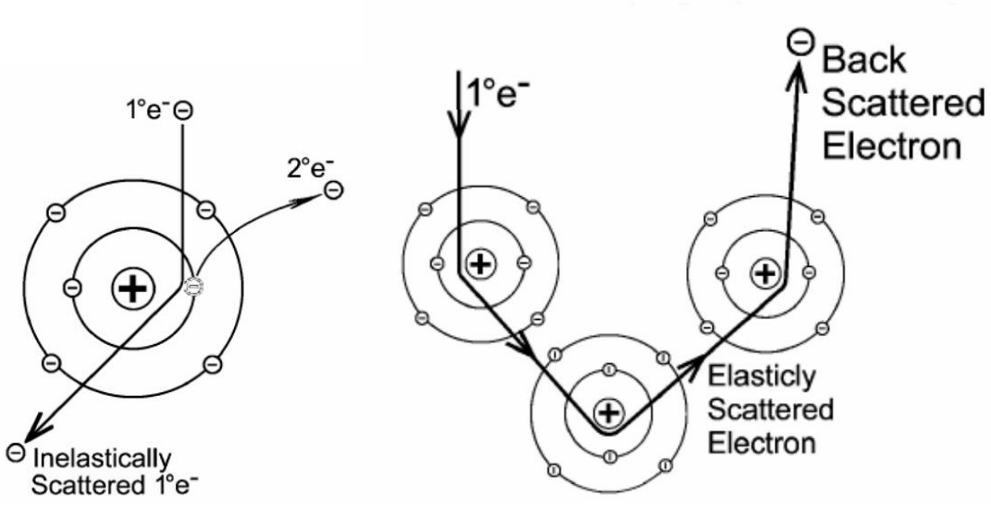

Figure 2.3: SEM illustration of a secondary electron caused by an inelastic event (left) and a backscattered electron caused by elastic events (Hafner, 2007)

2.1.3 SEM Map

All the maps were generated using FEI SEM MAPS™ software which facilitates automated acquisition of high-resolution SEM images. Initially, the dimensions and location of a map on the imaging surface of a sample is selected. By choosing the resolution, the dimension and the number of SEM images is thus determined. The quality of the SEM images is extremely sensitive to the depth of focus. A slight change in working distance, i.e. the distance of between the objectives lens and the sample, during the automated imaging process can result in out of focus image. Therefore, there is a requirement for calibrating focus. The focus setting is chosen as “interpolated”. By using interpolated focus setting, three locations in the map are manually picked for calibration; the locations near the edge of the map are favorable as they can cover the maximum area of the map. At each location, the SEM images are finely focused up to x100,000 magnification. All SEM images are then automatically acquired based on the working distance of the three calibrated locations. Finally, the images are stitched together to form a complete map. The overlap between two images is no larger than 5% of the dimension of each image.

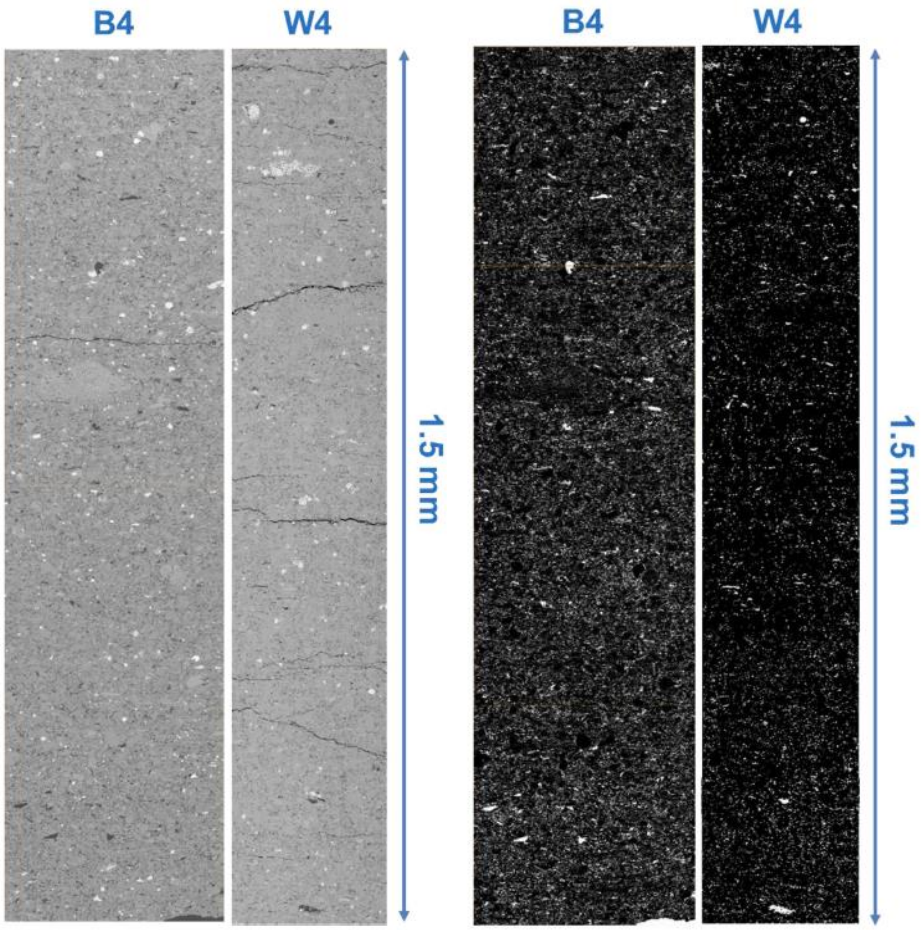

Figure 2.4: Portions of the BSE map of the Barnett sample (B4) and the Wolfcamp sample (W4) (left) and their corresponded segmented organic matter (white) network (right) Note a higher concentration of organic matter can be observed in B4 (Curtis et al., 2014)

2.2 Previous Works – SEM Upscaling

It is crucial to analyze and interpret shale microstructure as shale microstructure is the fundamental factor that controls its physical properties. While many different techniques mentioned in Chapter 1 applied for microstructural study fall short of either

providing sufficient area of investigation or providing sufficient resolution. The idea of using automated high-resolution SEM imaging and stitching technique to overcome this challenge had been applied by Curtis et al. (2014) and Goergen et al. (2014). The results from imaging data are correlated with discrete core petrophysical measurements for upscaling purpose.

Curtis et al. (2014) presented an attempt to map the distribution and connectivity of organic matter in shale. **Fig 2.4** shows portion of the BSE maps of one Barnett sample (B4) and one Wolfcamp sample (W4) and their corresponding segmented organic matter network BSE maps. The length of the images is 1.5 mm. The measured TOC values for B4 and W4 are 7.6 wt% and 3.4 wt%, respectively, while the organic contents from the area measured from the maps for these two samples are 14.6% and 4.5%, respectively. The weight percentage of organic matter translates into more organic matter by area for all samples. However, while the difference between TOC and SEM organic matter content is fairly small for the Wolfcamp sample, the difference is large (7% difference) for the Barnett sample. It can be seen from **Fig 2.4** that most of organic matter associated with the clay is small and elongated while majority of organic matter associated with larger, non-clay grain is larger. W4 is heavily dominated by clay (78%), more of small, elongated organic matter is observed, resulting in less organic content. Compared to W4, B4 is less clay dominated (48%) but contains much more quartz and carbonate, resulting in larger organic sizes. Statistical results extracted from 1/8 of area of the map (due to size limitation) on sample W4 suggests that most of organic matter is below 100 nm in diameter and is elongated. Note that most of organic matter being elongated may be a consequence of looking parallel to bedding plane and

viewing the edge of the organics. The orientation study for both two samples suggests no strong preference to the bedding plane is found for all organic matter. However, when the study is restricted to the largest 100 organic matter objects, they appear to orient at roughly 19^{o} to bedding for both two samples.

Before this thesis, study on capturing scale of heterogeneity in organic shale was presented (Goergen et al., 2014). The study was conducted using the FEI SEM mapping technique. The experiments were conducted on a 1 ft section of Wolfcamp core, the same with the samples using in this thesis. The maps acquired for the samples is up to 2 mm in length. Goergen's statistical results from the map of sample #4 indicate that although there is organic porosity, clay porosity dominates and makes up to 80% of the total segmented porosity. **Fig 2.5** illustrates the dominance of clay porosity. The image is from the map of the same sample; porosity is segmented and highlighted in red. Clay porosity develops a near bedding (horizontal orientation) dominant pore network. When comparing with crushed helium porosity, SEM porosity for the map of this sample appears to be less, 4.0% compared to 7.8% (Goergen et al., 2014).

Upscaling of rock properties was also studied for conventional reservoir. Previously, rock properties measured from core plugs in the laboratory with inadequate evaluation of heterogeneity. These properties were used as an input for simulation grid blocks which have larger volume, resulting in remarkable uncertainties and imprecision. Vahrenkamp et al, 2011 introduced a new approach to account for carbonate inherent heterogeneity via small scale simulation model. The study was conducted on a 3.5 ft thick carbonate layer in the vertical direction. Different rock properties such as porosity,

permeability, and relative permeability curves were determined using high resolution CT scanning – Digital Rock Physics (DRP) processes combination on a 8-inch slab of core. These properties were served as an input for the simulation model of the 3.5 ft carbonate layer; the simulation model is created from deriving Formation Macro Imager (FMI) logging data and it provides the upscaled absolute permeability and relative permeabilities. The detailed workflow is showed in **Fig 2.6. Fig 2.7** shows the permeabilities estimated from CT-DRP combination on the 8-inch sample slab: the permeability for vertical flow is 6.0 mD and the permeabilities for horizontal flows are 2.3 mD and 3.3 mD. These permeabilities result in an absolute permeability of 8 mD for vertical flow for the grid block model derived from FMI logging (**Fig 2.7**). **Fig 2.8** shows the comparison between porosity values of three plugs from this 8-inch slab estimated from CT-DRP combination and those from laboratory measurements. A strong agreement is observed for porosity estimation from all of the plugs.

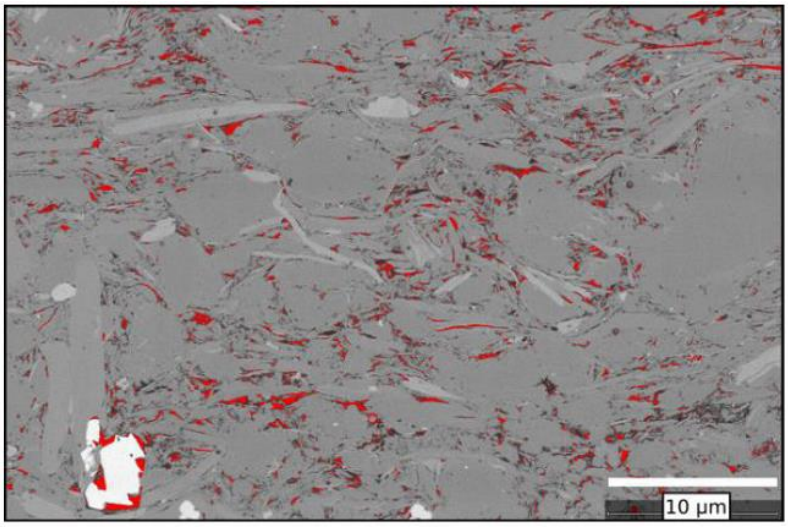

Figure 2.5: SEM image from the map of sample #4. Porosity is segmented (red). Clay porosity leads to a high-degree of pore shape anisotropy (Goergen et al., 2014)

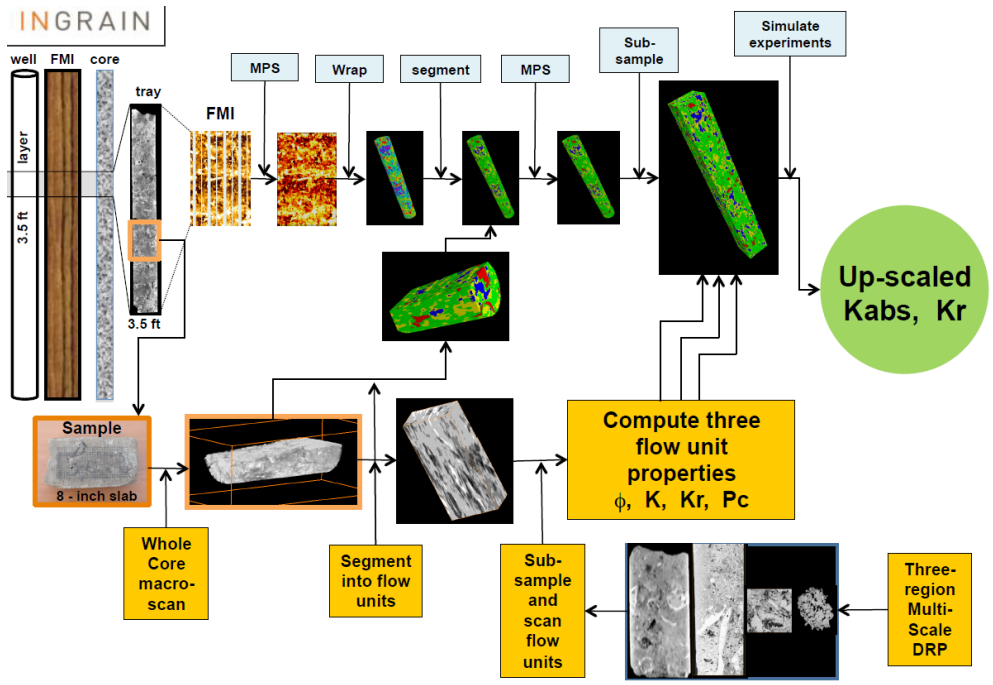

Figure 2.6: Workflow for upscaling rock properties in a 3.5 ft carbonate layer from nanometer to gird block scale (Vahrenkamp et al, 2011).

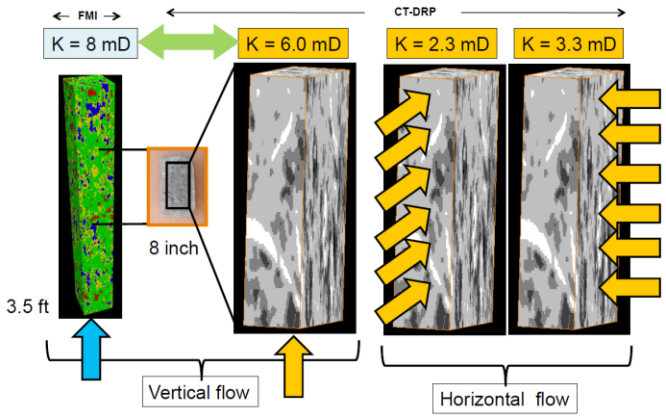

Figure 2.7: Absolute permeability for vertical flow from a 3.5 ft layer simulation model (first picture) derived from permeabilities for vertical flow (second picture) and horizontal flows (third and fourth pictures) from 8-inch sample slab (Vahrenkamp et al, 2011).

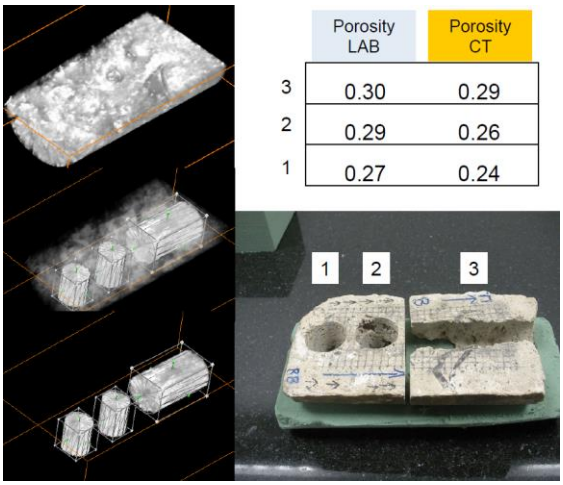

Figure 2.8: Comparison between porosity measured from laboratory and from CT scanning for three plugs located in the 8-inch slab. Strong agreement is observed (Vahrenkamp et al, 2011).

2.3 Geologic Description – Wolfcamp Formation

The Wolfcamp shale is located at the Permian Basin of Texas and New Mexico (**Fig 2.9)**. The samples selected for this microstructural study were from the Wolfcamp Shale located in southern Midland Basin below the Spraberry Formation (**Fig 2.10**). United States Geological Survey (USGS) has confirmed that the Midland Basin Wolfcamp contain approximately 20 billion barrels of recoverable oil, 16 trillion cubic feet of associated natural gas, and 1.6 billion barrels of natural gas liquids (USGS, 2016). The total organic carbon for the Midland Basin Wolfcamp Shale range from 2 to 10 wt%; Ro values ranges from 0.85 to 1.10% which indicates the formation is at the late oil generation and early gas generation windows (UNG, 2012). The formation is deepest at the center of the Basin (approximately 12,000 ft) and becomes much shallower varying

from 4,000 to 7,000 ft when moving towards the edges of the basin (**Fig 2.11**). The formation is composed of a series of laminated black shales and argillaceous limestone.

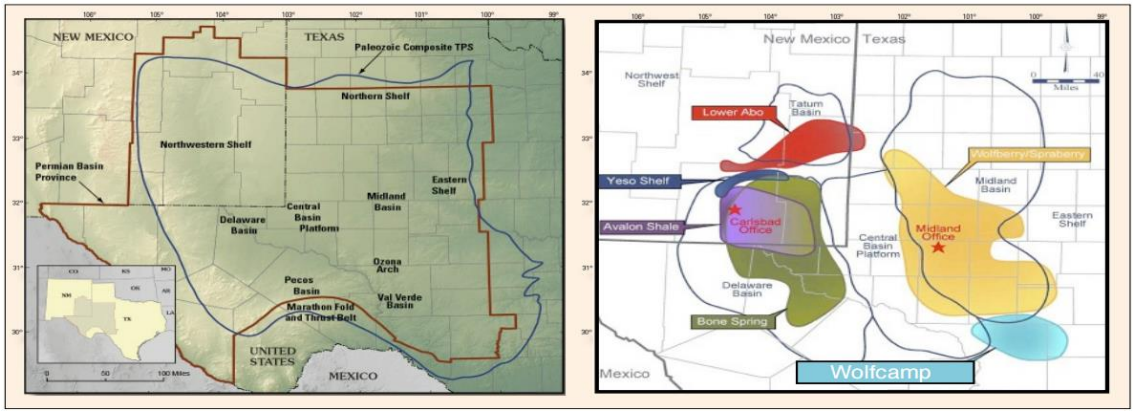

Figure 2.9: Location of Wolfcamp formation (light blue) in the Permian Basin in Texas and New Mexico (USGS)

Table 2.1: Stratigraphy of selected Permian Basin (UNG, 2012)

System	Northwest Shelf			Delaware Basin		Midland Basin		
Permian		Dewey Lake			Dewey Lake		Dewey Lake	
		Rustler			Rustler		Rustler	
		Salado			Salado		Salado	
					Castile			
	Whiten Horse	Tansill	Goat Seep - Capitan Reef	Delaware Mountain Group	Lamar	Whitenhorse	Tansill	
		Yates			Bell Canyon		Yates	
		7 Rivers					Seven Rivers	
		Queen			Cherry Canyon		Queen	
		Grayburg					Grayburg	
	Word	San Andres			Brushy Canyon	Word	San Andres	
		Glorieta					San Angelo	
	Yeso	Paddock		Bone Spring	Avalon Shale		Clearfork	Wolfberry / Wolffork
		Blineberry			1st Bone Spring Sand			
		Tubb					Upper Spraberry	
		L. Clearfork			2nd Bone Spring Sand		Lower Spraberry	
		Abo					Dean	
					3rd Bone Spring Sand			
		Wolfcamp			Wolfcamp		Wolfcamp	
Pennsylvanian		Cisco			Cisco		Cisco	
		Canyon			Canyon		Canyon	
		Strawn			Strawn		Strawn	
		Atoka			Atoka		Atoka	
		Morrow			Morrow			

Figure 2.10: Stratigraphic nomenclature of Delaware Basin and Midland Basin. Note the Wolfcamp formation in Midland Basin is located below the Spaberry formation (Kelly et al., 2012).

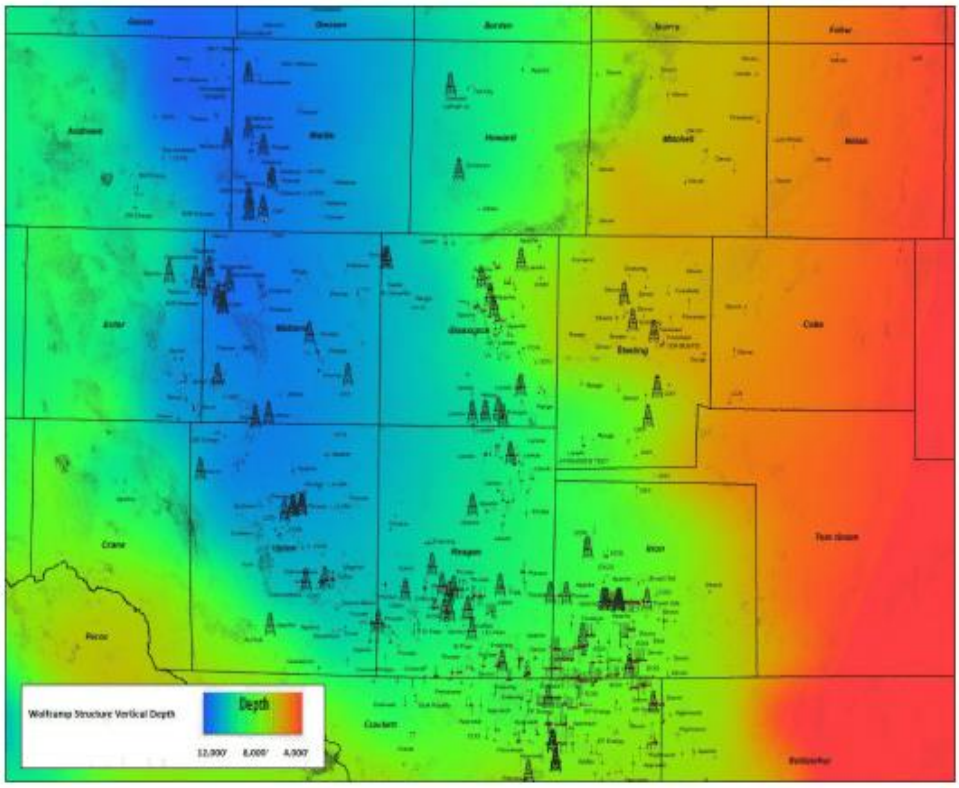

Figure 2.11: Vertical depth map of the Wolfcamp formation throughout the Midland Basin (Bachmann et al., 2014)

Chapter 3: Experimental Procedure

3.1 Sampling Procedure

A 1-foot section of core was selected from the Midland Basin Wolfcamp Shale and sampled. **Fig 3.1** illustrates the sampling and tests performed. A vertical slab was taken from the core and divided into 24 intervals (approximately 12.5 mm each). Samples were taken from each interval for SEM, FTIR, SRA, crushed helium porosity, and TOC measurement. As indicated, the samples were taken such that the material for each test was taken as close as possible, horizontally, to other test samples for that interval.

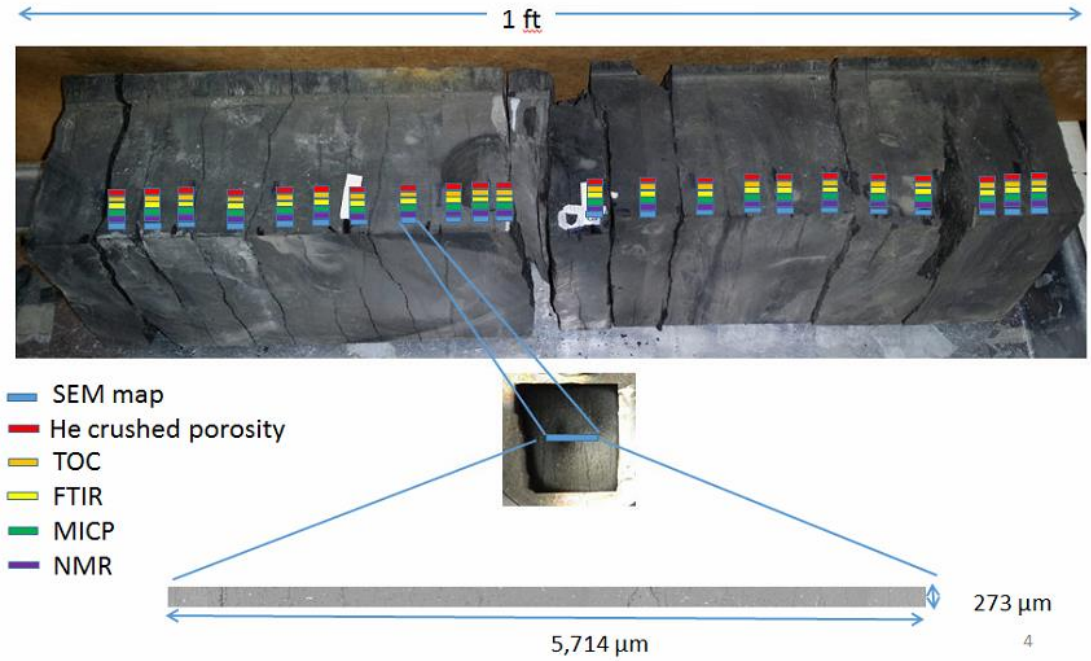

Figure 3.1: Location of SEM Map and petrophysical measurements of the 24 samples from a one-foot section of Wolfcamp shale core. Different colored labels indicate different types of tests; the tests are performed next to each other horizontally in each interval. The measurements are compared to the properties estimated from the images spanning the cored interval

3.2 Scanning Electron Microscopy (SEM) Imaging

3.2.1 SEM Procedure

The SEM samples were prepared perpendicular to bedding by mechanical polishing. 400, 600, and 800 grit emery paper were used until there were no remarkable scratches or artifacts observed on the surface under monocular microscope at 50x magnification. The samples then underwent broad ion beam milling the sample process. Two-step milling procedure using a Fischione Instruments Model 1060 ion mill is performed allow large milled surface area for imaging. The first step is three-hour milling at 5 kV voltage which focused on the center area of the sample. The second step is nine-hour milling at 6 kV voltage at low angle which focuses on the surrounding region. Milled samples were lightly sputter coated with Au/Pd to minimize charging artifacts. Imaging was performed by FEI MAPS software on a FEI Helios Nanolab™ 650 DualBeam™ FIB/SEM using a concentric backscatter detector (CBS) and a 2 kV accelerating voltage. The reason for using backscattered electron images is that this type of imaging is sensitive to atomic number and Z-contrast. Features on the SEM image which are composed of heavier elements, i.e. have higher Z, appear lighter. On a typical SEM image for shale microstructure, pore is the darkest feature, while pyrite is the lightest feature. An entire SEM map for each sample was centered on the sample and the size of the maps were approximately 270 μm wide by 6,000 μm long (1.56 mm^2 area). Each map is comprised of about 3,000 individual SEM images; the length of the image is perpendicular to bedding. To preserve the highest quality for the map, consistency of contrast and focus of the images are required. Instead of running one map at the desired size (273 μm x 6,000 μm), three sub-maps with dimensions of 273 μm x 2,000 μm

(each includes ~1,000 SEM images) were acquired. The three maps were stitched into a large map with desired dimension. The resolution of each map was 10 nm.

Avizo® Fire 9.0 and custom MATLAB software were utilized for analysis on the SEM MAPS™. Every map underwent a denoising procedure using non-local means filter method by Avizo® Fire 9.0 software. After that, components of interest were carefully segmented by choosing threshold values from SEM images and their statistical results were extracted. The average threshold values are reported in **Table 3.1.**

Table 3.1 – Average threshold values from SEM 8-bit images. The classification of the mineral groups can be seen at 3.2.3

Component	Threshold range
Pore	0 - 114
Organic matter	115-135
Mineral group SCl (silica, clays, Mg-dol., feldspar)	136-156
Mineral group CCl (calcite, clays, Fe-dol., K-feldspar)	157-178
Mineral group RA (rutile, apatite)	179-200
Mineral group P (pyrite)	201-255

3.2.1 SEM Segmentation – Pore and Organic Matter

Pore and organic matter are the lowest density components in shale microstructure, hence pores are the darkest and organic matter is the second darkest feature presented on the SEM map. **Fig 3.2** illustrates an example of how pore and organic matter are segmented from an SEM image. The threshold values are determined manually for each component and the gray scale image is converted into binary image.

3.2.3 SEM Segmentation – Mineralogy Breakdown

Besides porosity and organic matter, minerals with different densities presents as different shades of a gray in an SEM images. Due to their much higher density, minerals appear as much brighter features compared to pores and organic matter. Based on gray scale, four major groups of minerals are recognized and separated: group SCl including silica, clays (kaolinite and illite), magnesium rich dolomite, and feldspar; group CCl including calcite, clays (chlorite), iron rich dolomite, and potassium feldspar; group RA including rutile and apatite; and group P including pyrite. Because the gray values of certain minerals in each group are very similar or overlapping (especially in group SCl and group CCl), they can not be separated from each other based on gray scales. **Fig 3.3** shows an example of how the four major groups of minerals are segmented from an SEM image from sample #1. Note the mineral grains in group SCl constitute to most of the microstructure. The majority of the minerals in this group are large quartz grains mixing with numerous clays. Majority of the minerals in group CCl are highly elongated clays and large to average sized calcite and dolomite grains. Compared to group SCl, clays in group CCl are more abundant. Only a few mineral

grains are observed in group RA and P. Rutile and apatite grains (group RA) tend to have smaller size than pyrite grains (group P). **Fig 3.4** illustrates how the mineral distribution observation is significantly enhanced by converting gray scale SEM map into color map with different colors represent different major mineral groups as well as pore and organic matter.

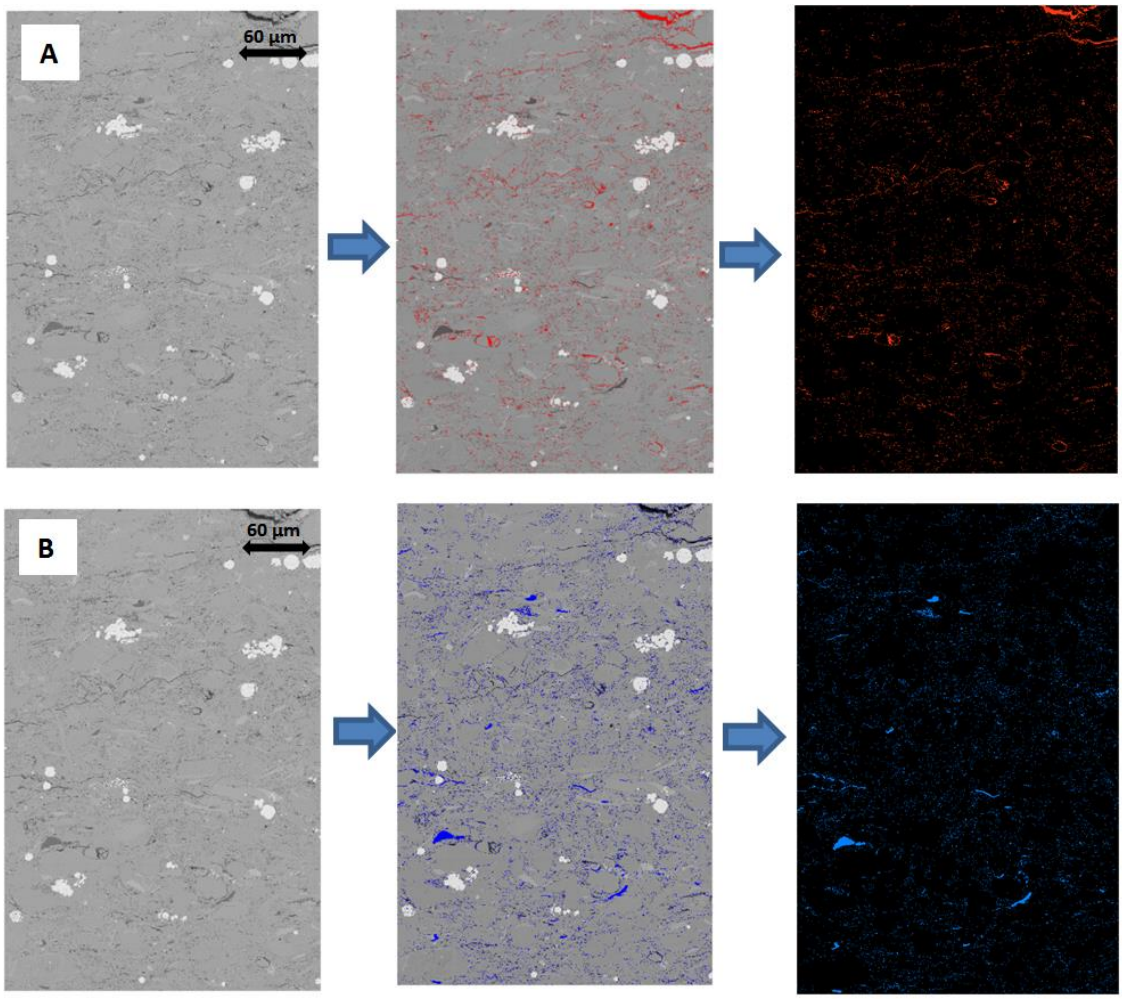

Figure 3.2: A) pores are segmented, i.e. that is defined through setting gray scale thresholds. The left most image is the original, the middle image shows the pore highlighted in red and the right most image show the extracted pore areas, B)

organic matter is segmented in an SEM image; organic matter is highlighted in blue. The sequence of images is the same as defined in A.

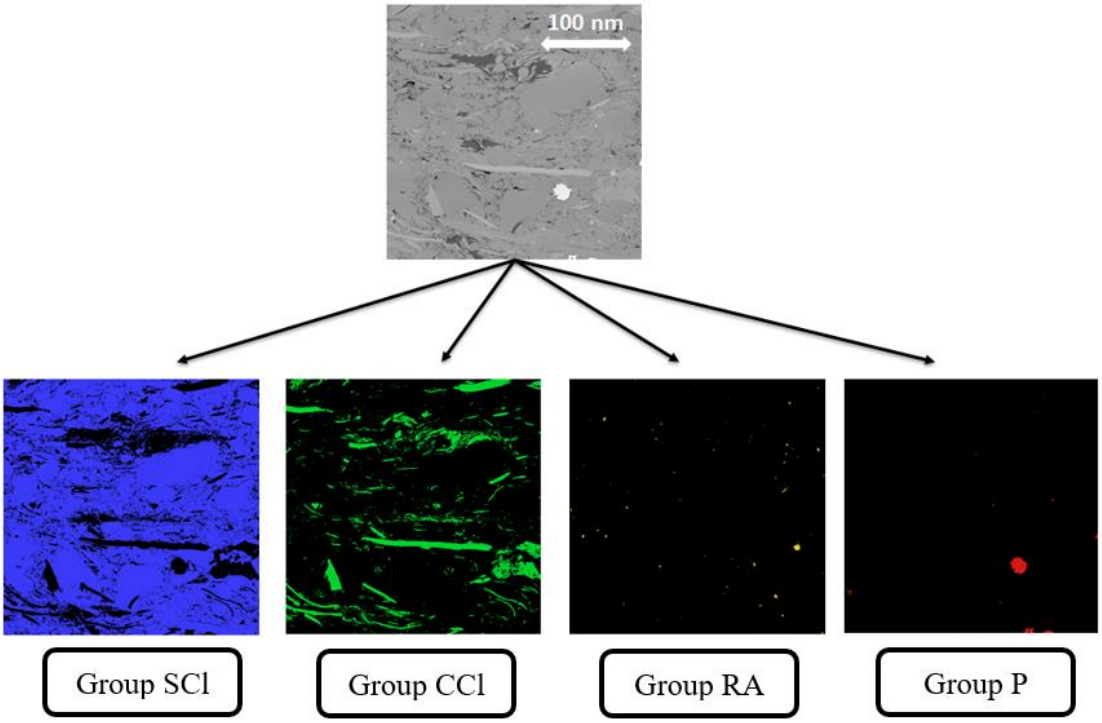

Figure 3.3: Sample #1 minerals are segmented through setting gray scale thresholds. There are 4 major mineral groups: group SCL (silica, clays, Mg-dol., feldspar), group CCL (calcite, clays, Fe-dol., K-feldspar), group RA (rutile, apatite), and group P (pyrite). These groups are highlighted in different colors with density range increasing from the left to the right.

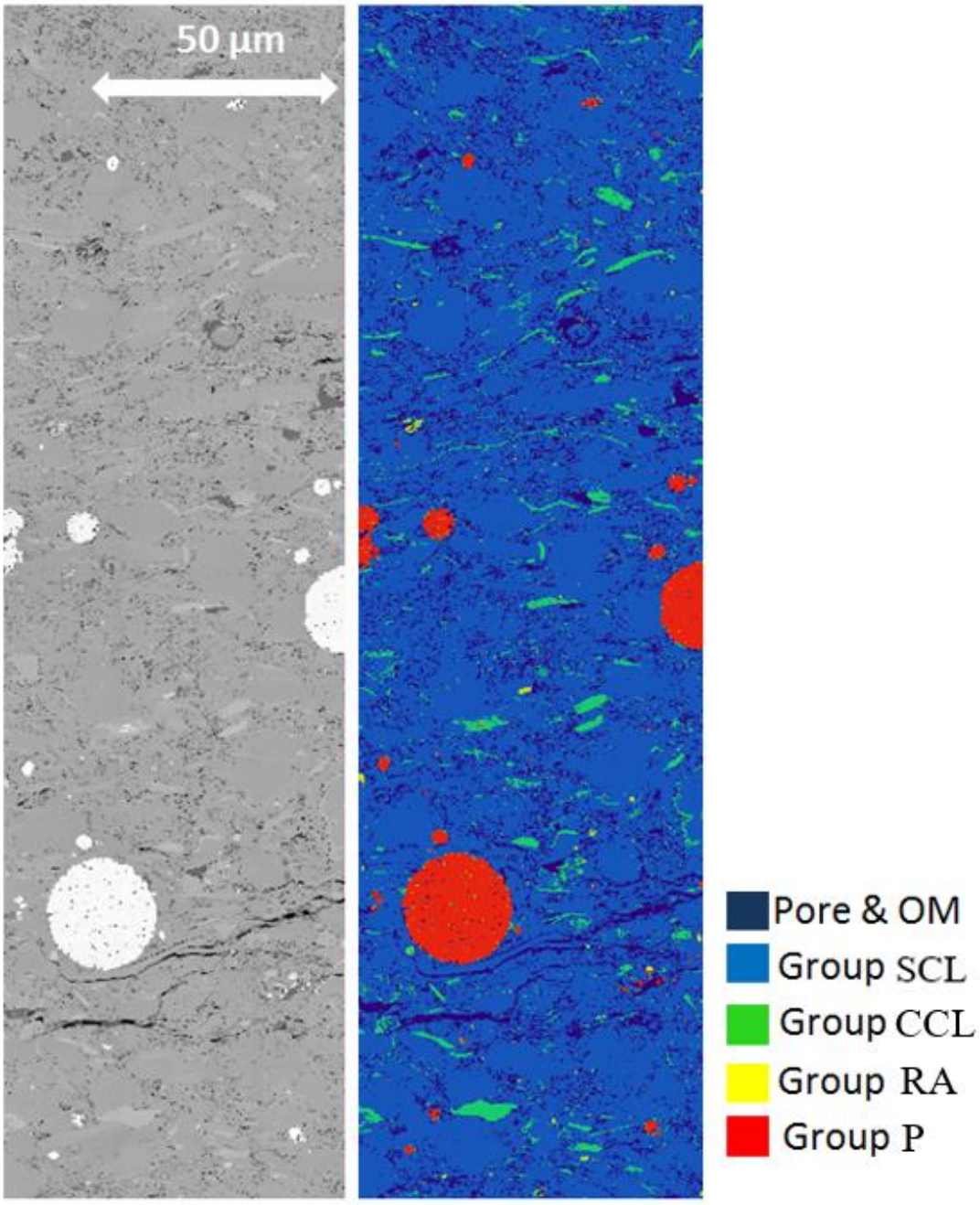

Figure 3.4: A portion of SEM map (sample #1) before and after mineralogy segmentation. There are 4 major mineral groups: group SCL (silica, clays, Mg-dol., feldspar), group CCL (calcite, clays, Fe-dol., K-feldspar), group RA (rutile, apatite), and group P (pyrite). Note the mineral distribution in shale microstructure is much easier to observe with the segmentation.

To improve the grain size distribution study, better mineralogy breakdown is required. Clays were suggested to have a much lower aspect ratio than sand grains (Xu and White, 1995). Thus, it is noticed that clay grains which present in group SCl (silica, clays, Mg-dol., feldspar) and group CCl (calcite, clays, Fe-dol., K-feldspar) have remarkably low aspect ratio compared to other grains in these two groups; it is crucial to separate clay from group SCl and CCl based on grain shape, i.e. aspect ratio. **Fig 3.5** illustrates how aspect ratio of a particle is defined. Aspect ratio is the ratio of smallest diameter of a particle to the largest dimeter orthogonal to it; it ranges from 0 to 1. A particle with aspect ratio of 1 is perfectly rounded and become more elongated when aspect ratio approaches 0. For group SCl and CCl, clay grains are highly elongated and thus have small aspect ratio compared to other grains in the same group. **Fig 3.5** shows aspect ratio histogram profile from group SCl of sample #1. Different cut-off aspect ratio values for clay – other grain separation are chosen from large to small. All particles with aspect ratio smaller than the assumed cut-off value are selected; grain size distribution for those particles are plotted. **Fig 3.6 – 3.8** shows the grain size distribution for grains from group SCl of sample #1 with aspect ratio less than 0.4, 0.35, and 0.3, respectively. When the cut-off aspect ratio is value is assumed to be 0.4, no clear trend line is observed (**Fig 3.6)**. No clear trend line is observed when the assumed aspect ratio cut-off value decreases to 0.35 (**Fig 3.7)**. When the value is 0.3, a trend between number of grain and grain equivalent radius is recognized (**Fig 3.8)**. This indicates that at this cut-off value or below, majority of grains start to follow a straight trend line. Aspect ratio of 0.3 is then defined as the cut-off where majority of grains are clays (**Fig 3.9)**.

Other grains with aspect ratio higher than 0.3 are grouped together. The complete mineralogy breakdown is shown at **Fig 3.10**

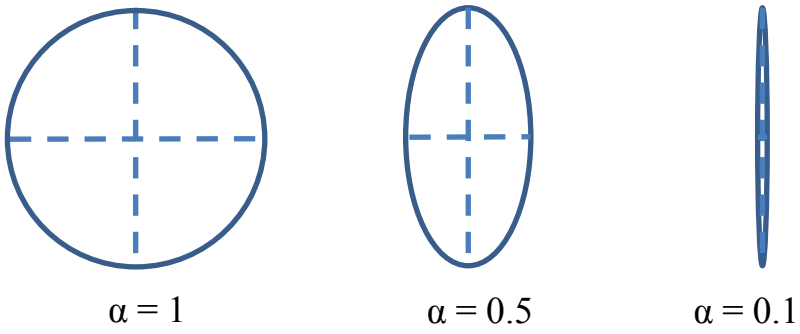

Figure 3.5: Aspect ratio is defined. Particle with aspect ratio of 1 is perfectly rounded. As the aspect ratio decreases, the particle is more elongated.

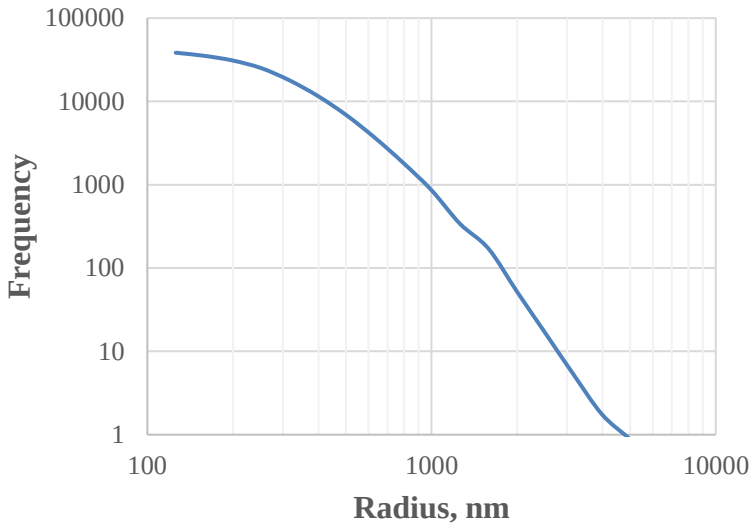

Figure 3.6: Grain size distribution of all particles with aspect ratio less than 0.4. Note no clear trend line is observed.

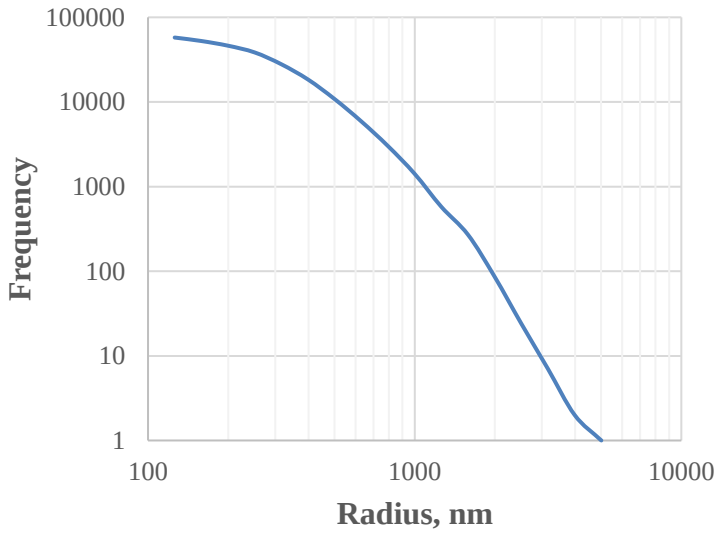

Figure 3.7: Grain size distribution of all particles with aspect ratio less than 0.35. Note no clear trend line is observed.

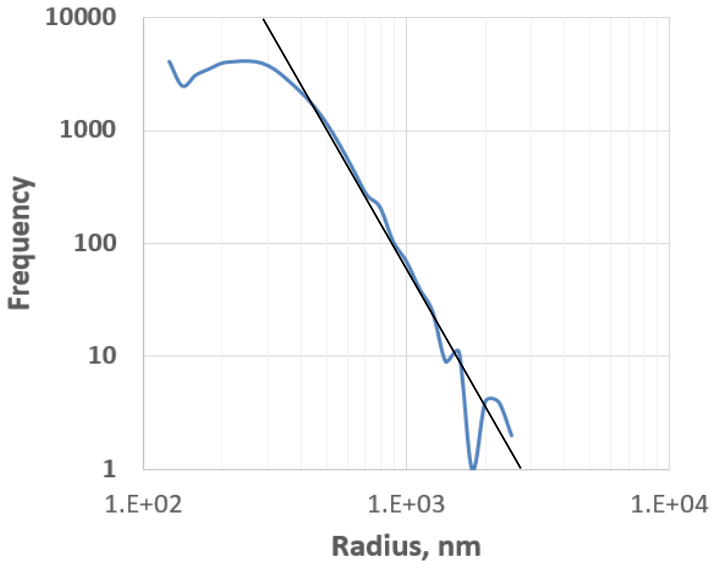

Figure 3.8: Grain size distribution of all particles with aspect ratio less than 0.3. Note a trend line is observed (black line). More fluctuation is observed due to less number of grains.

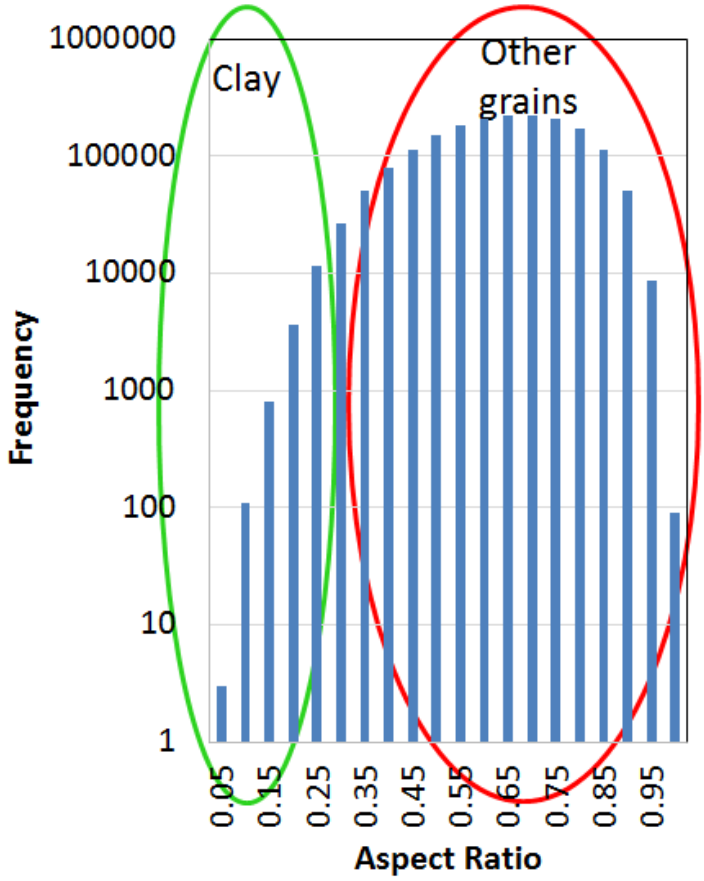

Figure 3.9: Clays are separated from other grain particles in aspect ratio histogram due to their elongated shape. The cut-off aspect ratio for separation is 0.3

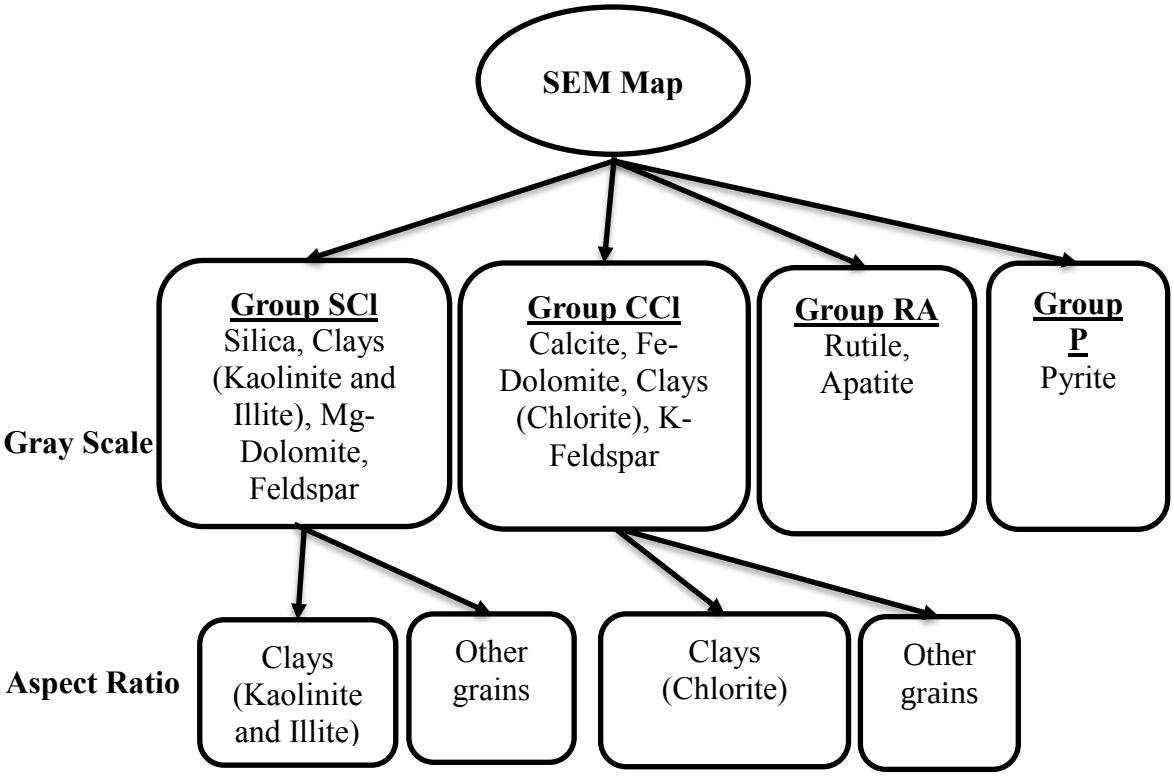

Figure 3.10: Four major mineral groups are separated from an SEM map based on gray-scale values. The minerals in each group have close or overlapping gray values. Clays are separated from other grains in group SCl and group CCl based on aspect ratio.

3.2.4 SEM Segmentation – Watershed

One of the major challenges in grain size studies is grain segmentation. Watershed segmentation is utilized to separate grains. It is applied right after the thresholding segmentation step. **Fig 3.6** illustrates how watershed can effectively define the boundary and thus distinguish two overlapping objects. From a binary image of two overlapping objects as a result of thresholding segmentation (**Fig 3.11A)**, at every pixel within the objects (white area), a distance from that point to its closest edge of the

objects is calculated. A gray scale distance image is then created (**Fig 3.11B)**; the regions at the center are darker compared to the regions near the edges as they have further distance to the edge of the objects. The distance map is treated as a topographic map. The darkness of the pixels is directly proportional to their topographic depth. The dark regions at the center are thus considered deeper compared to the brighter regions near the edges. "Water" is then progressively filled within those regions; the boundary between the two objects is decided when the water from the two regions meets (**Fig 3.11C**). **Fig 3.12** shows an example of how mineral group CCl (calcite, clays, Fe-dol., K-feldspar) is segmented from an SEM image using the watershed method. After watershed segmenting, boundaries between grain particles are successfully recognized, resulting in improved grain size analysis.

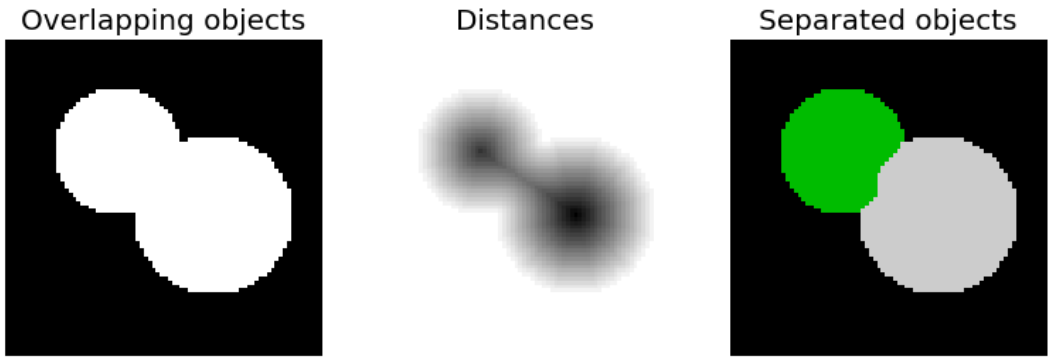

(A) **(B)** **(C)**

Figure 3.11: Illustration of watershed segmentation process – convert an image of overlapping objects (A) into a distance image (B) and finally into image with completed separated objects by progressively filling "water"

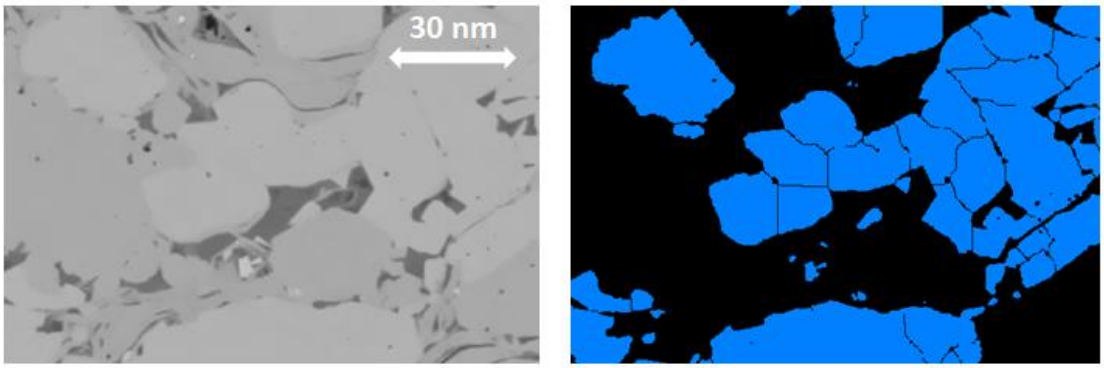

(A) **(B)**

Figure 3.12: Watershed segmentation applied to an SEM images. Mixing grains are successfully separated (group CCl (calcite, clays, Fe-dol., K-feldspar) – sample #1).

3.3 Petrophysical Measurements

3.3.1 Crushed helium Porosity Measurements

Porosity measurements were performed using the Micrometrics™ 1340 low pressure helium pycnometer (LPP). At each depth interval, four to eight grams of sample were taken and dried in the oven at 100^{o} for 12 hours for free water removal. The samples were cooled in a desiccator. The weight and volume of the samples were carefully measured. The samples were finely crushed and put into a pycnometer cell; the weight loss is allowed to be no more than 0.05%. The crushed samples were put in the oven at 100^{0}C for another 12 hours before being run in the LPP machine. During LPP run, helium is injected into the crushed sample at low pressure (approximately 20 psi). The grain volume was measured by the machine using Boyle's Law. The grain volume was corrected to account for the weight lost during the crushing procedure using:

$$V_{G_{corrected}} = V_G + \frac{\Delta m}{\rho_G}$$

The crushed helium porosity was calculated from the bulk volume and corrected grain volume of the sample:

$$\emptyset = \frac{V_B - V_{G_{corrected}}}{V_B} \; x \; 100\%$$

3.3.2 Total Organic Carbon (TOC) Measurements

TOC measurements were performed using LECO™ C844 TOC instrument. Approximately 10g of sample at each interval are used. The crushed particles were sieved with a 40 mesh sieve. The weight of each crushed sample was carefully measured. The crushed samples were washed with diluted acid (50% HCl: 50% H_2O) to remove inorganic carbon. The crushed samples were washed with deionized water to remove remaining acid. Samples were mixed with cooper and iron accelerators before being placed in the LECO™ machine. During the experiment, the samples were burned in a high frequency induction furnace; the remaining carbon (organic carbon) was oxidized to produce CO_2. The amount of CO_2 produced during the procedure is measured by infrared detectors and corresponds to the TOC in weight percentage.

3.3.3 FTIR Mineralogy Measurements

The mineralogy measurements were performed using the Thermo Scientific™ Fourier Transform Infrared Spectroscope (FTIR) in the transmission mode. The samples were finely crushed to a particles diameter less than 30 μm. The crushed samples were heated

at 100^{o}C for 12 hours to remove moisture. They were to plasma ashing for 12 hours for organic carbon removal using the Anatech™ asher. An exact amount of 0.005 g of ashed sample was mixed with 0.3g of KBr. The mixture was run in the FTIR spectrometer by making semi-transparent disc using a pellet press. An FTIR absorbance spectrum was captured as a function of wavenumber. The spectrum is inverted using partial least squares regression method to acquire the quantitative mineralogy in weight percentage.

3.3.4 Mercury Injection Capillary Pressure (MICP) Measurements

The objective of MICP test is to acquire the pore throat volume distribution. Approximately 10g of sample are used for this measurement. The samples were placed in penetrometers. The experiment consists of two stages. First, the penetrometers were inserted into low pressure port and evacuated. Small pressure (1.5 psi to 5 psi) is applied to the system that mercury was pushed to fill the stem of the penetrometer; the pressure was gradually increased until it reached 60 psi. The first stage lasted for one and a half to two hours. The penetrometer was then transfer into the high pressure port and pressurized to 60,000 psi. The equilibrium time between successive pressures is 35 sec for pressure below 27 psi and 60 sec for pressure above 27 psi; there are approximately 45 pressure steps for low pressure stage and 150 steps for high pressure stage. Mercury intrusion was measured in both stages as a function of change in the capacitance of the stem (Bocangel 2013).

3.3.5 Nuclear Magnetic Resonance (NMR) Measurements

NMR experiments record the interaction of an external magnetic field, the spin angular momentum and magnetic moment of hydrogen atoms. As a magnetic field is applied, the magnetic moments of atoms become aligned with the applied field. When the applied field is removed, the hydrogen atoms experience relaxation; eventually approaching a new equilibrium. The ratio between high and low energy atom populations during the transition between equilibrium stages produces a signal that can be used to characterize petrophysical properties such as porosity, water saturation, fluid type, and wettability (Odusina, 2011).

During NMR experiments, net magnetization of hydrogen atoms is measured with the present of external magnetic field (Kleinberg et al., 1993; Howard, 1994; Dunn et al., 2002). The NMR relaxation time T_2 is defined as:

$$\frac{1}{T_2} = \frac{1}{T_{2\,bulk}} + \frac{1}{T_{2\,surface}} + \frac{1}{T_{2\,diffusion}}$$

where $T_{2\ bulk}$, $T_{2\ surface}$, and $T_{2\ diffusion}$ are bulk fluid relaxation, surface relaxation, and diffusion relaxation, respectively. With the use of fast measurement timing and homogeneous magnetic field, surface relaxation dominates in a fast diffusion limit (Dunn et al., 2002) The equation becomes:

$$\frac{1}{T_2} \simeq \frac{1}{T_{2\,surface}} = \rho \frac{S}{V}$$

where ρ is surface relaxivity, S is pore surface area, and V is pore volume.

The objective of NMR experiments is to acquire the pore body size distribution. The measurements were made on the one-inch dimeter samples taken at each interval of the core section using a 2 MHz benchtop system. The value for half of the echo spacing τ is selected as 0.057 ms. All of the samples are kept at native state saturations.

3.3.6 Overview - Petrophysical Measurements

Measurements of thermal maturity, crushed helium porosity, TOC, and FTIR mineralogy were performed on all 24 Wolfcamp samples. Thermal maturity from source rock analysis showed an average T_{max} value of 451^{o}C which indicates that these samples fall into the peak wet gas window (Dow, 1977). **Fig 3.13** shows the helium porosity, TOC, and FTIR mineralogy results with the increasing depth. Low pressure crushed sample helium pycnometer porosity values ranged from 7.8 – 11.0 %. LECO™™ TOC values ranged from 2.0 – 6.0% by weight. Transmission FTIR spectroscopy indicated mineralogy is dominated by clay (55-75 wt%), which is mostly illite, following by quartz (8-25 wt%), feldspar (approximately 10 wt%), and carbonate (approximately 5 wt%). Overall, the mineralogy is fairly homogeneous over the 1 ft interval, especially the clay content. Porosity distribution with T_2 relaxation from NMR data is consistent throughout the 1 ft section (see **Fig 3.13**). For the plot of each sample, a dominant signal of clay-bound water at extremely fast relaxation time (0.7 – 1 ms) following by a smaller broad peak of adsorbed fluid at 50-60 ms indicates the dominance of clay porosity (Goergen et al., 2014). Available MICP data of 21 samples

also shows a strong consistency within this section (see **Fig 3.13**); the diameter of most of the pores ranges from 4 to 8 nm.

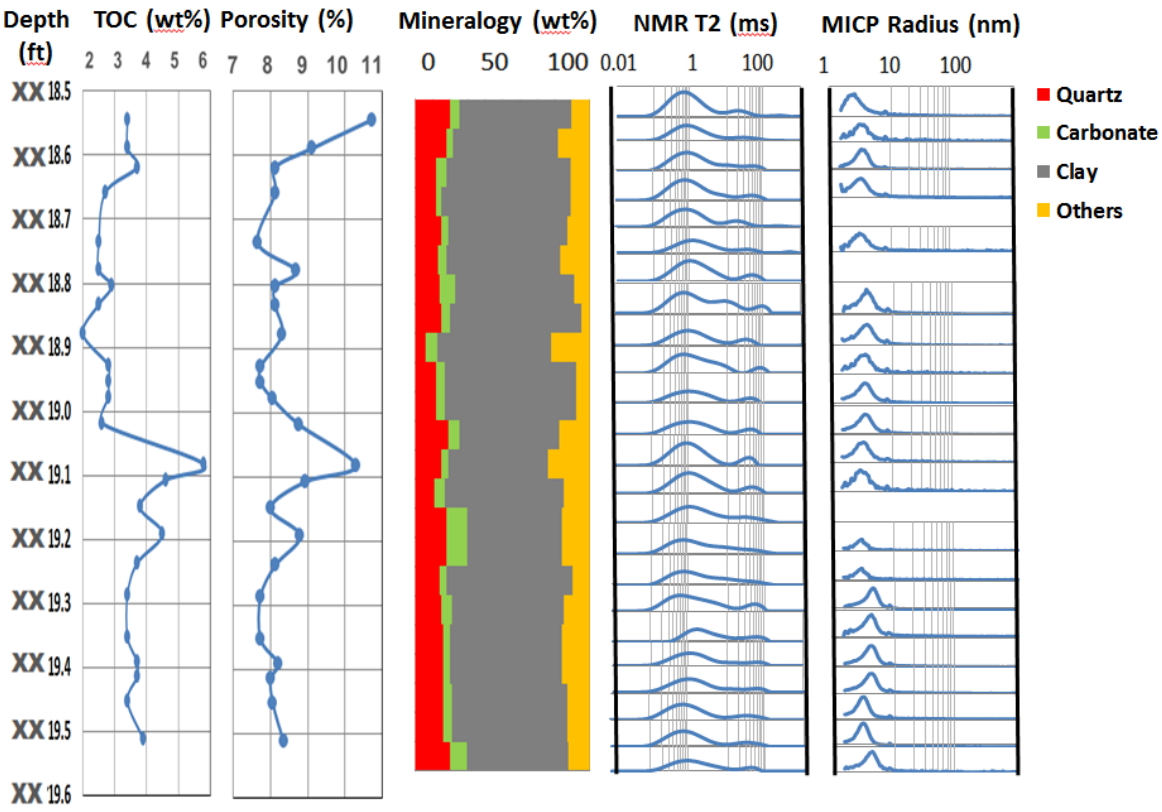

Figure 3.13: Measured TOC, crushed helium porosity, FTIR mineralogy, NMR T2 distributions, and MICP for the 24 samples plotted against increasing depth over the one-foot depth interval. Note that the mineralogy is dominated by clay, predominately illite

Chapter 4: Results and Discussion

This chapter presents the results of three studies from SEM imaging analyses. The first study investigates the appropriate representative elementary areas (REA) required for imaging various microstructural components including porosity, organic matter, and mineral grains. The second focuses on the size distribution for each of these components. Finally, the third study involves the correlation between the imaging data and other petrophysical data including crushed helium porosity, TOC, MICP, and NMR.

4.1 Pore and Organic Matter

4.1.1 Representative Elementary Area

From one map, which has the standard dimensions of 273 μm width and 6,000 μm length (1.56 mm^2 area) stitched from approximately 3,000 SEM images taken at 10 nm resolution; multiple sub-maps of different sizes selected at random locations were extracted for comparative analyses. The 2D SEM porosities of these sub-maps were calculated using the segmentation method described previously and were compared with the segmented porosity value of the entire original map. **Fig 4.1A** shows an example result from sample #5. The area of original map of this sample is 1.56 mm^2. A large fluctuation of the porosity is observed for small sub-maps (especially below 10% of the original map). As the size of the sub-maps increases, the porosity values converge to the porosity of the whole map for sample #5. **Fig 4.1B** shows the truncation error of the porosity of each sub-map compared to the porosity of the whole map. Truncation error of sub map at scale i, E_i is defined as:

$$E_i = \left| \frac{\Phi_i - \Phi_{map}}{\Phi_{map}} \right| * 100$$

where ϕ_i is the porosity at scale i and ϕ_{map} is the porosity of the entire map image. At the scale of 22% of whole map which is equivalent to an area of 0.32 mm^2, all porosity values are almost the same and close to the porosity of the whole map. This area is roughly equivalent to a 550 µm x 550 µm image. At this size of sub-map or larger, the truncation errors are 10% or less. Note that the acquisition time for the whole map of 1.56 mm^2 is approximately 66 hours for the acquisition parameters used, e.g., dwell

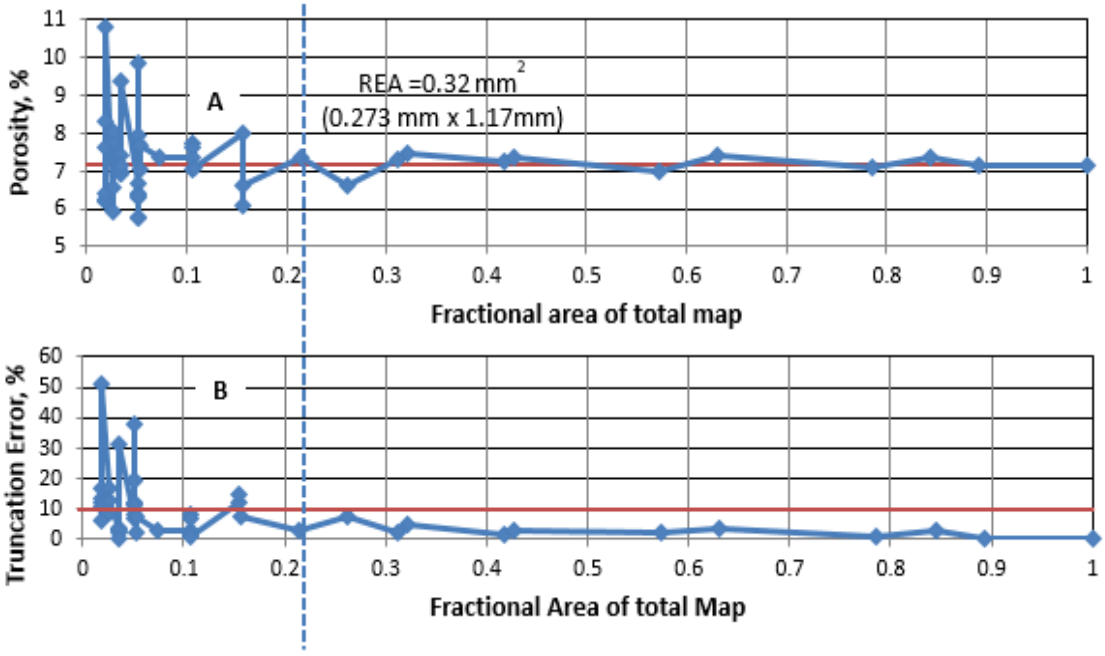

Figure 4.1: A) Porosity measured from SEM map (sample #5) for different sub-map areas is compared to total porosity for the original map (red line), B) Truncation errors of each porosity value is compared to 10% truncation error (red line). Note beyond a map area of roughly 20% of the whole map, the difference in porosity estimates reduces and become acceptable.

time and resolution. Collecting a map of 0.32 mm^2 requires only 15 hours and still provides a representative porosity result. In addition to the acquisition time, the image processing time for feature extraction is much less.

The REA study is also performed for organic matter on the same sample (**Fig 4.2A**), using the same the cut-off of 10% truncation error or less (**Fig 4.2B**). A similar trend is observed: the organic matter content by area fluctuates at small sub-map sizes and converges toward the organic matter content of the whole map as the size increases. However, the REA for organic matter was determined to be 80% of the original map (approximately 1.09 mm^2) which is significantly larger than the REA for porosity of the same sample. The minimum map area required to representatively capture the organic matter content for sample #5 is about three times larger than for porosity.

The REA values for porosity and organic matter content for the 24 Wolfcamp Shale samples are showed in **Fig 4.3**. Throughout the one-foot core section, variations in REAs are observed for both porosity and organic matter, which reflects the degree of heterogeneity of the formation. With one exception, the minimum required imaging area for porosity is smaller than for organic matter content. REA for porosity ranges from 0.2-0.8 mm^2 with the average of 0.5 ± 0.2 mm^2; REA for organic matter ranges from 0.6 – 1.2 mm^2 with the average of 1.0 ± 0.2 mm^2.

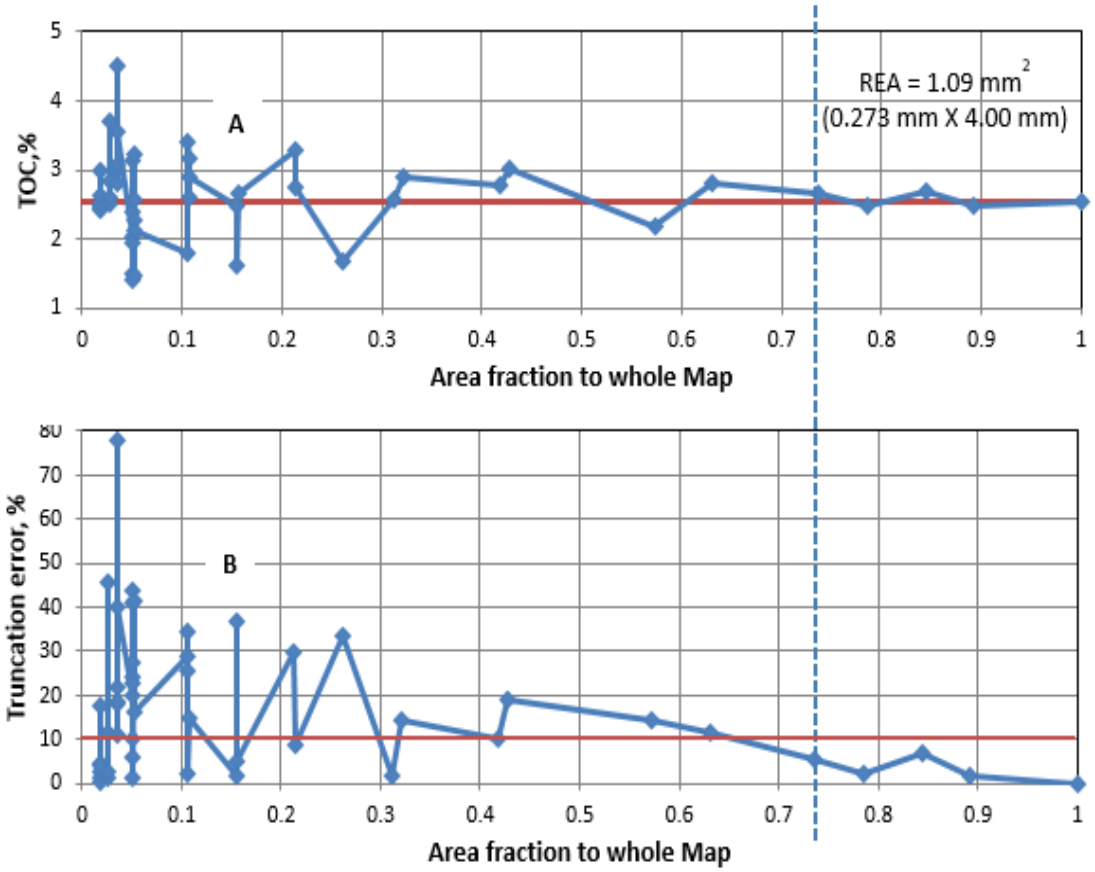

Figure 4.2: A) Organic matter content measured from an SEM map of sample #5 for different sub-map areas is compared to the total organic matter content for the original map (red line), B) Truncation errors of each TOC value is compared to 10% error (red line). Note beyond a map area of roughly 70% of the total area, the difference in TOC estimates reduces and become acceptable. Note also this area threshold is considerably larger than that for porosity.

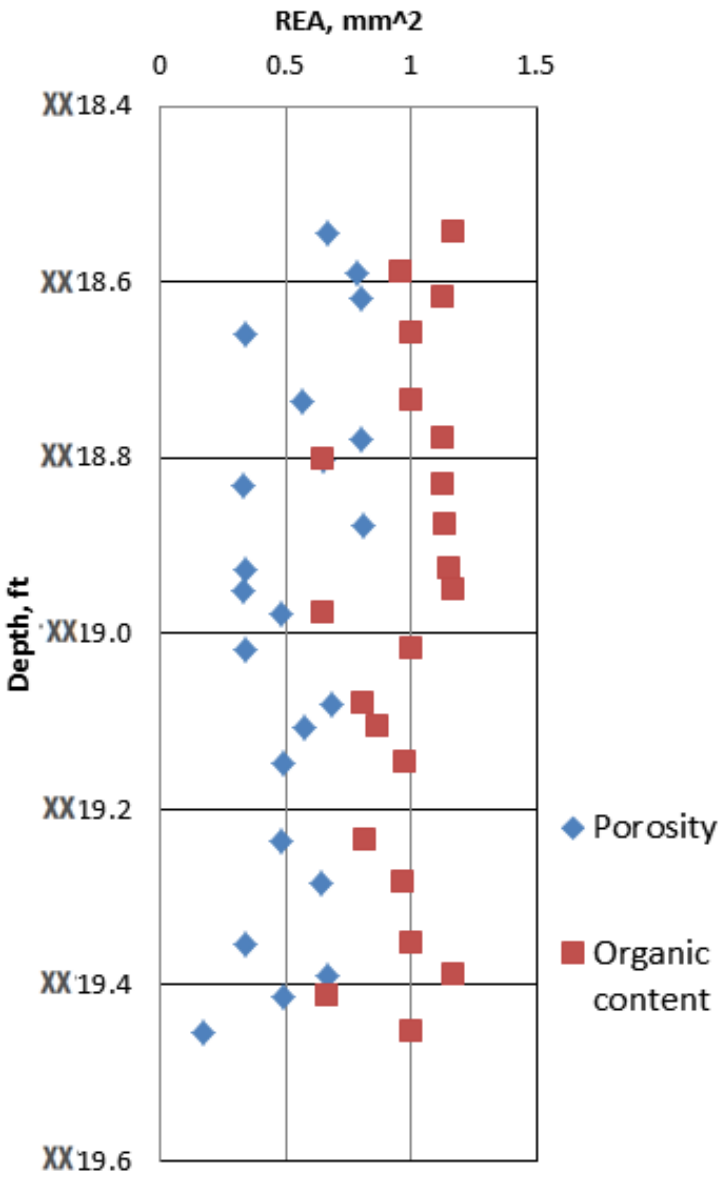

Figure 4.3: REA for porosity and organic content for 24 samples with depth. These are estimated from the whole maps. In general, the REAs for organics are roughly twice that for porosity.

4.1.2 Pore and Organic Matter Size Distribution

Pore size distribution studies of 3D shale microstructure using FIB/SEM system indicated that the number of pores decreases with increasing pore body radii assuming spherical pores (Curtis et al., 2010; Giffin et al., 2013; Goral et al., 2015). Do these 3D observations translate into 2D? **Fig 4.4** shows the pore size distributions plotted for all 24 Wolfcamp samples. The distributions were determined from the entire map acquired for each sample. The number of pores appears to be inversely proportional to an equivalent spherical pore body radius on a log-log scale. All 24 pore size distributions follow a similar trend wherein small pores dominate in number. The pore size distribution shows consistency throughout the 1 ft section. Unlike the variations observed in REA studies for porosity and organic matter, a single sample in this one-foot section is necessary for estimating the pore size distribution. The result of small pore domination strongly agrees with the earlier pore size distribution from the smaller scale 3D SEM reconstructions (Curtis et al., 2010; Giffin et al., 2013; Goral et al., 2015). As the pore body radius approaches the SEM resolution of 10nm, the data deviates from the observe trend. Undersampling in which there is insufficient pixel density to determine the structure of any element near the resolution of an image is responsible for the underestimation (Curtis et al., 2010). The distribution of organic matter particle sizes was also studied (**Fig 4.5**). The result shows a similar trend to pores as small organic matter particles dominate in number with the number of organic matter particles decreasing proportionally with the increasing equivalent spherical radius. A greater separation in the size distributions is observed for the organic matter than for the

pore size distributions. **Fig 4.6** shows an example of the variation of organic distributions. Most of organic matter particles from sample #5 (**Fig 4.6A)** are relatively small in size and fill between the clays. However, from sample #13 (**Fig 4.6B),** apart from small organic matter particles between the clays, a number of larger organic matter particles is observed (highlighted in red circles). Most of these particles are associated with cracks. The distribution parallel to bedding would be expected to have different distributions and REAs.

Assuming spherical pores and organic matter, the pore and organic matter size distribution plots are converted into areal contribution plots, respectively (**Fig 4.7**). The area contributions show that larger pores dominate in area with more than 80 % of pore area coming from pores with radius larger than 50 nm despite dominating by smaller pores. For organic matter particles, particles with radius smaller than 50 nm still contribute up to 35% of total area. One reason for this significant amount of small organic matter is because the selected one-foot core is clay-heavy in mineralogy and imaging suggests there are a lot of organic matter particles filling in the small regions within the clay network. When the areal contribution plots of pore and organic matter are combined, it is observed that pore area is generally larger than organic matter area. Total pore area can be up to 10 μm^2, while it is 7 μm^2 for organic matter. The average pore radius for the 24 samples ranges from 200 to 380 nm, while the average organic matter radius ranges from 70 to 180 nm. This suggests that most of the pores are located outside of the organic matter, i.e. they are mostly mineral-associated pores.

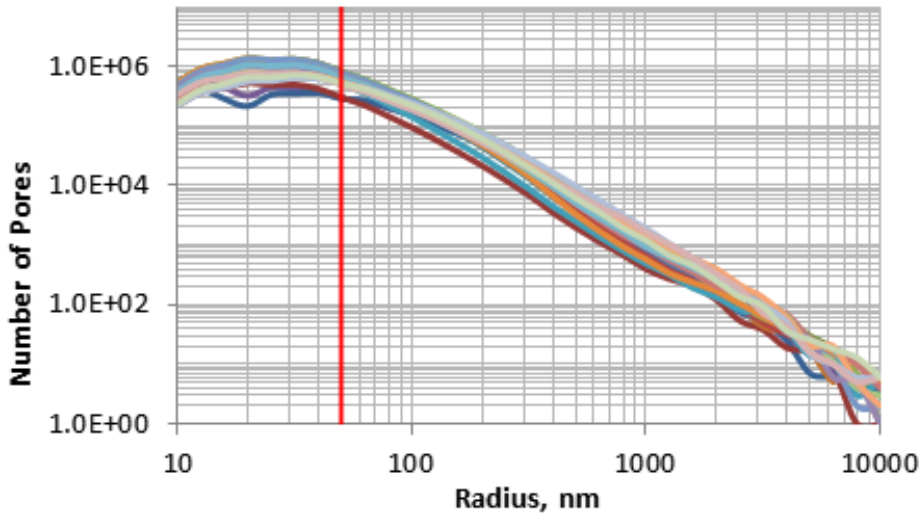

Figure 4.4: Pore size distribution for 24 samples with 50 nm radius boundary (red line). Note the similarity in the trend for 24 samples. Note the assumption of spherical pores.

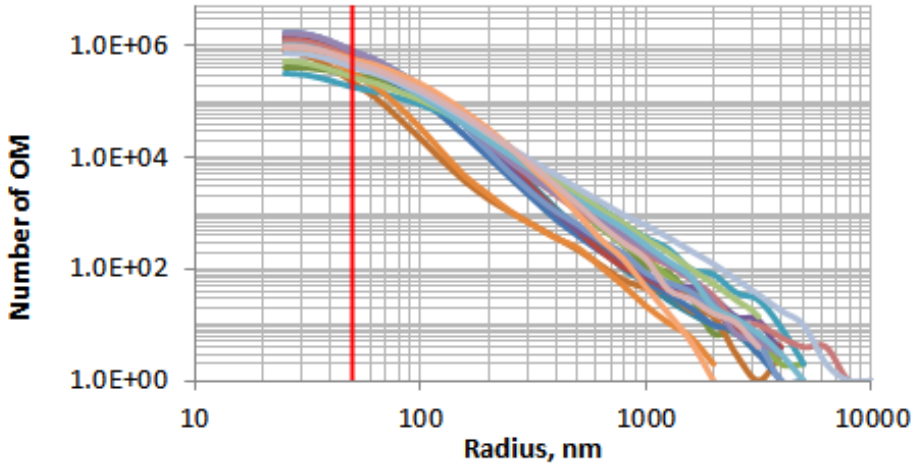

Figure 4.5: Organic matter size distribution for 24 samples with 50 nm radius boundary (red line). There is more scatter in the organic trends than the porosity trends. Note the assumption of spherical organic matter.

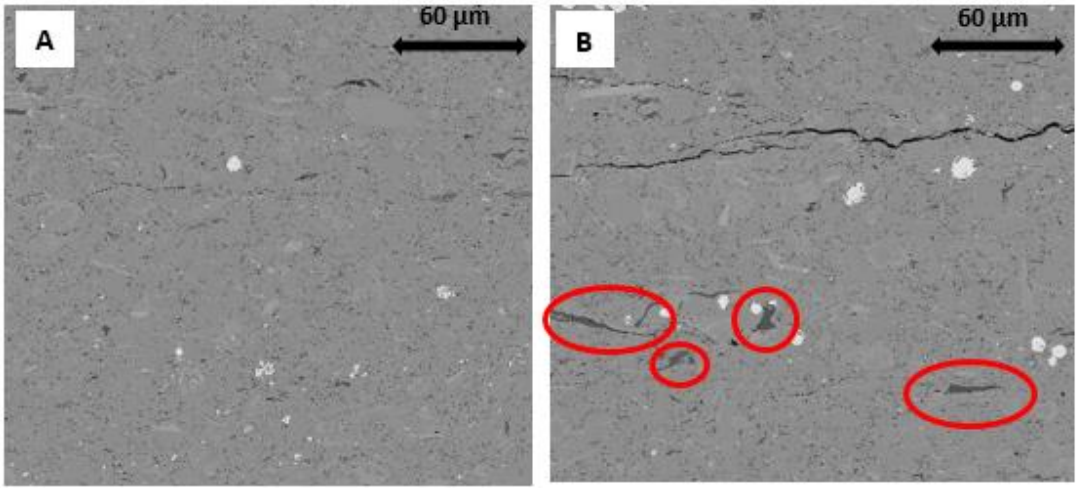

Figure 4.6: SEM backscattered images of A) sample #5 and B) sample #13. Red circles highlighted larger organic matter particles which are mostly associated with cracks. These organic filled cracks are important and considered as key to HC generation.

Pore and organic matter size distributions of each sample were studied at different scales. Three sub-maps of 10% scale (273 µm x 571 µm) which totally cover 30% area of the whole map of sample #5 are randomly selected. **Fig 4.8A** shows the pore size distribution plots of these three sub-maps. The same trend is observed as with the pervious pore size distributions (**Fig 4.4**) in that there is an inversely proportional relationship between number of pores and equivalent pore body radii on a log-log scale. The three distributions almost overlay and contain an almost equivalent total number of pores. The pore size distribution thus is very consistent at this sub-map scale. Breaking the map down to a smaller scale, six pore size distribution plots of six sub-maps of 5% scale (273 µm x 286 µm) at random locations are reported in **Fig 4.8B**. A similar trend

is observed for these plots, i.e. that number of pores decreases with increasing pore radius. A greater variation is observed because of higher standard deviation of total number of pores. However, the percentage deviation is always less than 5%. This suggests that to study pore size distributions, only a small area of ~5% scale for imaging is necessary. As for this 1 ft core section, the area needed to capture pore size distribution would be smaller than the area required to capture the total porosity (REA).

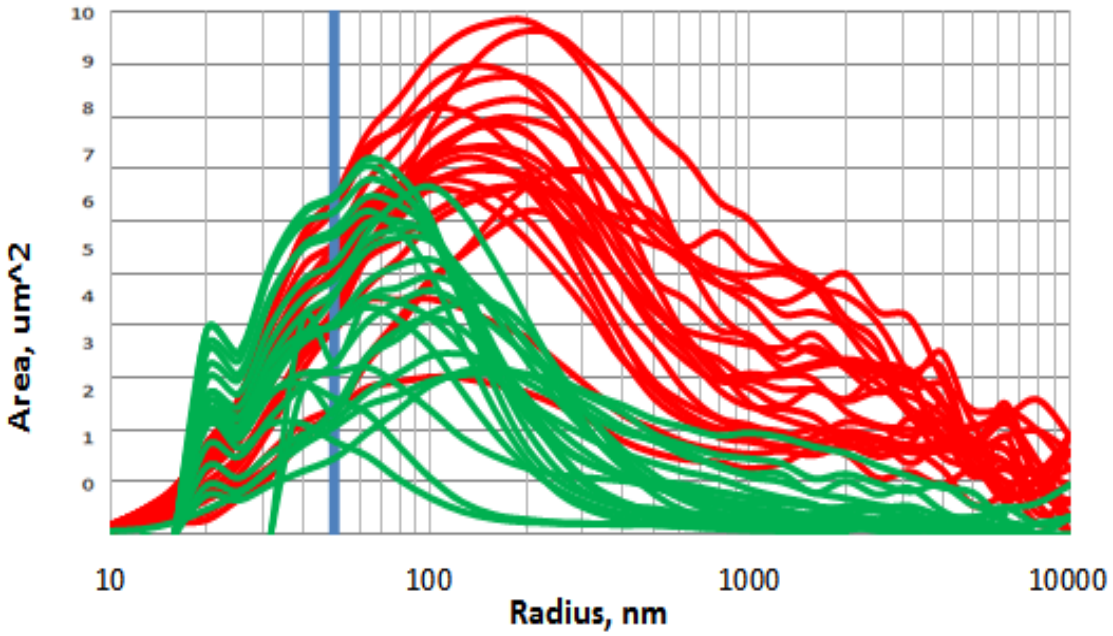

Figure 4.7: Areal contribution of porosity (red) and organic matter (green) for 24 samples assuming a 50nm radius boundary (blue line). Note the assumption of spherical pores and organic matter.

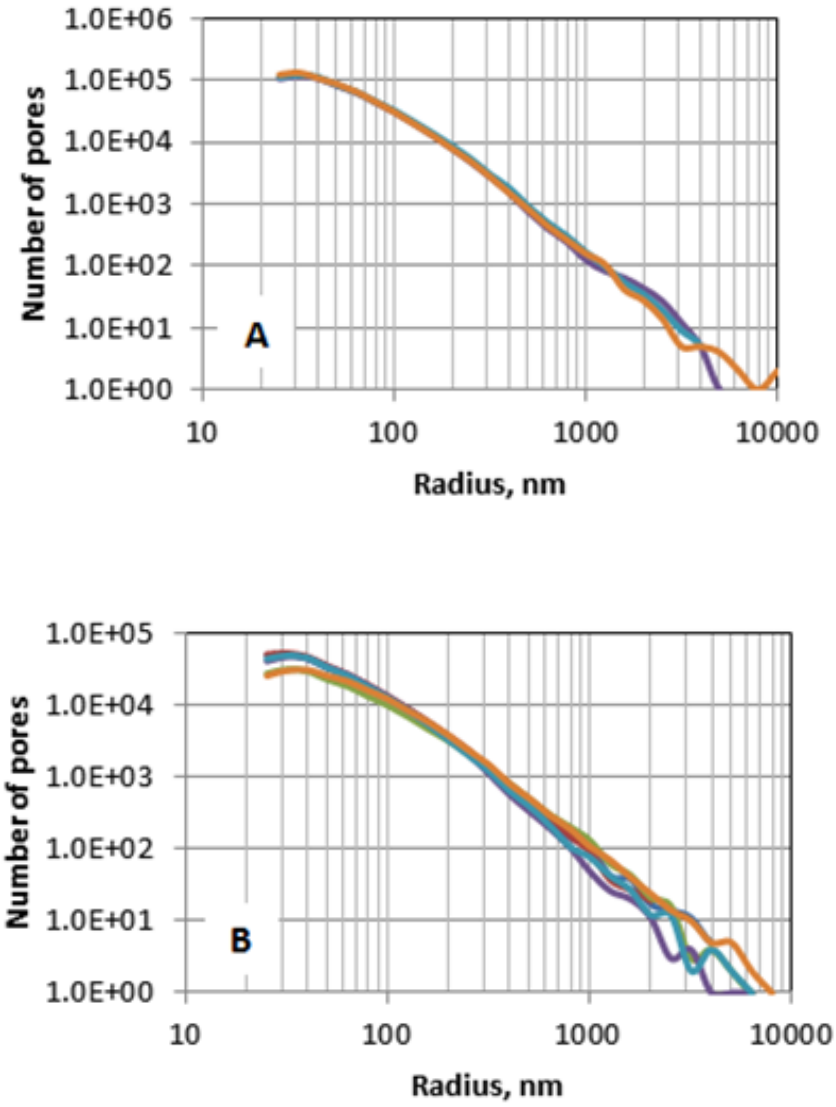

Figure 4.8: Pore size distribution of A) three sub-maps of 10% scale, average number of pores counted is 627,000 ± 17,000 and B) six sub-maps of 5% scale, average number of pores counted is 228,000 ± 39,000. Note variation at large size.

4.1.3 Imaging Data versus Petrophysical Data (Crushed helium Porosity and TOC)

Since porosity and organic matter studies utilizing SEM imaging are performed on a relatively small scale, it is important to correlate the results with those from petrophysical measurements which are performed at a larger scale. Petrophysical data including crushed helium porosity and TOC measurements are compared with the porosity and organic matter estimates derived from SEM data for the 1 ft section of Wolfcamp Shale core (**Fig 4.9** and **Fig 4.10**). There are differences between the SEM derived data and the lab petrophysical measurements, some are expected based on the modes of measurements. Helium porosity measurements yield a volume percentage whereas the SEM analysis yields an areal percentage. Organic matter content derived from the SEM is also an area percentage whereas in TOC measurements it is a weight percentage. Overall, a similar trend between imaging data and petrophysical data are observed for both porosity and organic content. The average difference between SEM porosity and helium porosity is 1.0%; the average difference between SEM TOC and LECO™™ TOC is 0.6%. Assuming the formation is weakly heterogeneous, it is very promising to predict these petrophysical data from SEM imaging analysis. There is a small interval highlighted by ellipses where the correlation is fairly poor for porosity (red ellipse) as well as organic content (green ellipse). These anomalies can be attributed to the high degree of heterogeneity in this interval.

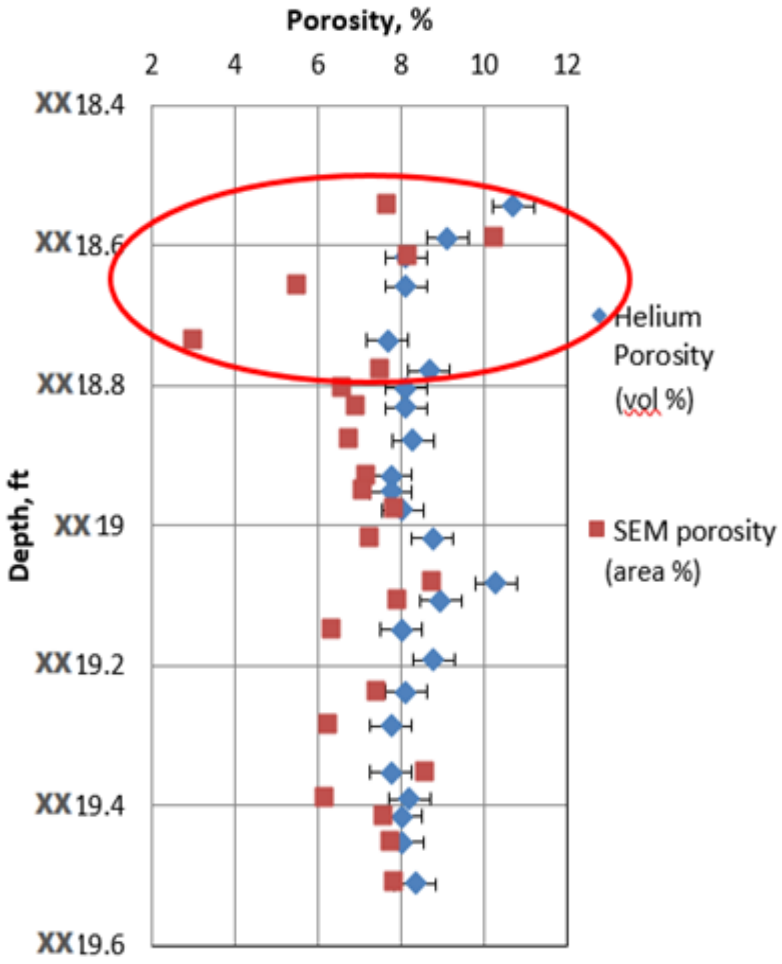

Figure 4.9: Comparison of porosity measured from SEM imaging and petrophysical data. Red ellipse highlights the interval with the poorest correlation. The error is 1.0% on average. Note SEM porosity values are measured from the whole maps.

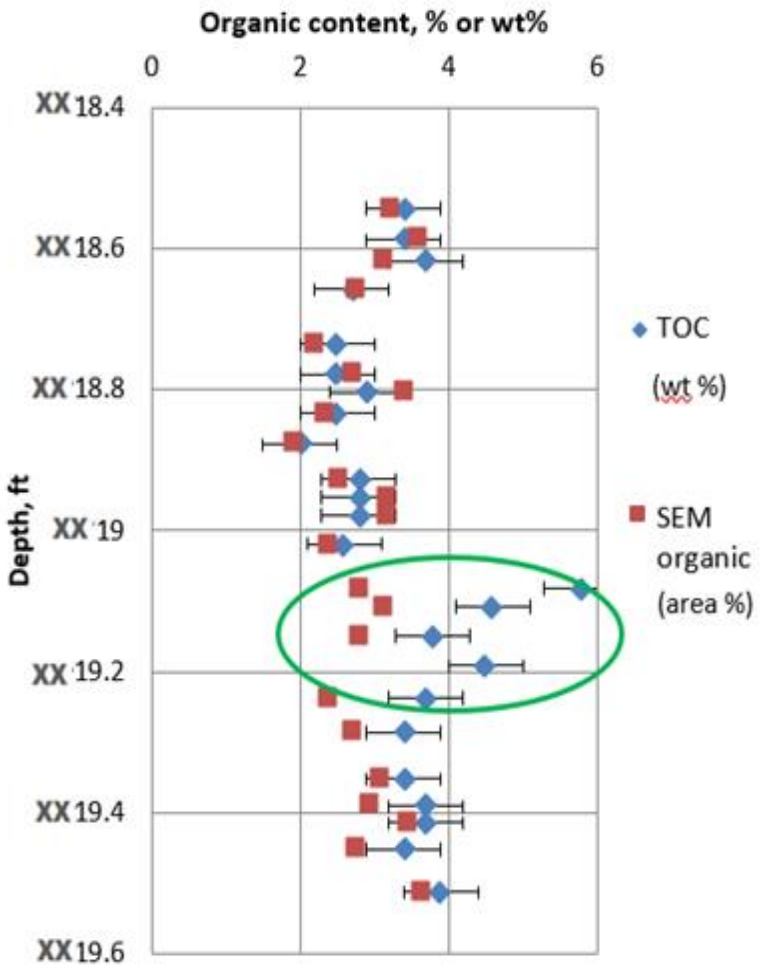

Figure 4.10: Comparison of organic content measured from SEM imaging and petrophysical data. Green ellipse highlights the interval with the poorest correlation. The error is 0.6% on average. Note the SEM TOC values are measured from the whole maps.

Fig 4.11 shows an SEM image from sample #3 which is located within the interval highlighted by the red ellipse in **Fig 4.9.** The SEM porosity measured on this sample is significantly lower than the helium porosity measured on cores taken in this interval. Compared to samples outside the interval, the majority of the pores and cracks for this

sample are relatively small. Limited number of large pores and lack of major fractures are some of the main reasons for the lower SEM porosity. **Fig 4.12** is an SEM image from sample #13; the size of organic matter in this sample varies over a considerable range; numerous large particles can be observed, resulting in fairly high organic matter content. However, TOC measurement for this sample is significantly greater than the estimation from SEM images.

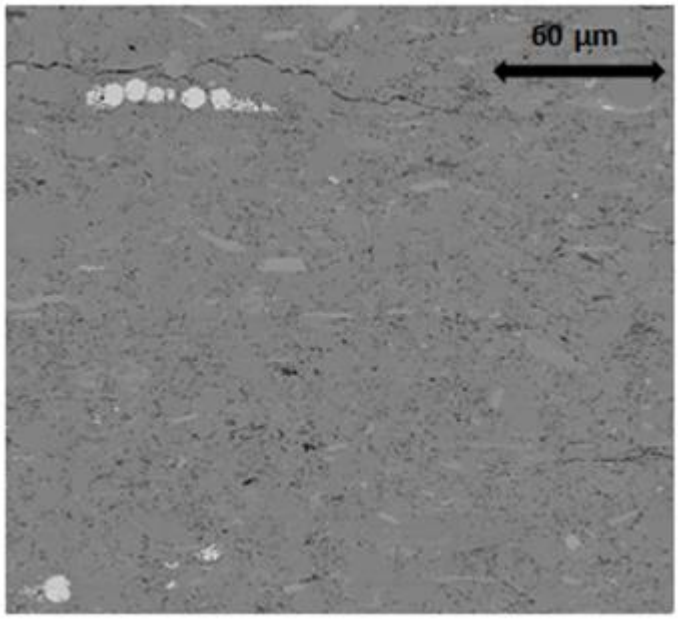

Figure 4.11: SEM backscattered image of sample #3. SEM porosity and crushed helium porosity measured for this sample are 3.0% and 7.0%, respectively. Lack of large pores and fractures results in low SEM porosity.

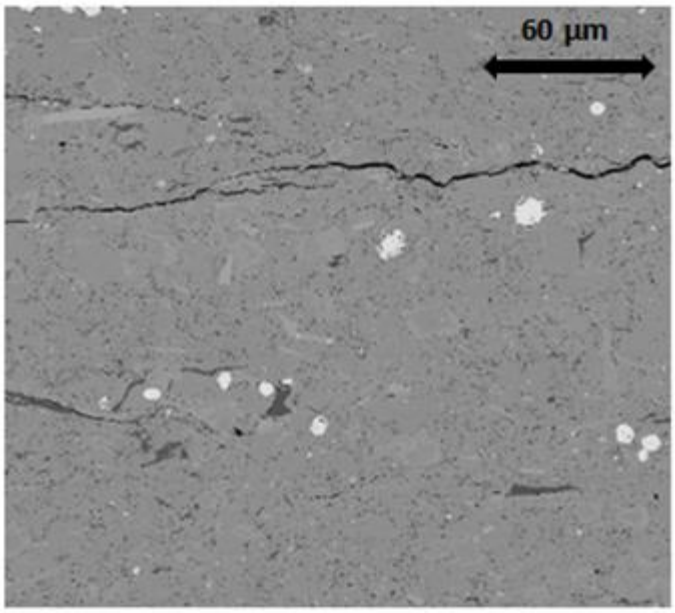

Figure 4.12: SEM backscattered image of sample #13. SEM TOC and LECO™ TOC measured for this sample are 2.4% and 3.8%, respectively. SEM TOC is smaller than LECO™ TOC despite numerous of large organic matter particles.

4.1.4 Imaging Data versus Mercury Injection Data

Mercury injection capillary pressure (MICP) measurements were performed on the Wolfcamp samples. During this experiment, mercury is injected into the sample in defined pressure increments from 5 to 60,000 psi. During the gradual pressure release, mercury extrusion is also recorded as a function of pressure. **Fig 4.13** shows the combination of intrusion and extrusion plots for sample #1. The difference between intrusion and extrusion data highlighted by black arrow proves that a significant amount of injected mercury is trapped inside the rock sample. Pore connectivity is the main reason for this trapped mercury. MICP model is interpreted under the assumption that

all of pores are cylindrical capillaries throughout the sample (**Fig 4.14**), whereas in reality, pore with different sizes are connected together (**Fig 4.14**). Large pores where most of fluid is stored are considered pore body while much smaller pores are considered pore throat as they help connecting the pore bodies together. The mercury trapped recognized from **Fig 4.13** is believed to be located inside the pore bodies.

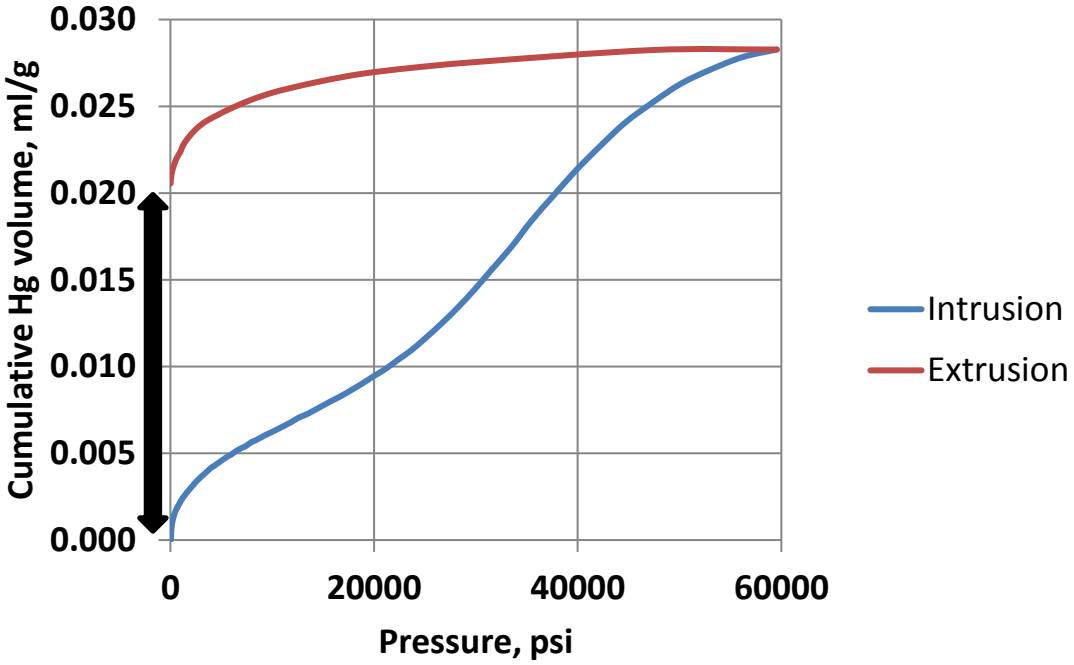

Figure 4.13: Mercury intrusion and extrusion as a function of pressure of sample #1. Black arrow indicates the difference between intrusion and extrusion profile, which represent the amount of mercury trapped inside rock sample.

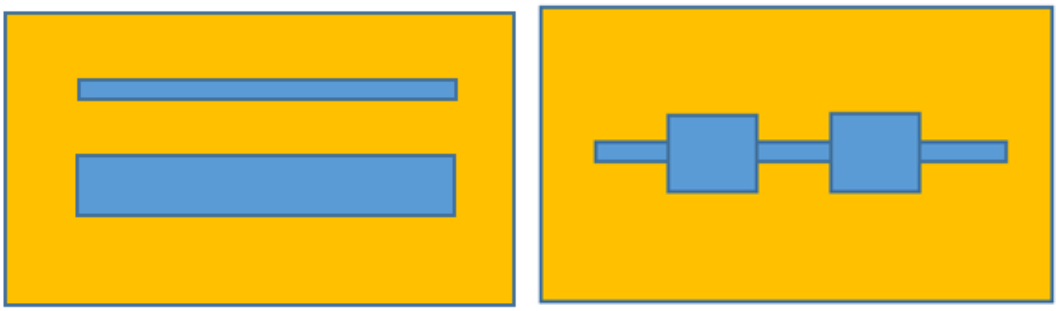

Figure 4.14: MICP model assumption that all pores (blue) are homogeneous in size (left figure) versus real life scenario where pores with different sizes are mixed together

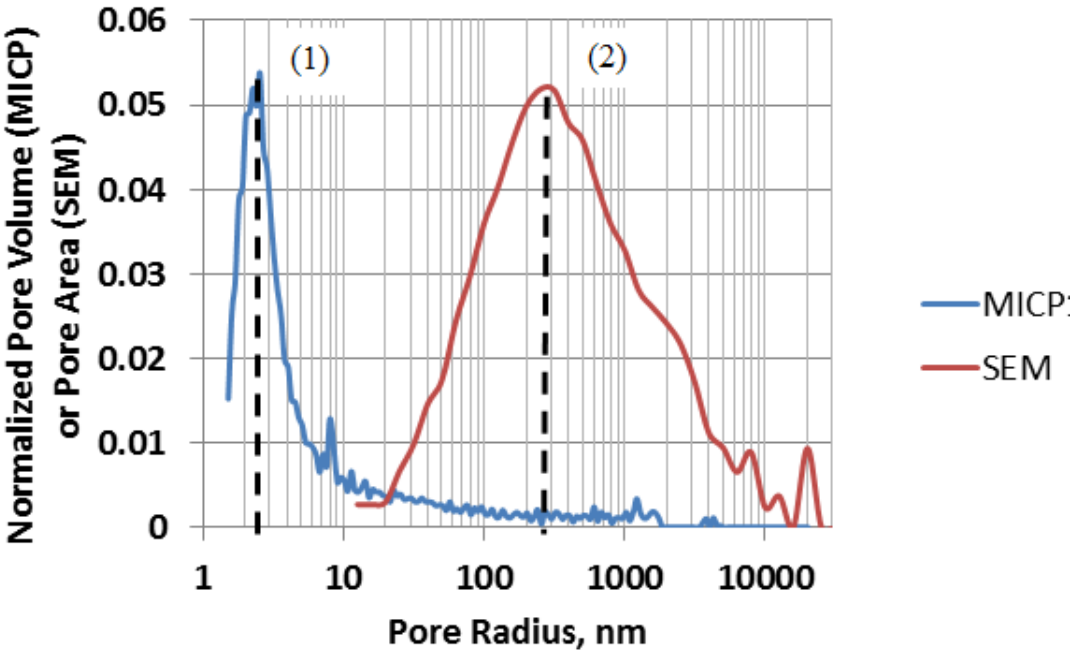

Figure 4.15: Comparison of MICP pore volume distribution and SEM imaging pore area distribution of sample #1. While each distribution has one dominant peak, they are not at the same pore radius.

While MICP results provide pore throat access volume distribution, pore area is acquired from SEM imaging data. It is necessary to combine these two to fully understand the pore distribution. It is worth noticing that MICP is able to provide information at better resolution (3 nm) compared to SEM imaging (10 nm). An example for sample #1 is showed (**Fig 4.15**). The two plots do not match; instead, two distinctive peaks are observed. The MICP peak (1) is expected to represent pore throats, while the SEM peak (2) is expected to represent the pore bodies. Fig 4.16 shows the MICP/SEM combination for all of the 24 Wolfcamp samples. Both MICP and SEM plots show strong consistency between the samples as two distinctive groups of peaks are observed. From MICP data, the diameter of most of pore population ranges from 4 to 8 nm; from SEM data, the diameter of most of pore population ranges from 200 to 400 nm. Do the difference between MICP and SEM data related to the difference between mercury intrusion and extrusion profiles? To answer that, the ratio between pore body from SEM distribution and pore throat from MICP distribution is plotted with the intrusion/extrusion difference for each of the samples (**Fig 4.17**). The amount of mercury trapped inside the pore system appears to be directly proportional to the ratio of pore body to pore throat. This result strongly agrees with earlier study by Wardlaw and McKellar where experimental evidence is presented from glass micromodels and from reservoir rocks that the volume of residual mercury trapped during pressure reduction increases as pore to throat size ratio increases (**Fig 4.18**). It can be concluded that MICP is able to provide information about pore throats that SEM imaging is unable to acquire due to resolution limitation.

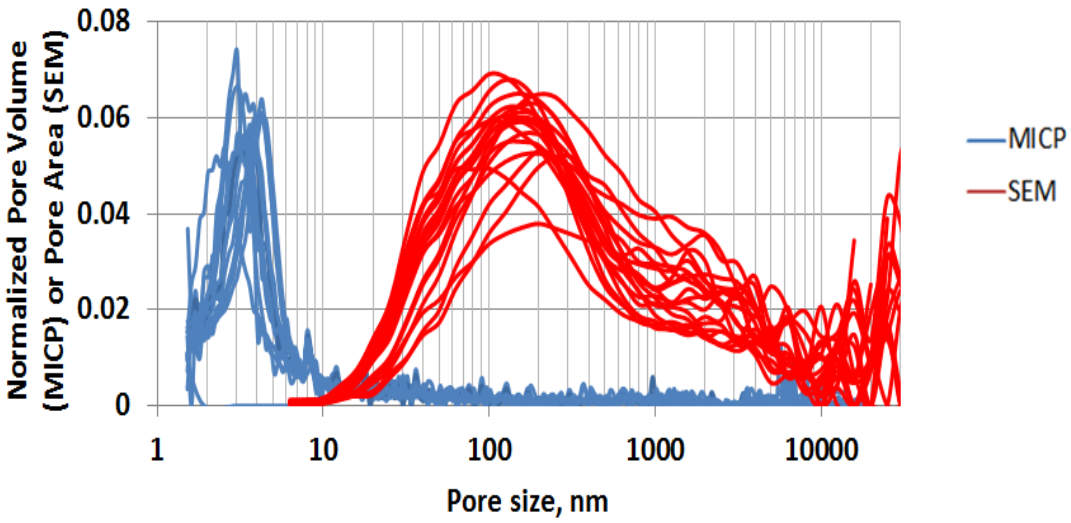

Figure 4.16: Comparison of MICP pore volume distribution and SEM imaging pore area distribution for the 24 Wolfcamp samples. Two separate peaks are still observed.

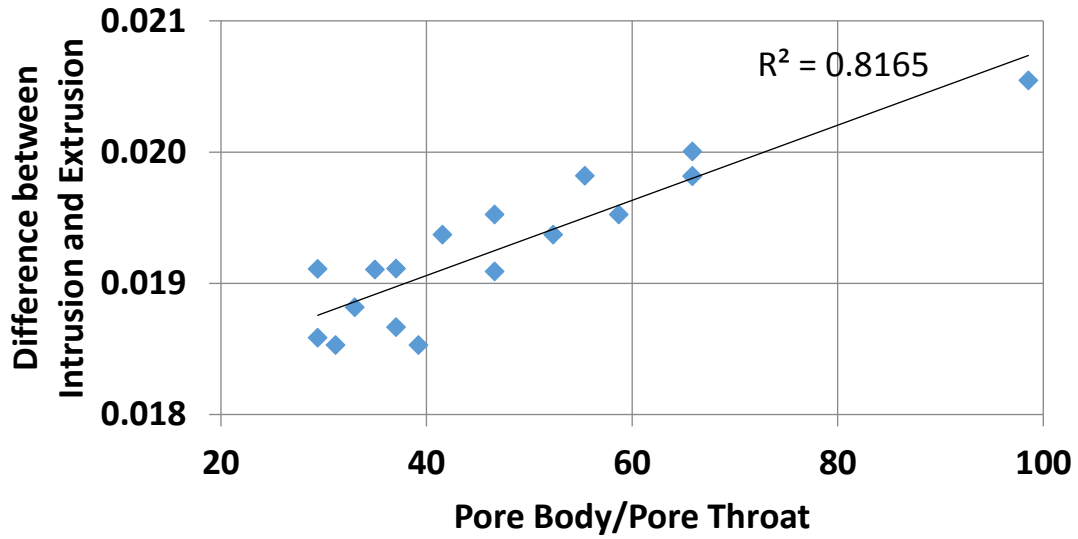

Figure 4.17: Difference between mercury intrusion and extrusion versus pore body to throat ratio shows a directly proportional relationship.

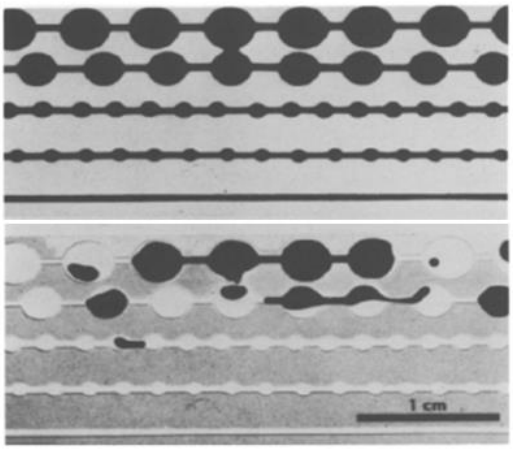

Figure 4.18: Glass model with mercury. Lower part shows the residual trapped mercury (Wardlaw and McKellar, 1981)

4.1.5 Imaging Data versus NMR Data

Nuclear magnetic resonance (NMR) was performed on the native-state samples. Pore volume distribution is plotted with the increasing T_2 relaxation time. While it is fairly easy to combine SEM data with MICP data, comparing SEM data with NMR data requires T_2 – pore radius conversion. Assuming all pores from SEM data are spherical, equivalent pore radius R (μm) is related to T_2 relaxation time as:

$$T_2 = \frac{1000 * R}{3 * \rho_e}$$

where ρ_e (μm/sec) is the effective surface relaxation and is treated as matching factor. **Fig 4.19 – Fig 4.22** show the comparison between pore distributions from NMR data and converted SEM data for sample #1, #2, #3, and #4. NMR and SEM data show a strong agreement; the peaks almost overlay each other for all samples. This strong

correlation indicates that NMR and SEM data represent the pore body distribution. The average ρ_e is 41 µm/sec ± 3 µm/sec. Compared to ρ_e values for NMR/MICP matching from Sulucarnain's study (2012), ρ_e values for NMR/SEM matching is larger. The average ρ_e for matching between NMR spectra and MICP data from Ordovician organic rich shale samples is 1.7 µm/sec ± 1.0 µm/sec (Sulucarnain et al., 2012). Since NMR and SEM presents the pore body distribution while MICP presents pore throat distribution, ρ_e values for NMR/SEM matching is more reasonable.

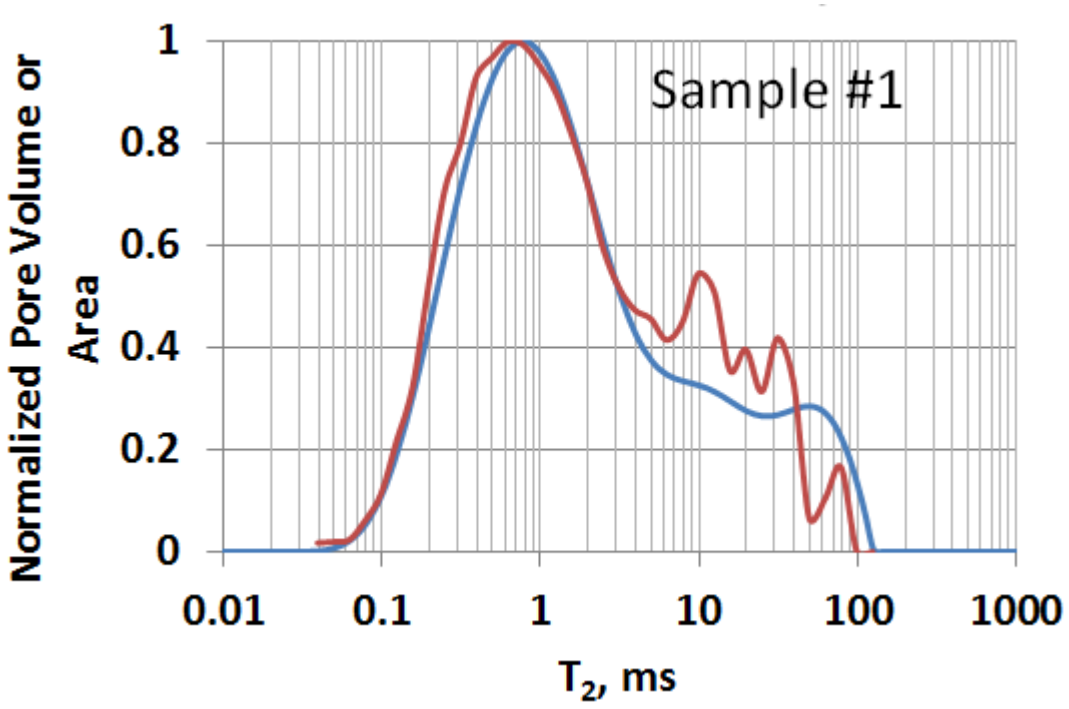

Figure 4.19: Comparison of NMR pore volume distribution (blue) and converted SEM pore area (red) distribution of sample #1. The effective surface relaxation is ρ_e = 33 µm/sec.

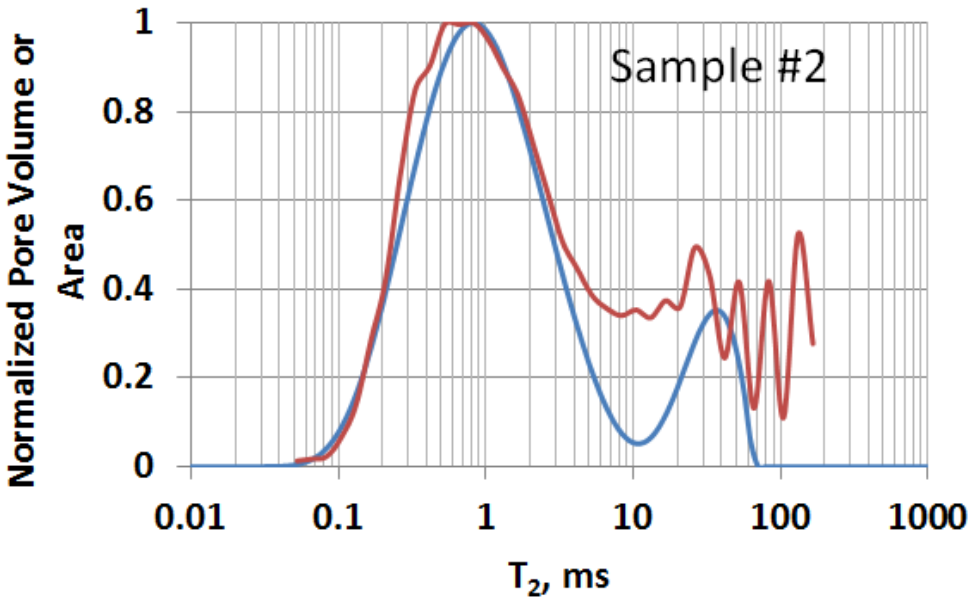

Figure 4.20: Comparison of NMR pore volume distribution (blue) and converted SEM pore area distribution (red) of sample #2. The effective surface relaxation is ρ_e = 40 µm/sec.

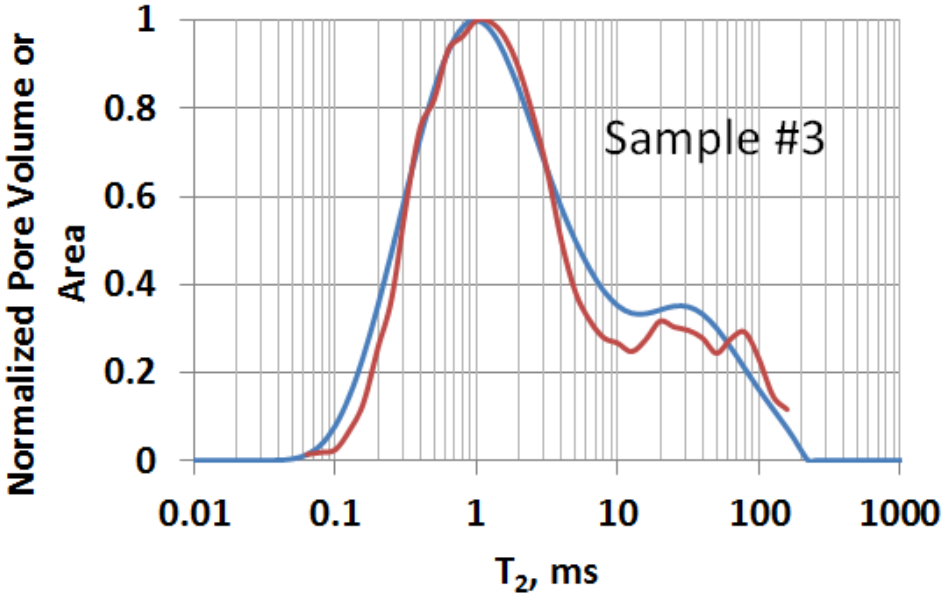

Figure 4.21: Comparison of NMR pore volume distribution (blue) and converted SEM pore area distribution (red) of sample #3. The effective surface relaxation is ρ_e = 46 µm/sec.

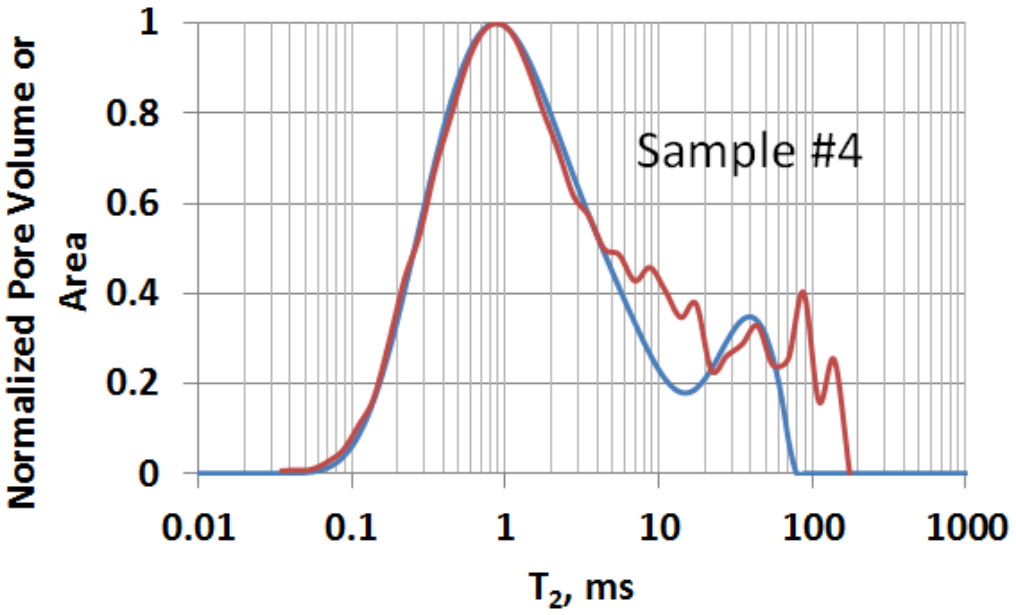

Figure 4.22: Comparison of NMR pore volume distribution (blue) and converted SEM pore area distribution (red) of sample #4. The effective surface relaxation is ρ_e = 46 µm/sec.

4.2 Mineral Grain Size Distribution

4.2.1 Representative Elementary Area

Seven samples from the 1ft Wolfcamp core are selected for the grain size study. Four major mineral groups are successively segmented by thresholding and applying the watershed method. Similar method applied for porosity and organic matter to determine REA values for mineral groups. From one standard map (276 µm x 6,000 µm), smaller sub-maps of different sizes and random locations were extracted. For each of the mineral group, SEM areal percentage of these sub-maps were calculated and plotted in comparison with the areal percentage value of the original map. **Fig 4.23** shows an example result for group SCl (silica, clays, Mg-dol., feldspar) from sample #1. The

original map area of this sample is 1.45 mm^2. Large fluctuation of areal percentage is observed for small sub-maps. As the size of the sub-map increases, the areal percentage values converge to the areal percentage value of the whole map for mineral group SCl of sample #1. This follows a similar trend to those observed porosity and organic matter. Truncation error of the areal percentage values of each sub-map is compared to the value of the whole map in **Fig 4.23B**. A cut-off of 10% truncation error is acceptable, i.e. 11% of the whole map area. At the 11% full map scale, the area needed is 0.16 mm^2 or larger)

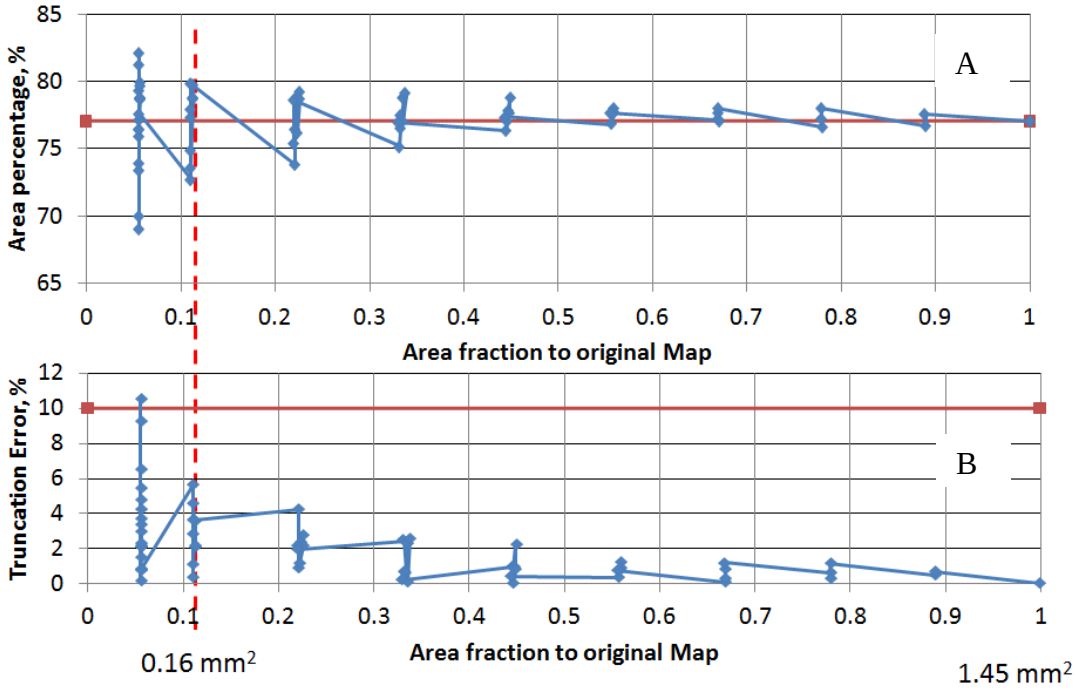

Figure 4.23: A) areal percentage for mineral group SCl (silica, clays, Mg-dolomite, feldspar) measured from SEM map (sample #1) for different sub-map areas are compared to total porosity for the original map (red line), B) Truncation errors of each areal percentage value is compared to 10% error (red line). Note beyond a map area of roughly 11% of the whole map, the difference in areal percentage estimates reduces and become acceptable.

Excluding image processing time, the required amount of time to acquire this cut-off map is 8 hours, which is much less than the required time for the whole map of approximately 66 hours. **Fig 4.24 – Fig 4.26** shows example results for group CCl (calcite, clays, Fe-dol., K-feldspar), RA (rutile, apatite), and P (pyrite) from the same sample. The REA values for the four mineral groups from this sample are 0.16, 1.13, 0.97, and 0.97 mm^2, respectively.

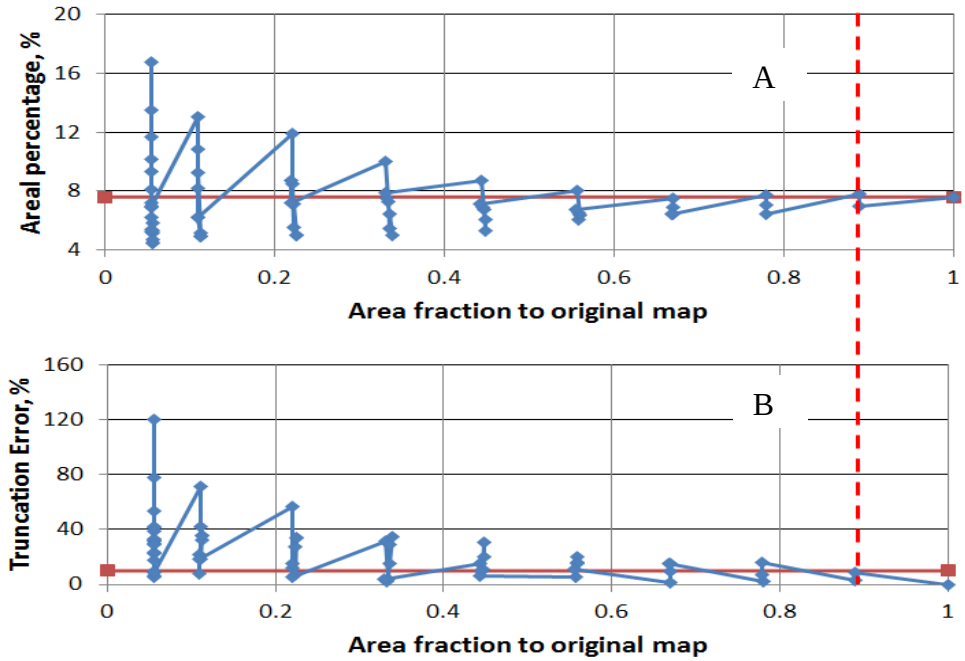

Figure 4.24: A) areal percentage for group CCl (calcite, Fe-Dolomite, clays, K-feldspar) measured from SEM map (sample #1) for different sub-map areas in compared to total porosity for the original map (red line), B) Truncation errors of each areal percentage value is compared to 10% error (red line). Note beyond a map area of roughly 90% of the whole map, the difference in areal percentage estimates reduces and become acceptable.

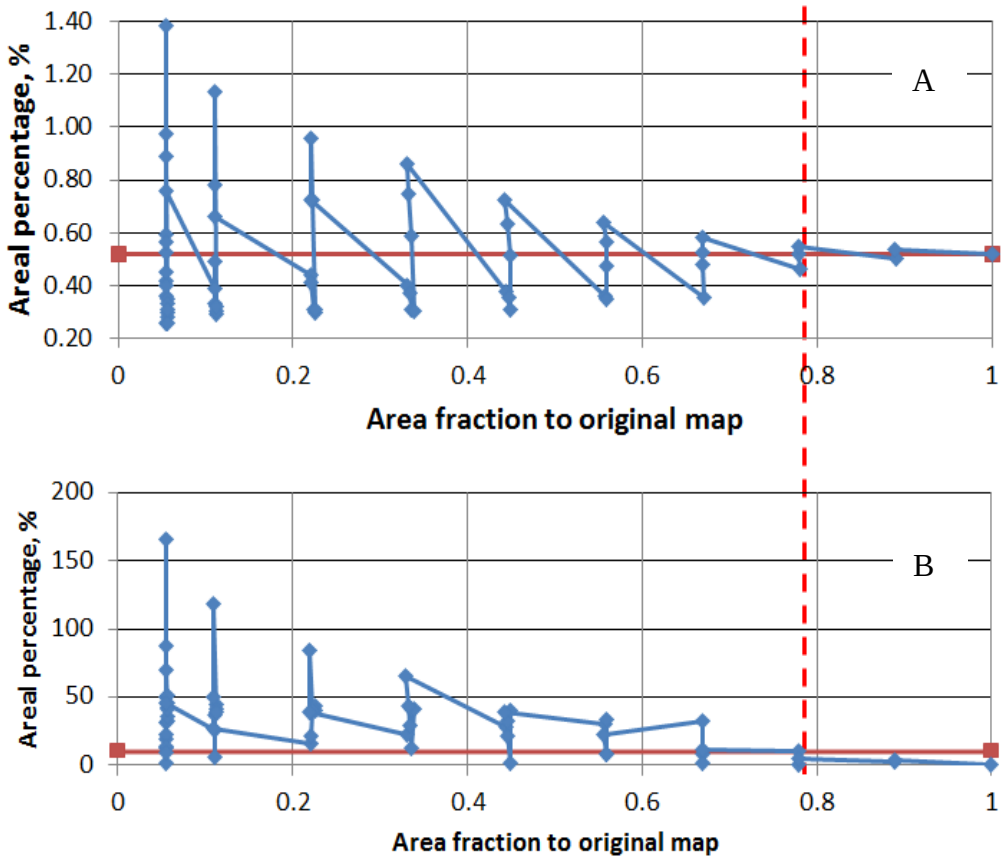

Figure 4.25: A) areal percentage for group RA (rutile and apatite) measured from SEM map (sample #1) for different sub-map areas is compared with total porosity for the original map (red line), B) Truncation errors of each areal percentage value is compared to 10% error (red line). Note beyond a map area of roughly 78% of the whole map, the difference in areal percentage estimates reduces and become acceptable

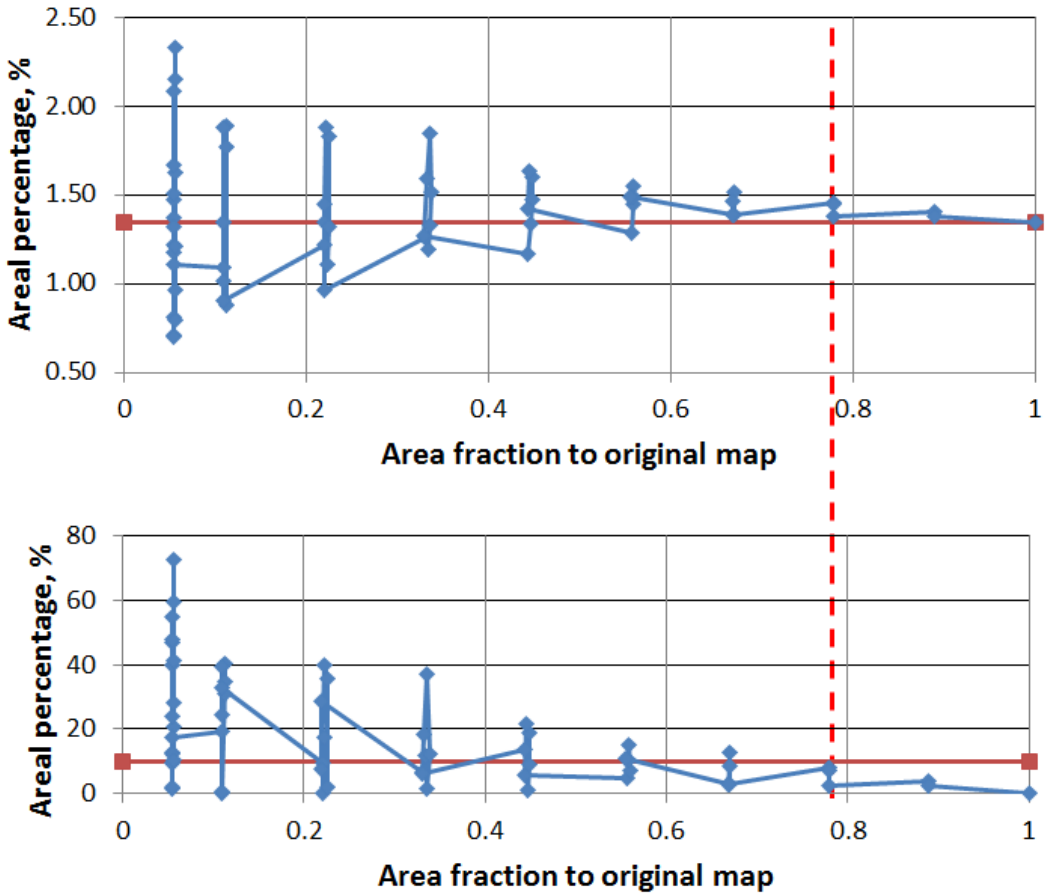

Figure 4.26: A) areal percentage for group P (pyrite) measured from SEM map (sample #1) for different sub-map areas is compared to total porosity for the original map (red line), B) Truncation errors of each areal percentage value is compared to 10% error (red line). Note beyond a map area of roughly 78% of the whole map, the difference in areal percentage estimates reduces and become acceptable.

The REA values for the four mineral groups for the seven Wolfcamp Shale samples are showed in **Fig 4.27** in comparison with the REA values for porosity calculated in **Chapter 4.1.1**. A fairly similar trend is observed from the results for the selected

samples. mineral group SCl (silica, clays, Mg-dolomite, feldspar) has significant low REA (0.08 to 0.16 mm^2), much lower compared to the REA values for the other three mineral groups including group CCl (calcite, clays, Fe-dolomite, K-feldspar), group RA (rutile and apatite), and group P (pyrite). These small REA values are due to the dominance of quartz which contributes 78% of the total area in average for the seven samples in the mineralogy (**Table 4.1**); the more common a mineral is in the microstructure, the smaller area required to capture its representative. Mineral group CCl has fairly high REA (0.05 to 0.12 mm^2) due to its lower areal percentage (6.2% in average). Mineral group RA and Group P have the highest REA (0.97 to 1.30 mm^2 and 0.65 to 1.30 mm^2, respectively); the REA required is almost equal to the area of the whole map (approximately 1.56 mm^2). The large REA values for rutile, apatite, and pyrite are due to low concentration; this can be clearly observed from the SEM image and map (**Fig 3.4**). In fact, mineral group RA and P only contribute to 0.3% and 1.1% in average to the total 2D microstructural area, respectively. When comparing the REA values of the four mineral groups with those of the porosity (see **Fig 4.27**), we note that the representative area required for porosity is smaller than most of the mineral group except for group SCl. It is noticed from **Table 4.1** that similar behavior is observed for areal percentage: on average, the porosity values measured from the whole maps for the seven samples are smaller than the areal percentage of group SCl, but greater than the areal percentage of the other three groups.

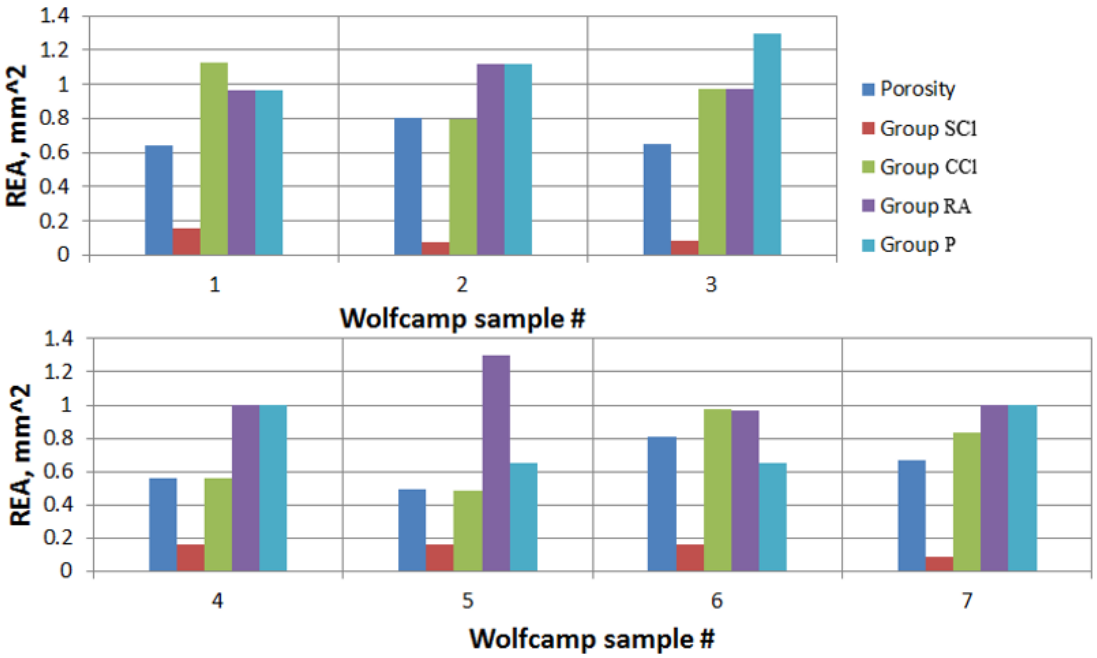

Figure 4.27: REA values for porosity and four mineral groups for the selected seven samples. Note that REAs for group SCl are significantly low compared to the others

Table 4.1 – Average areal percentage and REA values for four mineral groups of the selected seven samples

Wolfcamp	Group SCl (silica, clays, Mg-dolomite, feldspar)	Group CCl (calcite, clays, Fe-dolomite, K-feldspar)	Group RA (rutile, apatite)	Group P (pyrite)
Areal percentage, %	78 ± 2	6.2 ± 1	0.3 ± 0.2	1.1 ± 0.3
REA, mm^2	0.08 – 0.16	0.8 - 1.13	0.97 – 1.2	0.96 – 1.30

4.2.2 Grain Size Distribution

Fig 4.28 shows size distribution result for all of the mineral grains observed from the maps of the seven Wolfcamp samples. The distributions were determined from the entire map acquired for each sample (similar to pore and organic size distribution). There is an inversely proportional relationship between number of mineral grains and

equivalent spherical mineral grain radius on a log-log scale. The grain size distributions for the seven samples show a high degree of consistency as the plots follow a similar trend; an insignificant variation is observed. Similar to pore and organic size distribution, grain size distribution indicates that small particles dominate in number. The average grain equivalent radius for seven samples within the 1 ft section ranges from 288 nm to 321 nm. The average grain radius for all seven samples is 307 nm ± 12 nm. On average, approximately 200 to 325 grains can be sampled with a nanoindentor probe.

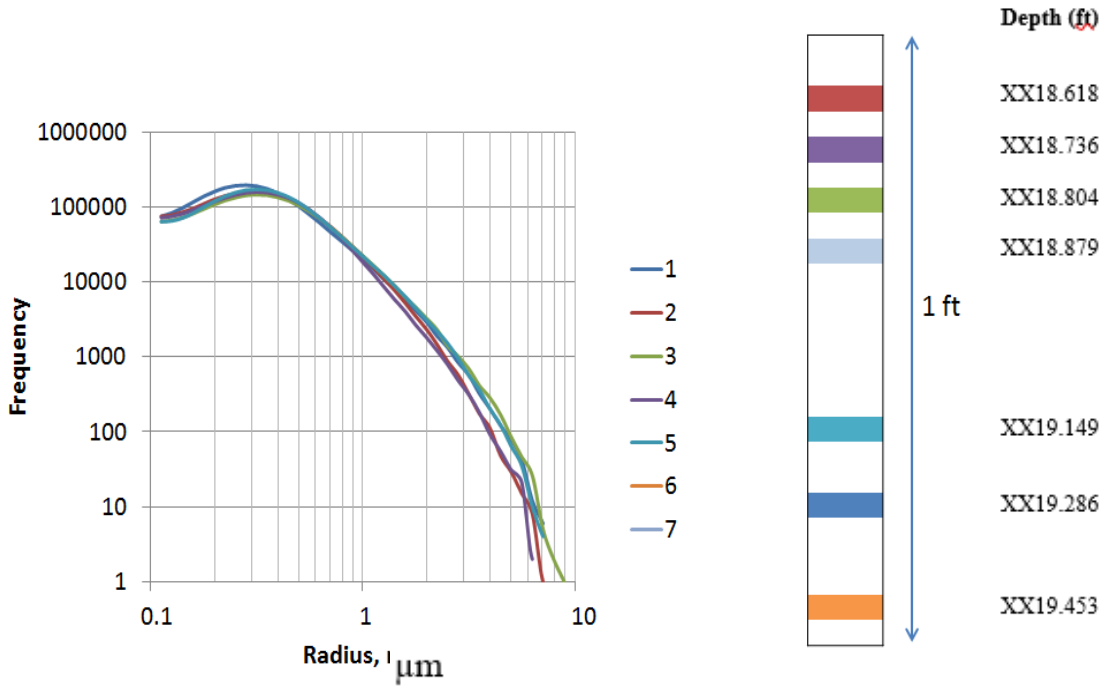

Figure 4.28: All Grain size distribution for seven samples with their location on the right picture. Note the similar trend for these seven samples. Distributions were derived from entire SEM maps (1.6 mm^2)

However, mineral grain includes four smaller groups whose amounts and behaviors are remarkably different from each other. Thus, it is necessary to break down the grain

distribution more finely. **Fig 4.29 – Fig 4.32** show the grain size distribution for each of the four mineral groups acquired from the entire maps. Similar results are observed for all groups as the number of grains appears to inversely proportional to equivalent spherical grain radius and small grain particles dominate in number. Comparing to the distributions for all grains, the distributions for the four mineral groups show larger variation between the samples, especially for mineral group RA (rutile, apatite) and group P (pyrite). This is due to the small number of rutile and apatite grains in group RA and pyrite grains in group P observed from the maps. These variations for these groups are however relatively small; overall it can be stated that the grain size distributions are fairly consistent even after breaking down by mineral groups. Combining this result with the FTIR from **Fig 3.8**, It can be concluded that there is no significant difference in mineralogy throughout the selected one-foot section of Wolfcamp shale. Therefore, only one sample is required at any location from this one-foot section for a successfully grain size distribution study.

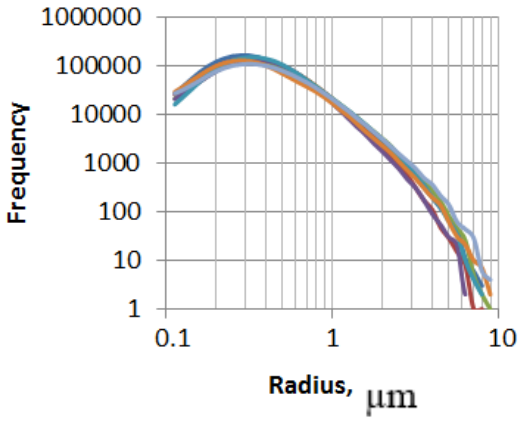

Figure 4.29: Grain size distribution for group SCl (silica, clays, Mg-dol., feldspar) of seven samples. Note the similar trend for these samples. A little bit more variation is observed compared to all grain distribution (see Fig 4.28).

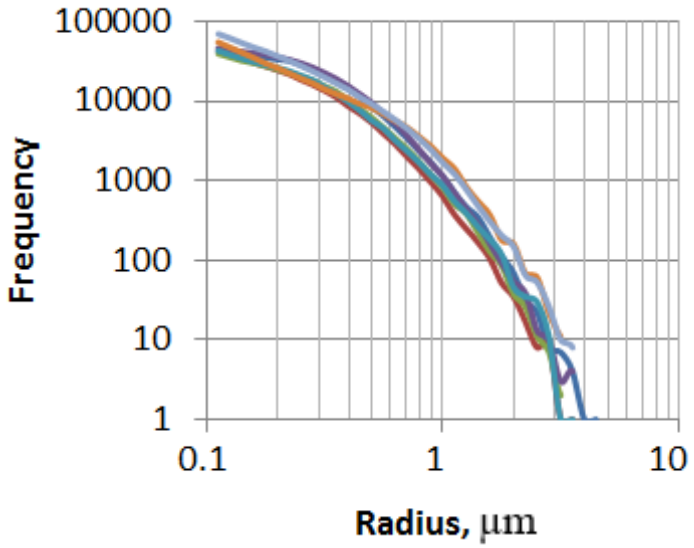

Figure 4.30: Grain size distribution for group CCl (calcite, clays, Fe-dol., K-feldspar) of seven samples. Note the similar trend for these samples. A little bit more variation is observed compared to all grain distribution.

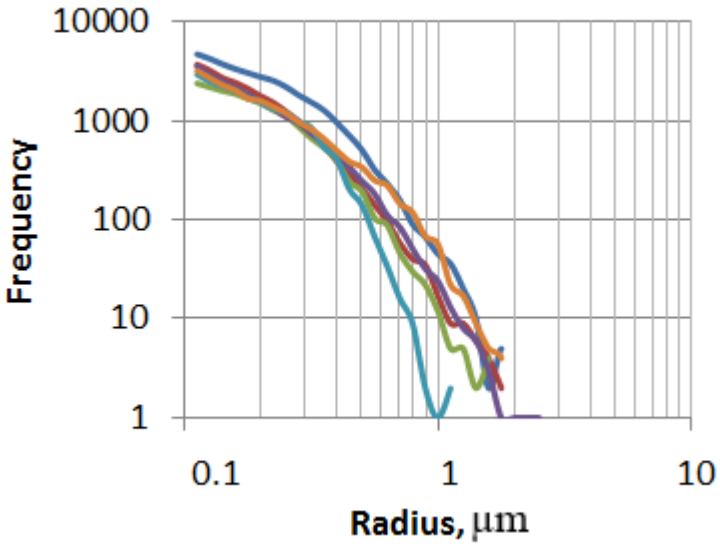

Figure 4.31: Grain size distributions for group RA (rutile, apatite) of seven samples. Note the similar trend for these samples. More variation is observed compared to all grain distribution.

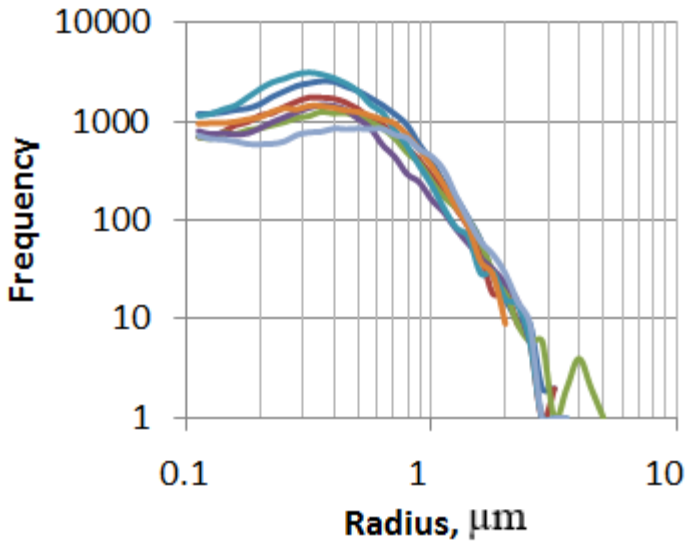

Figure 4.32: Grain size distribution for group P (pyrite) of seven samples. Note the similar trend for these samples. More variation is observed compared to all grain distribution.

The grain size distribution for clay is effectively separated from group SCl (silica, clays, Mg-dol., feldspar) and CCl (calcite, clays, Fe-dol., K-feldspar) based on aspect ratio. An example for group CCl from sample #1 (**Fig 4.33**) shows the distribution results for clay grains (mostly chlorite) and for the combination of other grains (calcite, iron-rich dolomite, and feldspar) in this group. It is noticed that the number of grains proportionally decreases with the increasing grain size. For group CCl in all seven samples, the average grain radius of clay (200 nm ± 2nm) is smaller than the average grain radius of other grains (227 nm ± 2 nm); this difference is however insignificant. A similar result is observed for group SCl as the average radius for clay and other grains are 243 nm ± 2 nm and 319 nm ± 2 nm, respectively.

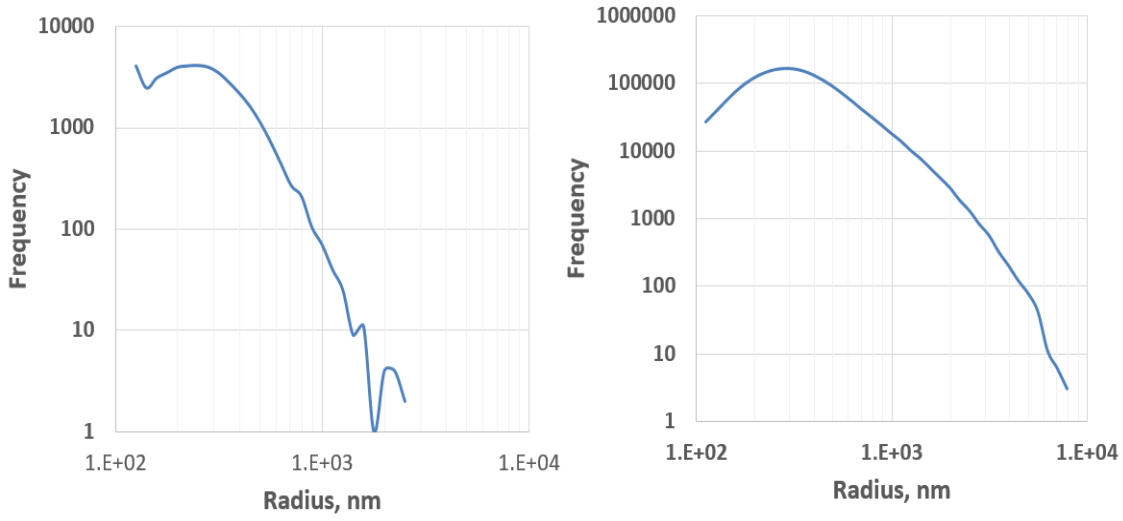

Clay Other Grains

Figure 4.33: Grain size distribution for clay grains (left) and other grains (right) from group CCl of seven samples. Average radius of clay is less than of other grains.

Similar to pore and organic matter, grain size distributions for each sample are studied at different scales. Three sub-maps of 30% scale (273 μm x 1,713 μm) which totally cover 90% area of the whole map of sample #1 are random selected. **Fig 4.34** shows the grain size distribution of mineral group SCl (silica, clays, Mg-dol., feldspar) for the three sub-maps. As with the previous grain size distribution (**Fig 4.28**), the same trend is observed in that number of grains is inversely proportional to equivalent spherical grain radius on the log-log scale. There is a nice consistency that those three plots almost overlay each other and contain an almost similar total number of mineral grains. The grain size distribution thus is very consistent at this sub-map scale. Breaking down into smaller scale, grain size distribution plots of six sub-maps of 20% scale (273 μm x

1,429 μm) which totally cover 80% area of the whole map of the same sample at random locations are shown in **Fig 4.35**. A similar trend is observed for these plots. Compared to 30% scale, these lots show a little bit more variation, however the percentage deviation is still relatively small. **Fig 4.36** and **Fig 4.37** show the same interpretation for smaller scales including 10% scale (273 μm x 571 μm) which is approximately equivalent to REA scale for this group of this map and 5% scale (273 μm x 286 μm). Although greater variations of the plots are observed as the scale gets smaller, the difference is always less than 5%. Therefore, to study grain size distribution, only a small area of imaging is required. As for this 1 ft core section, the area needed for grain size distribution would be two times smaller than the area required to capture the representative mineralogy.

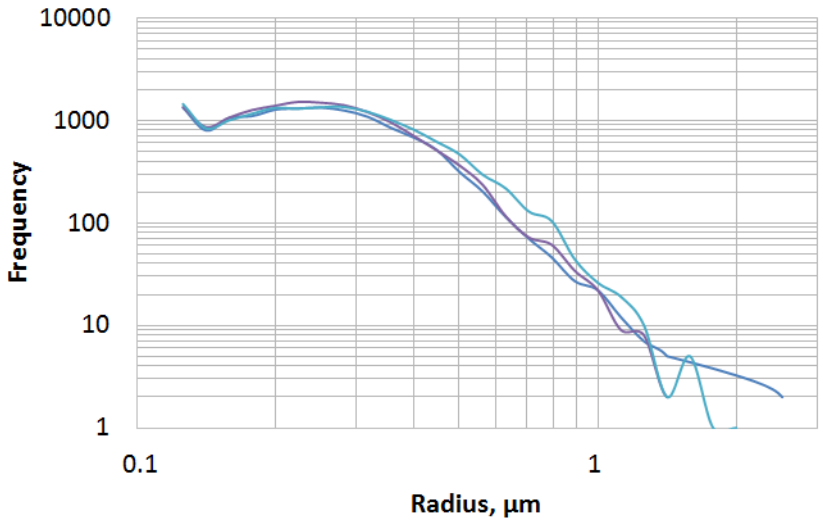

Figure 4.34: All grain size distribution of three sub-maps of 30% scale for group SCl (silica, clays, Mg-dol., feldspar) of sample #1. Note the similar trend of these sub-maps. Note we assume spherical grains

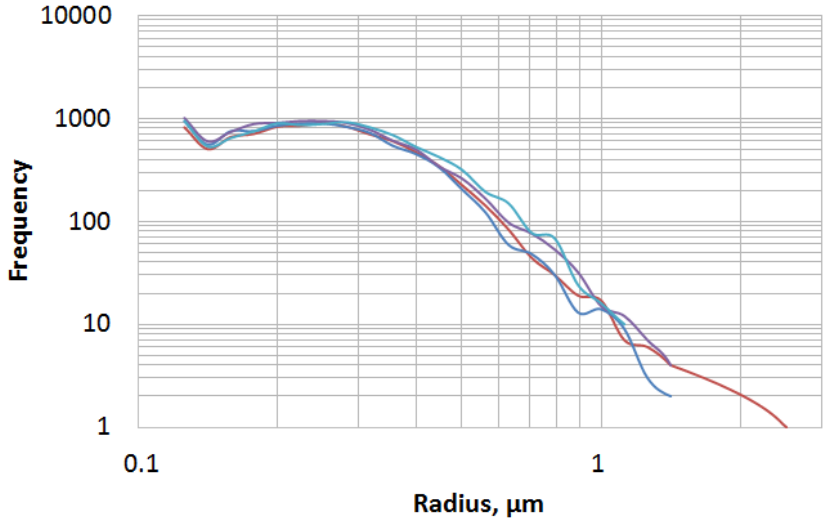

Figure 4.35: All grain size distribution of four sub-maps of 20% scale for group SCl (silica, clays, Mg-dol., feldspar) of sample #1. Note the similar trend of these sub-maps. Note we assume spherical grains

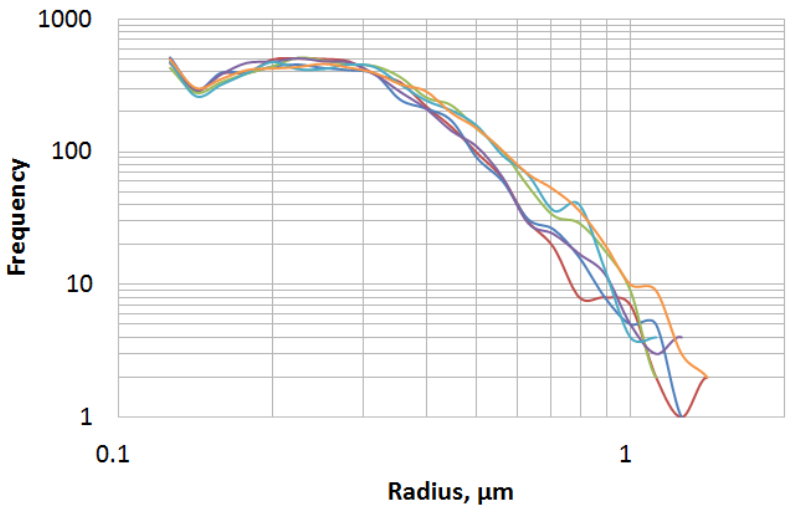

Figure 4.36: All grain size distribution of six sub-maps of 10% scale for group SCl (silica, clays, Mg-dol., feldspar) of sample #1. Note the increase in variation between the plots especially at large size. Note we assume spherical grains

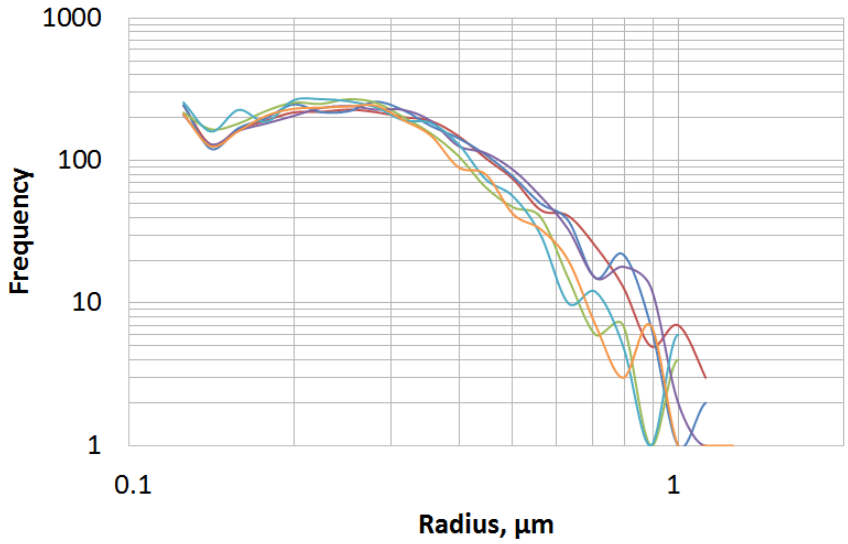

Figure 4.37: All grain size distribution of six sub-maps of 5% scale for group SCl (silica, clays, Mg-dol., feldspar) of sample #1. Note the increase in variation between the plots especially at large size. Note we assume spherical grains

4.2.3 Clay Grains Alignment

Earlier study on New Albany Shale and Chattanooga Shale using X ray diffraction techniques suggests that anisotropy at elevated pressure is caused mainly by preferred orientation of clays parallel to bedding plane (Johnston and Christensen, 1995). Therefore, the clay orientation acquired using SEM imaging technique might be useful to evaluate the anisotropy. **Fig 4.38** shows the orientation plot for the clay particles separated from other mineral grains in group CCl (calcite, clays, Fe-dol., K-feldspar) of sample #1. On average, clays are 16^0 to the bedding plane. More than 60% of the elongated particles lie between 0^0 and 10^0 to the bedding plane. Most of the clay particles are oriented at larger angle (from 10^0 to 60^0); there are very few particles at high angle to the bedding plane (70^0 or more). Most of the clays are thus observed to be sub-parallel to the bedding plane. According to the study of Johnston and Christensen (1995), these samples can be concluded to be strongly anisotropic. The anisotropy of the samples (%) is defined as (Johnston and Christensen, 1995):

$$\frac{V_{max} - V_{min}}{V_{max}}$$

The velocity measurements were conducted on samples within a 195 ft interval in the same well with the 1 ft section. The results show that those samples are highly anisotropy, approximately 24 ± 3% for V_p and 26 ± 5 % for V_s at 5,000 psia. This strongly agree with the conclusion made from clay alignment study.

Fig 4.39 shows orientation to the bedding plane for the clay particles separated from group CCl (calcite, clays, Fe-dol., K-feldspar) of sample #1 at 100%, 30%, 10%, and 5% scale. Similar to the entire map (100% scale), sub-maps with smaller scales present the same trend that majority of the clay particles are oriented at small angle between 0

and 10^0; most of the clay grains are parallel to the bedding plane. However, the trend for clay alignment becomes clearer as the imaging sample size increases. At 5% scale (273 µm x 286 µm), the low angle peak flattens out and is more difficult to recognize than the peak for the entire map. This suggests that a relatively large area needs to be acquired for the anisotropy study.

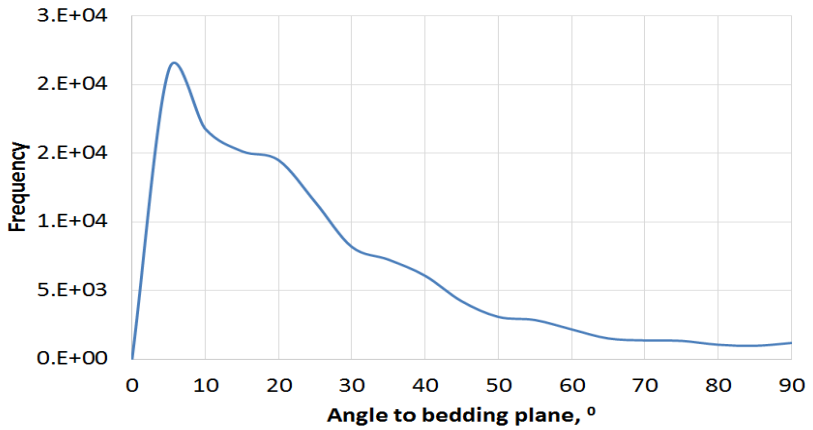

Figure 4.38: Clay particle orientation relative to the bedding plane (group CCl (calcite, clays, Fe-dol., K-feldspar) – sample #1). Majority of clays are oriented at 0^0 to 10^0

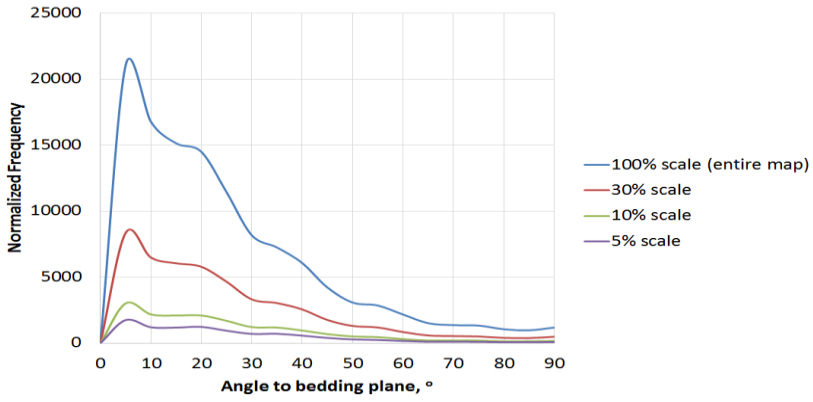

Figure 4.39: Clay particle orientation to the bedding plane at different scale (group CCl (calcite, clays, Fe-dol., K-feldspar) – sample #1). Note the trend gets better as the scale increases

Chapter 5: Conclusion

5.1 Significance and Contribution

Within the 1 ft interval of Wolfcamp shale, large variations of REA to measure porosity, organic matter, and grain size indicate a high degree of microstructural and mineralogical heterogeneity. Thus, to successfully characterize this interval, representative sample size needs to be studied for each depth interval. At high resolution (10 nm), the reported REA values are large; especially for organic matter and mineral Group RA (rutile and apatite), and Group P (pyrite) REAs are almost as large as the area of the original map (1.56 mm^2). **This makes the idea of extracting petrophysical information from either a large SEM image with low resolution or a small SEM image with high resolution statistically unrepresentative.**

Excluding the factor of viewing angle, clays are proved in SEM images to have slit-like shape. By selecting appropriate aspect ratio cut-off, majority clays can be effectively separated from other grains in a mineral group of nearly similar density. This improves grain size distribution and grain alignment study.

Strong agreement between derived SEM and NMR pore size data indicates that both represent the pore body distribution. Compared to previous works that match MICP with NMR pore size data (Sulucarnain et al., 2012; Ghomeshi et al., 2013; Fiorelli et al., 2015 etc.), effective surface relaxation ρ_e for SEM – NMR matching is larger (41 ± 3 μm/sec). This ρ_e is more reasonable compare to ρ_e values for MICP – NMR matching.

Besides REA and pore size distribution, FEI SEM mapping technique allows the determination of grain size in shale. For seven sample distributed in the 1 ft Woflcamp core section, average grain size ranges from 288 nm to 321 nm. The average grain size for the whole section is 307 ± 12 nm; this indicates that grain size is consistent throughout this interval.

5.2 Conclusion

The main conclusions of this study are summarized below:

- Representative Elementary Areas (REA) are determined over a 1 ft Wolfcamp core to be 0.8 mm^2 for porosity and 1.2 mm^2 for organic matter.

- Pore and organic size distribution were derived from MAPS SEM images. Pore size distributions are consistent for samples taken throughout the 1ft section. Thus, only one MAP sample is required to characterize the pore size distribution in this interval. For each depth interval, pore size distribution is consistent at different scales. REA needed to capture pore size distribution is smaller than REA to measure porosity.

- There is good correlation between porosity estimations from imaging data and crushed helium porosity measurement (1.0% difference). There is good

agreement between organic measurements from imaging data and LECO™ TOC data (0.6% difference).

- NMR data and SEM pore size distributions are very similar. Average effective surface relaxation ρ_e values derived from matching SEM and NMR pore size distribution is 41 ± 3 μm/sec. Compared to ρ_e values from matching MICP and NMR distribution, this value is recommended as both SEM and NMR represent pore body distribution while MICP data represents pore throat distribution.

- We derive grain size distribution from SEM images of shale. Mineral grains can be segmented into four groups based on gray scale which reflects atomic number. Group SCl includes silica, clay (kaolinite and illite), magnesium dolomite, and feldspar. Group CCl includes calcite, clay (chlorite), iron rich dolomite, and potassium feldspar. Group RA includes rutile and apatite. Group P includes pyrite. Watershed segmentation allows mixing grains from the same group to be separated and thus improves grain size distribution calculation. REAs for different mineral groups are determined using a workflow similar to those used for porosity and organic matter REA determinations. Mineral REAs are 0.16 mm^2 for group SCl, 1.13 mm^2 for group CCl, 1.20 mm^2 for group RA, and 1.30 mm^2 for group P.

- Clays are oriented mostly parallel to the bedding plane (16^0 to the bedding plane on average), suggesting anisotropy should be strong in these samples.

5.3 Limitation of the Study

The results and conclusions from the study are constrained by following limitations and assumptions :

- The study is conducted over a limited 1 ft interval of Wolfcamp shale. All of the results are legitimate only for this interval of investigation. Different results are predicted when working on extended Wolfcamp sections or different formations.

- Size distribution analysis is under assumption that all pore, organic matter, or grain particles are spherical. The radius of a particle for this study is the equivalent radius of a sphere which has same area.

- The imaging surface in the study is parallel to bedding plane. Different results may be expected at the surface perpendicular to bedding plane.

- NMR measurements were conducted on native state samples; a significant amount of free water in these samplesis missing as can be observed from the NMR spectra. Experiments on saturated samples would yield a better result.

- 8-bit SEM images result in limited intensity histogram. The gray values only range from 0 to 255. Thus it is challenging to diffrentiate a particular mineral from the others. It is worth considering using 16-bit images for FEI SEM Mapping; this will give a much better intensity histogram where the gray values range from 0 to 65,535.

- Watershed is observed to not perform very well on mineral Group SCl (silica, clay, magnesium dolomite, and potassium feldspar), where most grains mix together.

5.4 Acknowledgements

I would like to thank:

- FEI and Thermo Fisher Scientific for providing me with the graduate fellowship as well as laboratory equipment to conduct the study.
- Pioneer Natural Resources for their donation of the Wolfcamp shale samples used in this study
- Unconventional Gas Shale Consortium for their continued support and feedback

References

Bakhtiary, E., and Arson, C. 2013. Towards a Thermodynamic Framework to Model Particle Crushing and Sieving. Paper ARMA 13-348 presented at the 47th US Rock Mechanics/ Geomechanics Symposium, San Francisco, CA, 23-26 June.

Ballard, T., and Beare, S. 2013. Particle Size Analysis for Sand Control Applications. Paper SPE 165119 presented at the SPE European Formation Damage Conference and Exhibition, Noordwijk, the Netherlands, 5-7 June.

Bachmann, J., Stuart, P., Corales, B., Fernandez, B., Kissel, P., Stewart, H., Amoss, D., Angelico, B., Garcia, A.G., Handcock, K.B., Roberts, R., Sanchez, B. 2014. The "New" Horizontal Permian Basin. Howard Weil, 27 January.

Bocangel, W. 2013. Acoustic and Topological Characterization of Organic Matter in Shales. Master's Thesis. University of Oklahoma, Norman.

Bocangel, W., Sondergeld, C.H., and Rai, C.S., 2013. Acoustic Mapping and Characterization of Organic Matter in Shales. Paper SPE 166331 to be presented at the SPE Annual Technical Conference and Exhibition, New Orleans, LA, September 30-October 2.

Bishop, D. L. 1934. A Sedimentation Method for the Determination of the Particle Size of Finely Divided Materials (such as Hydrated Lime). Part of Bureau of Standards Journal of Research, Vol. 12.

Curtis, M.E., Ambrose, R.J., Sondergeld, C.H., and Rai C.S., 2010. Structural Characterization of Gas Shales on the Mirco- and Nano- Scales. Paper SPE 137693 to be presented at the Canadian Unconventional Resources & International Petroleum Conference, Calgary, Alberta, Canada, 19-21 October.

Curtis, M.E., Goergen, E.T., Jernigen J.D., Sondergeld, C.H., and Rai, C.S., 2014. High-Resolution Mapping of the Distribution and Connectivity of Organic Matter in Shales. Paper SPE 170787 to be presented at the SPE Annual Technical Conference and Exhibition, Amsterdam, The Netherlands, 27-29 October.

Dow, W.G., 1977. Kerogen Studies and Geological Interpretations. *Journal of Geochemical Exploration.* **7**, pp. 79-99.

Dunn, K.J., Bergman, D. J., and Latorraca, G. A. 2002. Nuclear Magnetic Resonance: Petrophysical and Logging Applications, Pegamon Press, New York, pp. 293.

EIA. 2016. Trends in U.S. Oil and Natural Gas Upstream Costs. https://www.eia.gov/analysis/studies/drilling/pdf/upstream.pdf. March 2016

EIA. 2016. Future U.S. Tight Oil and Shale Gas Production Depends on Resources, Technology, Markets. https://www.eia.gov/todayinenergy/detail.php?id=27612. 22 August

Fiorelli, G.L., Winter, A., Koroishi, E.T., and Trevisan, O.V. 2015. Characterization of Coquinas and Dolomites Integrating Electrical Resistivity, Nuclear Magnetic Resonance (NMR), and Porosimetry by Mercury Intrusion (MICP). Paper SPE 175657 to be presented at the SPE Reservoir Characterization and Simulation Conference and Exhibition, Abu Dhabi, UAE, 14-16 September.

Giffin, S., Littke, R., Klaver, J., and Urai, J.L., 2013. Application of BIB-SEM technology to characterize macropore morphology in coal. *Internal Journal of Coal Geology*. pp. 11

Gladkikh, M., Chen, J., and Chen, S. 2008. Method of Determining Formation Grain Size Distribution from Acoustic Velocities and NMR Relaxation Time Spectrum. Paper presented at the SPWLA 49th Annual Logging Symposium, Edinburg, Scotland, 25-28 May.

Goergen, E.T., Curtis, M.E., Jernigen, J.D., Sondergeld, C.H., and Rai, C.S., 2014. Integrated Petrophysical Properties and Multi-Scaled SEM Microstructural Characterization. Paper URTeC 1922739 to be presented at the Unconventional Resources Technology Conference, Denver, Colorado, USA, 25-27 August.

Goral, J., Miskovic, I., Gelb, J., and Andrew, M. 2015. Correlative XRM and FIB-SEM for (Non)Organic Pore Network Modeling in Woodford Shale Rock Matrix. Paper presented at the International Petroleum Technology Conference, Doha, Qatar, 6-9 December.

Hafner, B. 2007. Scanning Electron Microscopy Primer. University of Minnesota, Characterization Facility.

Howard, J.J. 1994. Wettability and Fluid Saturations Determined from NMR T1 Distributions. Mgn. Reson. Imaging **12** (2), pp. 197-200

Johnston, J.E. and Christensen, N.I. 1995. Seismic Anisotropy of Shales. Journal of Geophysical Research, **100,** pp. 5991-6003.

Kelly, L., Bachmann, J., Amoss, D., Angelico, B., Corales, B., Fernandez, B., Kissel, P., Roberts, R., and Stewart, H. 2012. Permian Basin: Easy to Oversimplify, Hard to Overlook. Exploration & Production Journal, Howard Weil, 19 January.

Kleinberg, R. L., Straley, C., Kenyon W.E., Akkurt, R., and Fraooqui, S. A. 1993. Nuclear Magnetic Resonance of Rocks: T1 vs. T2. Paper SPE 26470 presented at the SPE Annual Technical Conference and Exhibition, Houston, Texas, 3-6 October.

Ko, L.T., Loucks, R.G., Ruppel, S.C., Zhang, T., and Peng, S. 2017. Origin and characterization of Eagle Ford pore networks in the south Texas Upper Cretaceous shelf, AAPG Bull., 101, 3, 387-418.

Loucks, R.G., Reed, R.M., Ruppel, S.C., and Jarvie, D.M.., 2009. Morphology, Genesis and Distribution of Nanometer-Scaled Pores in Siliceous Mudstones of the Mississippian Barnett Shale. Journal of Sedimentary Research. 79, pp. 848-861.

Odusina, E. O. 2011. An NMR Study of Shale Wettability. Master's Thesis, University of Oklahoma, Norman.

Pommer, M., and Milliken, K., 2015 Pore Types and Pore-Size Distributions across Thermal Maturity, Eagle Ford Formation, Southern Texas. AAPG Bulletin, v. 99, no. 9, pp. 1713-1744.

Prasad, M.., 2002. Mapping Impedance Microstructures in Rocks with Acoustic Microscopy. *The Landing Edge*, **20(**2): 172-179.

Prasad. M., Mukerji, T., Reinstaedler, M., and Arnold, W.,2009. Acoustic Signatures, Impedance Microstructure, Textural Scales, and Anisotropy of Kerogen-Rich Shale. Paper SPE 124840 presented at the SPE Annual Technical Conference and Exhibition, New Orleans, LA, 4-7 October.

Shellenberger, M., Nordhaus, T., Trembath, A., and Jenkins, J. 2012. Where the Shale Gas Revolution Came from – Government's Role in the Development of Hydraulic Fracture in Shale. Breakthrough Institute Energy & Climate Program. May 2012.

Sulucarnain, I.D., Sondergeld, C.H., and Rai, C. S. 2012. An NMR Study of Shale Wettability and Effective Surface Relaxivity. Paper SPE 162236 to be presented at the SPE Canadian Unconventional Resources Conference, Calgary, Alberta, Canada, 30 October – 1 Novemvber.

Suri, Y. 2011. Predicting Petro-physical Properties using SEM Image. Paper SPE 144434 to be presented at the SPE Reservoir Characterization and Simulation Conference and Exhibition, Abu Dhabi, UAE, 9-11 October.

UNG. 2012. Unconventional Oil and Gas Report. Technical Report 49, Hart Energy LLC.

Vahrenkamp, C. V., Zhao, W., and Hurley, N. 2011. Determination and Upscaling of Rock Properties in Heterogeneous Carbonates Using Digital Rock Physics: from Nano-Meter to Grid Block Scale. Paper SPWLA present at SPWLA Conference, Abu Dhabi, March 2011.

Varfolomeev, I., Yakimchuk, I., Denisenko, A., Khasanov, I., Osinceva, N., and Rahmattulina, A. 2016. Integrated Study of Thin Sections: Optical Petrography and

Electron Microscopy. Paper SPE 182071 presented at the SPE Russian Petroleum Technology Conference and Exhibition, Moscow, Russia, 24-26 October.

Wardlaw, N.C., and McKellar, M. 1981. Mercury Porosimetry and the Interpretation of Pore Geometry in Sedimentary Rocks and Artificial Models. Powder Technology, 29: 127 -143.

Xu, S. and White, R. E. 1995. A New Velocity Model for Clay-Sand Mixtures, Geophysical Prospecting, v.43, pp. 91-118.

Zhou, W., Apkarian, R.P., Wang, Z.L., and Joy, D. 2007. Fundamental of Scanning Electron Microscopy. Scanning Microscopy of Nanotechnology.